

THESIS
2
2007

This is to certify that the
dissertation entitled

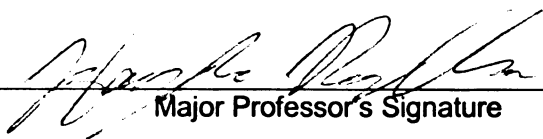
NEW TRANSFORM-BASED REPRESENTATION FOR
IMAGES

presented by

RAMIN ESLAMI

has been accepted towards fulfillment
of the requirements for the

Ph.D. degree in Electrical Engineering

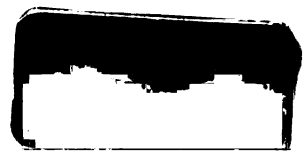

Major Professor's Signature

August 1, 2006

Date

MSU is an Affirmative Action/Equal Opportunity Institution

LIBRARY
Michigan State
University



PLACE IN RETURN BOX to remove this checkout from your record.
TO AVOID FINES return on or before date due.
MAY BE RECALLED with earlier due date if requested.

DATE DUE	DATE DUE	DATE DUE

NEW TRANSFORM-BASED REPRESENTATIONS
FOR IMAGES

By

Ramin Eslami

A DISSERTATION

Submitted to
Michigan State University
in partial fulfillment of the requirements
for the degree of

DOCTOR OF PHILOSOPHY

Department of Electrical and Computer Engineering

2006

ABSTRACT

NEW TRANSFORM-BASED REPRESENTATIONS FOR IMAGES

By

Ramin Eslami

This dissertation designs and develops new directional representation of images that are based on *true two-dimensional* (2-D) basis. Furthermore, we employ the proposed directional schemes in image denoising and coding, where the satisfactory results of these applications are heavily dependent on the nonlinear approximation behavior of the proposed schemes.

First, we develop methods to find a translation-invariant version of a general multidimensional multi-channel subsampled filter bank. In particular, we extend the *algorithme à trous* to a *generalized algorithme à trous*. Then, based on this algorithm, we propose the *translation-invariant contourlet transform* (TICT) and also the less complex and less redundant scheme of *semi-TICT* (STICT). We use the proposed TICT and STICT schemes for image denoising and compare them with the state-of-the-art methods.

Second, we propose a new family of nonredundant geometrical transforms using *Hybrid Wavelets and Directional filter banks* (HWD). We convert the wavelet basis functions in the finest scales to a flexible and rich set of directional basis elements by employing directional filter banks, where we form a nonredundant transform family, which exhibits both *directional* and *nondirectional* basis functions. We demonstrate the potential of the proposed transforms using nonlinear approximation. In addition, we employ the proposed family in two key image processing applications, image coding and

denoising, and show its efficiency for these applications.

Third, we examine the issue of linearly combining different denoising schemes in order to improve the denoising results. We propose to optimally mixing the denoising results by minimizing the ℓ_2 norm of the overall error, where we develop optimal and suboptimal approaches that do or do not require an access to the original image and the noisy image.

To My Parents and My Wife

ACKNOWLEDGMENTS

First, I must thank the almighty God, who is the origin of all creation and innovation, for enabling me to advance my work by trusting in and relying on Him. Second, I sincerely thank Professor Hayder Radha, my advisor, whose guidance, support, encouragement, patience, and considerateness taught me precious lessons in my academic life and played the key role in order that I prosper and thrive.

I am grateful to Professor John Deller, Jr. who partially advised my dissertation, and was very friendly and supportive. I would like to also thank Professors Anil Jain and Selin Aviyente as my other committee members whom I received their guidance and suggestions.

I would like to express my gratitude to Professors Hassan Khalil, Lalita Udpa, and Michael Frazier for their teaching and help during my Ph.D. program.

More importantly, I am sincerely and deeply grateful of my parents where their overall support, patience, and encouragements have been essential factors that I could pursue my degree. Finally, many thanks go to my wife and my daughter since it would have been impossible for me to accomplish many things in life without their support, companionship, and sympathy.

TABLE OF CONTENTS

LIST OF TABLES	viii
LIST OF FIGURES	ix
Chapter 1 INTRODUCTION	1
1.1 Motivation	1
1.2 Problem Statement	3
1.3 Dissertation Proposal Outline	4
Chapter 2 TRANSLATION-INVARIANT CONTOURLET TRANSFORM	6
2.1 Introduction	6
A. Background	7
B. Contributions	8
C. Overview of the Chapter	10
2.2 Contourlet Denoising using Cycle Spinning	11
A. Cycle-Spinning Algorithm	11
B. Numerical Experiment	13
2.3 Developing a TI Scheme for a Subsampled Filter Bank	15
2.4 Translation-Invariant Contourlet Transform	23
A. Translation-Invariant Pyramids	23
B. Translation-Invariant DFB	30
C. TI and Semi-TI Contourlet Transforms	33
D. Complexity Analysis and Efficient Realization	35
2.5 Image Denoising	40
A. STICT Denoising Scheme Using Bivariate Shrinkage	41
B. Simulation and Results	42
2.6 Conclusion	47
Chapter 3 A NEW FAMILY OF NONREDUNDANT DIRECTIONAL TRANSFORMS	49
3.1 Introduction	49
3.2 Background	51
A. Motivation	51
B. 2-D Separable Wavelets	53
C. Directional Filter Banks	53
3.3 Hybrid Wavelets and DFB	56
A. Construction	56
B. HWD for Quincunx Wavelets	64
C. Scaling Law and DFB Levels	65
3.4 Analysis and Realization	67
A. Multiresolution Analysis	67
B. Approximation	69

C. Efficient Realization	71
D. Complexity	74
3.5 Applications and Results	76
A. Nonlinear Approximation	76
B. Image Coding	79
C. Image Denoising	82
3.6 Conclusion	87
Chapter 4 ON THE LINEAR COMBINATION OF DENOISING SCHEMES	88
4.1 Introduction	88
4.2 Related Work	89
4.3 Optimal Linear Combination	90
A. Optimal LMS Approach	90
B. LMS Approach using the Noisy Signal	93
C. Approximation to the Optimal LMS Approach	94
4.4 Experimental Results	96
A. A Brief Note on the Denoising Artifacts	96
B. Results	99
4.5 Conclusion	103
Chapter 5 FUTURE WORK	105
5.1. Image Coding	105
5.2. Image Denoising	106
5.3. Image Watermarking	106
5.4. Other Possible Areas for HWD	106
APPENDICES	107
A.1 Proof of Remark 2.1	107
A.2 Proof of Remark 2.3	108
A.3 The Rearrangement Algorithm	111
REFERENCES	113

LIST OF TABLES

Table 1	PSNR Values of the Denoising Experiments	45
Table 2	Largest First-Order Difference of the DFB When Applied to φ	74
Table 3	PSNR Values of the NLA Experiment for the <i>Barbara</i> Image	78
Table 4	PSNR Values of the NLA Experiment for the <i>Barbara</i> Image (Quincunx Case)	79
Table 5	PSNR Values of the Denoising Experiments <i>Left Part</i> : Different Transforms with Hard Thresholding, <i>Right Part</i> : Different Denoising Methods	84
Table 6	PSNR Values of the Denoised Images	100
Table 7	PSNR Values of the Denoised Images (Advanced Methods)	101

LIST OF FIGURES

Figure 1.	A flow graph of the contourlet transform. The image is first decomposed into subbands by the Laplacian pyramid and then each detail image is analyzed by the directional filter banks.	13
Figure 2.	The contourlet transform of the <i>Boats</i> image using 3 LP levels and $\{3, 2, 2\}$ directional levels. For better visualization, the transform coefficients are clipped between 0 and 15.	14
Figure 3.	The PSNR values of the denoised images versus the standard deviation of noise for the denoising experiments.	15
Figure 4.	Denoising experiment of the <i>GoldHill</i> image corrupted with a Gaussian noise of $\sigma = 20$	16
Figure 5.	A single-level multi-channel filter bank.	17
Figure 6.	The nonsubsampling or TI multi-channel filter bank scheme in the polyphase domain.	19
Figure 7.	The effects of subsampling on the filters of a filter bank should be considered when developing a TI scheme.	20
Figure 8.	Laplacian pyramid. <i>Left</i> : The signal x is decomposed into a detail signal, d , and approximation, c . <i>Right</i> : The reconstruction scheme.	23
Figure 9.	Single-level 2-D LP in the form of an oversampled filter bank.	24
Figure 10.	The frequency responses of the analysis filters in the 2-D oversampled LP (Figure 9).	28
Figure 11.	(a) The frequency response of a DFB decomposed in 3 levels. (b) An example of the <i>vertical</i> directional filter banks using 8/2 directions. (c) An example of the <i>horizontal</i> directional filter banks using 8/2 directions.	32
Figure 12.	Some of the STICT coefficients of the <i>Boats</i> image using $L = 3$ and $\{\hat{l}_i\}_{1 \leq i \leq 3} = \{3, 2, 2\}$ directional levels. The coefficients for only one TILP subband ($k = 3$) are depicted. From <i>left to right</i> the subbands $\eta_{1,3}^{(d)}$, $\eta_{2,3}^{(d)}$, and $\eta_{3,3}^{(d)}$ with all directions are shown. For better visualization, the transform coefficients have been clipped.	34

Figure 13.	(a) Reconstructed images using the subbands $\gamma_i^{(1)}$, $\rho_{i,k}^{(1)}$, and $\eta_{i,k}^{(1)}$ for $1 \leq i \leq 3$, and $1 \leq k \leq 4$. (b) Image reconstructed using the subband(s) with indices $d = 1$, $i = 3$, and $1 \leq k \leq 4$. (c) Original image.	36
Figure 14.	The normalized joint histograms along with their contour plots of parents-children of the STICT coefficients for the images <i>Barbara</i> and <i>Peppers</i> . .	43
Figure 15.	The denoising results of the <i>Barbara</i> image when (a) $\sigma = 20$, (b) $\sigma = 40$,	46
Figure 16.	The denoising results of the <i>GoldHill</i> image when $\sigma = 10$	47
Figure 17.	The denoising results of the <i>Boats</i> image when $\sigma = 20$	48
Figure 18.	(a) 2-D separable wavelet transform. (b) The frequency partitioning of the separable wavelets. (c) Some basis functions corresponding to <i>Horizontal</i> , <i>Vertical</i> , and <i>Diagonal</i> subbands of biorthogonal 9/7 wavelets (from left to right). Note that only positive values are shown.	54
Figure 19.	(a) The frequency response of a (full-tree) DFB decomposed in 3 levels. (b) An example of the <i>vertical directional filter bank</i> (VDFB) using 3 levels. (c) An example of the <i>horizontal directional filter bank</i> (HDFB) using 3 levels.	55
Figure 20.	A schematic plot of the HWD-H transform using $l_1 = 3$ directional levels.	60
Figure 21.	The frequency partitioning in the HWD family using $l_1 = 3$ directional levels.	61
Figure 22.	A <i>directional</i> subband of HWD ($VD_1^{(3)}$). The shaded regions show the frequency support of the subband and the thick line indicate its major direction in the space domain.	62
Figure 23.	The effect of downsampling on the wavelet highpass subband which gives rise to frequency scrambling. By applying VDFB to horizontal subband in the HWD-H scheme, one can avoid inputting low-frequency regions of the wavelet subband to the directional decomposition.	63

Figure 24.	(a) Some <i>directional</i> basis functions of the HWD-H (first two rows of which the last column corresponds to the pseudo-directional subbands) and HWD-F (all except the pseudo-directional ones) when $l_1 = 3$. (Only positive values are shown.) (b) Four basis functions of the DFB with $l = 3$. (c) The corresponding magnitudes of the Fourier transform of the basis functions in (a).	64
Figure 25.	(a) The HQWD transform. (b) The frequency partitioning in the HQWD $l_1 = l_2 = 3$ directional levels. (c) <i>Left</i> : A basis function of the QWT. <i>Right</i> : Some directional basis functions of HQWD.	65
Figure 26.	<i>Top</i> : The analysis bank of the triplet QFB. <i>Bottom</i> : The synthesis bank. ..	72
Figure 27.	<i>Top</i> : The fan filter pair using triplet filter bank [1]. <i>Bottom</i> : The fan filter pair using double-halfband filter bank [72].	73
Figure 28.	<i>Left</i> : The HWD-F transform of the <i>Barbara</i> image. Here $J = 3$, $J_m = 2$, and $l_1 = l_2 = 3$. <i>Right</i> : The HWD-H transform of the <i>Boats</i> image with $J = 3$, $J_m = 2$, and $l_1 = l_2 = 2$	76
Figure 29.	Examples of the nonlinear approximation PSNR results. <i>Left</i> : The NLA results for the <i>Barbara</i> image. <i>Right</i> : The NLA results for the <i>Peppers</i> image.	77
Figure 30.	Example of the NLA visual results for the <i>Barbara</i> image when $M = 8192$	79
Figure 31.	Coding performance of the wavelet and HWD coders using SPIHT algorithm in terms of PSNR versus the rate for the <i>Barbara</i> image.	81
Figure 32.	Coding results of the <i>Barbara</i> image at rate 0.25 bpp.	82
Figure 33.	Coding results of the <i>Texture16</i> image at rate 0.1 bpp.	83
Figure 34.	Denoising results of the <i>Peppers</i> image when $\sigma = 20$	85
Figure 35.	Denoising results of the <i>Barbara</i> image when $\sigma = 40$	86
Figure 36.	(a) Some basis functions of wavelets. (b) The denoising result of the <i>Barbara</i> image using wavelets ($\sigma_v = 20$). (c) Some basis functions of contourlets. (d) The denoising result of the <i>Barbara</i> image using contourlets ($\sigma_v = 20$).	97

Figure 37.	The denoising results of the <i>Boats</i> image when $\sigma = 10$. (Note that the visual results for LMS_O and LMS_N are similar to that of LMS_A.)	102
Figure 38.	The denoising results of the <i>Barbara</i> image when $\sigma = 40$	103
Figure 39.	The polyphase domain scheme of the multi-channel filter bank given in Figure 5.	109
Figure 40.	A schematic diagram of the directional subbands using l levels ('S' is 'H' or 'V', and $d = 2^{l-1}$). <i>Left</i> : Subbands obtained by applying HDFB to a wavelet highpass channel. <i>Middle</i> : Subbands obtained by applying VDFB. <i>Right</i> : Subbands obtained by applying full-tree DFB.	111

Chapter 1

INTRODUCTION

1.1 MOTIVATION

Natural images contain smooth regions separated by regular edges, which are the common singularities found in these 2-D signals. As a result, there are two major types of correlation (or forms of *dependencies*) that exist among pixels within these images: the dependencies over the smooth regions and those dependencies that are found along edges. This implies that images can be represented more efficiently than when using the Euclidean basis, which is their current representation in the spatial domain. There have been numerous approaches that attempted to decorrelate the dependencies in images. We can divide these methods into two major categories.

Some methods work in the spatial domain, where they divide an image into homogeneous segments taking into account the edges. Binary space trees [75], quad-tree decomposition [83], and beamlets [31] are a few examples in the literature. These methods, however, are not successful in representing images with complex structure.

The other category of schemes is based on a transformation or specifically, a basis or a frame decomposition, which could be overcomplete. Fourier and wavelets are two

classical transforms in this category. A regular 1-D signal having a singularity produces many large (or *significant*) coefficients in the Fourier domain, whereas the wavelet transform of this signal results in a few significant coefficients around the singularity [91]. This makes the wavelet transform an efficient scheme for piecewise smooth 1-D signals. To measure this efficiency, we consider the nonlinear approximation behavior of the transform.

In nonlinear approximation, one retains the M largest transform coefficients (significant coefficients) and sets the others to zero. Then one measures the (ℓ_2 -norm) error of the reconstructed signal. For an orthonormal transform, this error is the same as the error in the transform domain, which is the ℓ_2 -norm of the insignificant coefficients. Hence, retaining the M largest coefficients is equivalent to the best nonlinear approximation for an orthonormal transform. It is shown that for piecewise smooth 1-D signals, wavelets provide an approximation error with a fast decay as M increases [60]. For instance, this error for a piecewise constant signal with a single discontinuity is of order 2^{-M} while it is of order $\frac{1}{M}$ when we use the Fourier transform [91].

In the 2-D case, however, although wavelets provide good nonlinear approximation results when compared to the Fourier case, they are not optimal. Two dimensional wavelets are constructed using tensor product of the 1-D transforms, which lead to separable bases. Consequently, they are not *true* bases for 2-D signals. That is, they ignore the regular geometry (e.g. regular edges) found in natural images. As a result, constructing new bases, which are more suited to natural images, has been a challenging task in recent years.

Several studies of the human visual system have shown that it is a localized, multiresolution and directional system. In addition, [68] shows that the image patches used as a basis to represent images sparsely are localized, oriented and bandpass functions. Therefore, directionality is an important feature that is not rich in wavelets. Bandelets [57], brushlets [65], complex wavelets [53], contourlet transform [28], curvelet transform [12], directionlets [90], and steerable pyramids [84] are among the directional multiresolution transforms in the literature.

There are, however, some disadvantages associated with some of these transforms. One major issue is redundancy, which is not desirable in image coding. Another issue is pseudo-Gibbs phenomena artifacts, which are introduced when setting some transform coefficients to zero prior to reconstructing the image. This happens in some image processing tasks such as image coding and denoising. It is worth noting that the problem of ringing artifacts is more serious for directional transforms when compared with their non-directional counterparts such as traditional 2-D wavelets. Another aspect of some of the recently proposed directional transforms is that they are adaptive in the sense that they do not follow a *fixed procedure* (independent of the signal) but rather signal-dependent procedures. Meanwhile, a fixed-procedure transform is usually desirable for a low computational complexity realization. Hence, one may argue that the recently developed signal-adaptive directional transforms have a key disadvantage when compared with non-directional transforms.

1.2 PROBLEM STATEMENT

In this study, we look for new 2-D transforms, which satisfy the following criteria:

- Provide perfect reconstruction

- Be multiresolution and localized transforms
- Have the feature of directionality
- Be nonredundant (required for coding applications)
- Provide good nonlinear approximation
- Introduce a minimum level of ringing artifacts during nonlinear approximation (and thus when decoding and denoising)
- Incur reasonable computational complexity

A transform fulfilling the above criteria would be a proper choice for image denoising and coding. Therefore, we look for efficient 2-D directional transforms and study their applications in image denoising and coding. Note that redundancy is not a requirement for denoising applications. Hence, this particular feature has not been pursued by some of the transforms developed under this work. Furthermore, although the complexity aspects are critical for practical realizations of any transforms, these aspects do not represent the highest priority when developing new transforms with other (arguably more critical) features such as reconstruction with minimal artifacts and high efficiency nonlinear approximation. Nevertheless, this dissertation attempts to develop low-complexity variations of high-complexity directional transforms.

1.3 DISSERTATION PROPOSAL OUTLINE

In Chapter 2 we study and propose methods to develop translation-invariant directional transforms that are primarily targeting denoising applications. To achieve this, we first develop a translation-invariant scheme corresponding to a general multidimensional multi-channel filter bank, where we extend the *algorithme à trous* to a *generalized algorithme à trous*. Then we use the proposed methods to develop

translation-invariant contourlet transform and employ it to image denoising.

We propose a new family of nonredundant directional transforms using *Hybrid Wavelets and Directional filter banks* (HWD) in Chapter 3. Then we use this family in a few image processing applications including nonlinear approximation, coding, and denoising and show its efficiency when compared with other leading transforms.

In Chapter 4 we propose and formulate methods to optimally/suboptimally and linearly combine different denoising schemes in order to improve the denoising results. Then we apply the proposed combination schemes to several image denoising approaches and provide the results.

Finally, in Chapter 5 we state possible extensions and improvements that we are currently developing and pursuing for the proposed methods.

Chapter 2

TRANSLATION-INVARIANT CONTOURLET TRANSFORM

2.1 INTRODUCTION

During the past decade, wavelets have proven their capability in many signal and image processing applications such as compression and denoising [60]. Owing to the good nonlinear approximation property of wavelets for piecewise smooth signals, they have been very effective in generating efficient representation of one-dimensional (1-D) waveforms. In the case of natural images in which piecewise regions are separated by smooth curves (or edges), however, one can still observe that there are self-similarities among the wavelet subbands. This implies that one is able to further process wavelet coefficients of an image in order to achieve more de-correlation. It is well known that wavelets are properly structured to treat point-wise singularities; hence, they are appropriate in representing piecewise smooth 1-D signals. In contrast, natural images contain 2-D singularities (edges), which need a more efficient transform than the *wavelet transform* (WT).

A. Background

An important factor of an effective transform is directionality. Having this feature, a transform would have the potential to handle 2-D singularities effectively. Many directional transforms have been introduced in recent years. Continuous (directional) wavelets [2], complex wavelets [54], steerable pyramids [85], and brushlets [65] are some examples in the literature. The wavelet X-ray transform [95] and ridgelet transform [14] apply wavelets to the radon transform of an image in such a way that one could effectively represent arbitrarily-oriented lines in an image. To make the ridgelet transform applicable to a natural image, the authors in [12] constructed curvelets using three steps: subband decompositions of the image, partitioning the subbands into blocks in such a way to satisfy the anisotropic scaling law¹, and then applying the ridgelet transform to the resulting blocks.

Using a similar idea of combining subband decomposition with a directional transform, Do and Vetterli introduced the *contourlet transform* (CT) [26]-[28]. In the CT, a *Laplacian pyramid* (LP) [10] serves as the first stage and *directional filter banks* (DFB) [5] as the second stage. The LP is a redundant transform with a redundancy ratio of up to 4/3; thus, since the DFB is critically sampled, the redundancy factor of the CT is up to 4/3. Both the LP and the DFB involve subsampling in their implementations and similar to the wavelet transform they are shift variant. Therefore, it follows that the CT is a shift-variant transform. An important advantage of translation invariance is that the performance for denoising applications is significantly improved when a *translation-*

¹ The anisotropic scaling law, which is different from the isotropic scaling law in wavelets, is based on having frame elements (generalized basis functions) with a 2-D support dimension that obeys the rule $width \propto length^2$.

invariant (TI) scheme of a subsampled transform is employed. This advantage of TI schemes is achieved due to the elimination of the pseudo-Gibbs phenomenon artifacts resulting from thresholding the transform coefficients [22]. Translation-invariant (sometimes called *stationary* or *undecimated*) wavelets have been introduced in several studies [6], [22], [62], [66], [71]. TI denoising can be realized through the cycle-spinning algorithm [22], [43]. Cycle-spinning, however, may not be a computationally efficient way to perform TI denoising for many applications. Hence, an alternative to cycle-spinning-based approaches is desired. Indeed, since wavelets are partially TI, by using an appropriate algorithm such as “*algorithme à trous*” [49], [82], the TI wavelet coefficients can be derived with low complexity, where only $N \log_2 N$ wavelet coefficients are needed to obtain the TI wavelets of a signal of size N , when using $L = \log_2 N$ levels. In contrast, in the cycle-spinning algorithm, one needs to calculate N^2 wavelet coefficients for the same signal.

In *algorithme à trous*, which is originally introduced for 1-D wavelets, we need to update the wavelet filters at each level (except the first one) when using undecimated transform (i.e., there is no subsampling operations). In a nutshell, starting from the second level, we update the decomposition filters by upsampling them with two. That is, we put zeros between samples (*trous* in French means holes). In addition to using the same procedure in the synthesis stage, we also add a scaling factor equal to $1/2$ at the end of each reconstruction level.

B. Contributions

In this chapter we propose methods for developing a TI scheme from a general multidimensional and multi-channel subsampled *filter bank* (FB). In particular, the

following contributions are presented in this chapter:

1. First, we employ the cycle-spinning algorithm (originally developed for the wavelet transform) to the contourlet transform, where it provides significant improvements over its wavelets counterpart when applied to noisy images.
2. The high complexity of the cycle spinning algorithm, however, motivates us to develop another more efficient directional TI transform. In particular, we extend the *algorithme à trous* [49] introduced for 1-D wavelets to a “*generalized algorithme à trous*” (GAT), which is applicable to a general multidimensional subsampled (uniform or non-uniform) FB.
3. We prove that the TI version of a subsampled FB obtained through the GAT provides a *tight frame*² if the original subsampled FB has a tight frame.
4. Using the proposed GAT along with employing modified versions of the DFB, we introduce the *TI contourlet transform* (TICT).
5. Although the TICT has potential to image denoising applications [36], its high redundancy in conjunction with a relatively high complexity provides an opportunity for further improvements. As a consequence, we propose *semi-TICT* (STICT), which is a less redundant and less complex scheme.
6. We also provide efficient realizations for the proposed TICT and STICT schemes. Subsequently, we propose a new image denoising scheme where we employ the STICT alongside the powerful bivariate shrinkage function (a Bayesian-based shrinkage approach, which considers the dependencies between transform coefficients) [79] and show its capability when compared with some

² In the tight frame condition, the reconstruction frame elements are the same as those for the decomposition; thus, the signal can be easily reconstructed (see Section 2.4A).

other outstanding denoising schemes.

C. *Overview of the Chapter*

The outline of the chapter is as follows: In the next section we present our first approach for translation-invariant contourlet denoising, where we employ the cycle-spinning algorithm. In Section 2.3 we study and develop a TI scheme of a subsampled FB. Then, we propose a TI scheme of the CT in Section 2.4. Section 2.5 presents a new image denoising scheme based on the STICT along with the simulation results and finally, our main conclusions and future work are given in Section 2.6.

Glossary of Abbreviations:

APS	additions per input sample
BLS-GSM	Bayes least-squares estimate using Gaussian scale mixtures
BS	bivariate shrinkage
CT	contourlet transform
CS	cycle spinning
DFB	directional filter bank
DTCWT	dual-tree complex wavelet transform
FB	filter bank
GAT	generalized <i>algorithme à trous</i>
HDFB	horizontal DFB
HT	hard thresholding
LP	Laplacian pyramid
MPS	multiplications per input sample
QFB	quincunx filter bank

STICT	semi-TI contourlet transform
TI	translation-invariant
TICT	TI contourlet transform
TIDFB	TI directional filter bank
TILP	TI Laplacian pyramid
TIWT	TI wavelet transform
VDFB	vertical DFB
WT	wavelet transform

2.2 CONTOURLET DENOISING USING CYCLE SPINNING

A. *Cycle-Spinning Algorithm*

Cycle spinning for denoising is a simple method that can be applied to a shift variant transform for signal denoising. For a shift variant transform T , operating on a noisy image $x = s + noise$, where s is the original image, we denote the 2-D circular shift by $S_{i,j}$ and the threshold operator by θ . Now, if the following procedure is applied:

$$\hat{s} = \frac{1}{K_1 K_2} \sum_{i=1, j=1}^{K_1, K_2} S_{-i, -j} (T^{-1}(\theta[T(S_{i,j}(x))])),$$

where (K_1, K_2) are the maximum number of shifts, one would expect an improvement for the estimation \hat{s} compared to the de-noised image without cycle spinning. The above cycle spinning procedure consists of the following steps:

1. Initialize $\hat{s} = 0$, $i = 0$, and $j = 0$
2. Circular-shift the noisy image by (i, j)

3. Decompose the shifted noisy image using the transform T
4. Threshold the transform coefficients
5. Obtain the denoised image by reconstructing the thresholded coefficients
6. Shift back the denoised image by $(-i, -j)$ and multiply by $1/(K_1 K_2)$
7. Add the output of Step 6 to \hat{s}
8. Increment i by 1; if $i \leq K_1$ go to Step 1
9. Increment j by 1; if $j \leq K_2$ go to Step 1
10. \hat{s} is the denoising result

For the wavelet transform decomposed into L levels ($L \leq \log_2(N)$), where the input image is of size (N, N) and $K = 2^L$, after K shifts in each direction, the transform output repeats. Since the contourlet transform is a shift variant transform, we can apply the same approach to the contourlet transform. Note that cycle-spinning algorithm is a highly complex procedure for translation-invariant denoising. As a result, we will later develop a translation-invariant contourlet transform to achieve efficient denoising.

Figure 1 shows a flow graph of the contourlet transform. It consists of two major stages: the subband decomposition and the directional transform. At the first stage, we use Laplacian pyramid (LP), and for the second one we use directional filter banks (DFB). Quincunx filter banks are the building blocks of the DFB.

We used the fan filters designed by Phoong, Kim, Vaidyanathan, and Ansari [72] with support size of $(23, 23)$ and $(45, 45)$ for the quincunx filter banks in the DFB stage.

Figure 2 depicts an example of the contourlet coefficients of the *Boats* image decomposed into three LP levels and $\{l_j\}_{1 \leq j \leq 3} = \{3, 2, 2\}$ directional levels (from finest

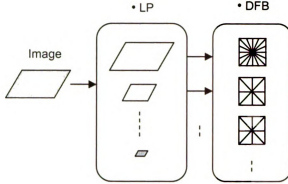


Figure 1. A flow graph of the contourlet transform. The image is first decomposed into subbands by the Laplacian pyramid and then each detail image is analyzed by the directional filter banks.

to lowest scales).

B. Numerical Experiment

To test our algorithm, we selected four images of size 512x512: *Barbara*, *GoldHill*, *Mandrill*, and *Peppers*. We used four approaches for our experiments: the contourlet transform (CT), the wavelet transform (WT), and the translation invariant wavelet transform (WT-CS) in addition to the proposed method based on the contourlet transform using cycle spinning (CT-CS). Moreover, we applied 81 cycle spins in this experiment.

We used biorthogonal Daubechies 9-7 wavelet transform and the same wavelet filters for the LP stage of the contourlet transform. For the contourlet transform, we used 6 LP levels and $\{I_j\}_{1 \leq j \leq 6} = \{5, 4, 4, 3, 3, 2\}$ directional levels. We added zero-mean Gaussian noise to the images and applied the above de-noising methods using a simple hard-thresholding to the noisy images. We set the thresholds to some values so that we obtain best PSNR values of the denoised images.

For contourlet denoising, we set the threshold values to $\{\tau_i\}_{1 \leq i \leq 6} = a \times \{3.4\sigma, 2.4\sigma, 2.4\sigma, 1.7\sigma, 1.7\sigma, 1.2\sigma\}$, where a is a constant around

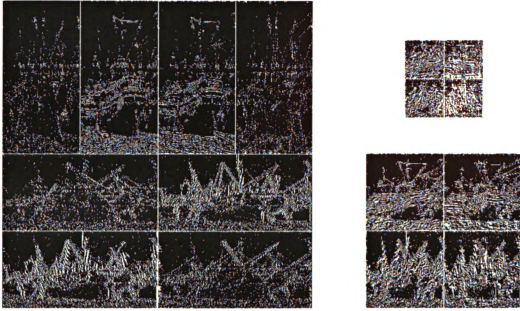


Figure 2. The contourlet transform of the *Boats* image using 3 LP levels and $\{3, 2, 2\}$ directional levels. For better visualization, the transform coefficients are clipped between 0 and 15.

one used to obtain the best value of PSNR. Note that at the finer scales we apply higher thresholds, which improves the contourlet denoising results. Note also that this method of variable thresholding fails to improve the wavelet denoising results since it introduces annoying artifacts, which resemble speckle noise.

Figure 3 shows the PSNR values of the denoised images versus a range of the input noise. For the *Peppers* image, which is a piecewise smooth image, and hence a “wavelet-friendly” image, the WT-CS performs almost the same as the CT-CS at a range of the input noise power. However, in case of images containing mostly textures and contours such as the *Barbara* image, the CT-CS yields significant improvements of up to 1.5 db over the WT-CS.

To visually compare the estimated images, we show part of the denoised images of the *GoldHill* image for $\sigma = 20$ in Figure 4.

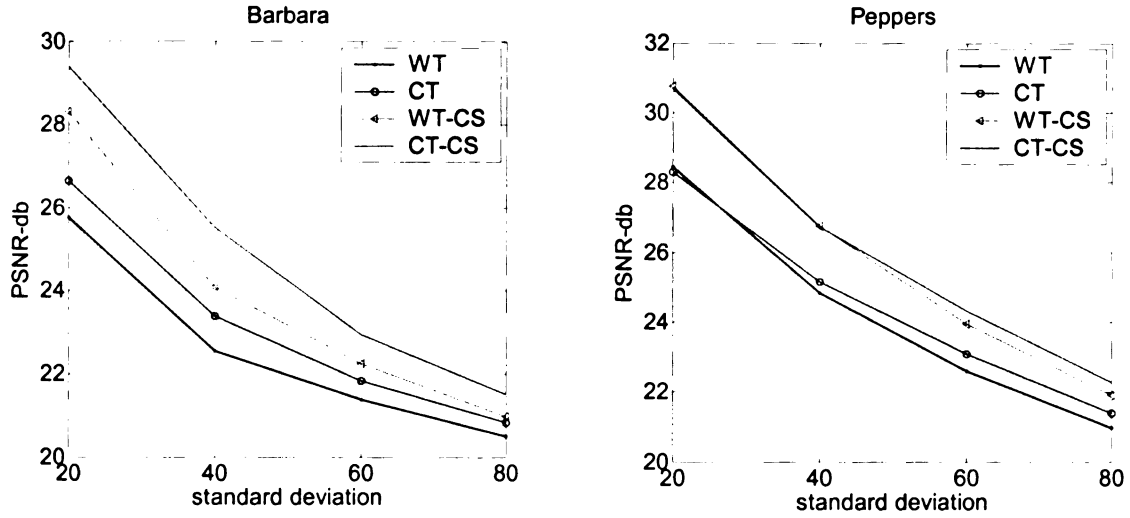


Figure 3. The PSNR values of the denoised images versus the standard deviation of noise for the denoising experiments.

2.3 DEVELOPING A TI SCHEME FOR A SUBSAMPLED FILTER BANK

In this section we develop a TI version of a general multi-channel and multidimensional FB. Translation invariance is achieved through several ways. Consider a 1-D wavelet transform scheme with periodic extension, and a signal of size N . At the first level, one decomposes the signal using the wavelet lowpass and highpass filters h and g , and then downsamples the resulting approximation and detail coefficients, that is, discards the odd-indexed coefficients.

Now, if one cyclic-shifts the original signal by an even number, e.g. $2k$, ($k \in \mathbb{Z}$), the output will be shifted by k , that is, the single-level wavelet transform is TI for even shifts. So, to make this wavelet transform TI, we also need the odd-indexed values of the filtered coefficients. To obtain these coefficients, one can cyclic-shift the signal by 1 (or an odd number) and decompose it; or, use the same signal and in downsampling shreds the even-indexed coefficients. Hence, one obtains two sets of transform coefficients for



Denoised Image Using WT-CS
PSNR = 28.87



Denoised Image Using CT-CS
PSNR = 29.39

Figure 4. Denoising experiment of the *GoldHill* image corrupted with a Gaussian noise of $\sigma = 20$.

each channel (each has a size of $N/2$) at the first level.

At the next wavelet level, we encounter the same situation. However, since we have two sets of approximation coefficients, using the same procedure as the one we used for the first level, for *each* wavelet channel we obtain four sets of coefficients, each having a length of $N/4$, leading to $2N$ coefficients at this level. We can decompose the signal up to $\log_2 N$ levels, where we get a total of $N \log_2 N$ wavelet coefficients and an approximation signal that is constant [60]. This way we achieve translation invariance by keeping all transform coefficients. For images, however, this procedure should be done in two dimensions: row and column. Consequently, omitting even- or odd-indexed rows and even- or odd-indexed columns, one can downsample the coefficients in four ways. Below we examine the problem for a general FB.

Consider a perfect reconstruction d -dimensional N -channel FB as illustrated in Figure 5. We denote M as a $d \times d$ sampling matrix. Note that if $N = d_M$, where $d_M = |\det(M)|$, the FB is critically sampled and if $N > d_M$, it is oversampled. Suppose we denote the outputs of the analysis filters before downsampling as

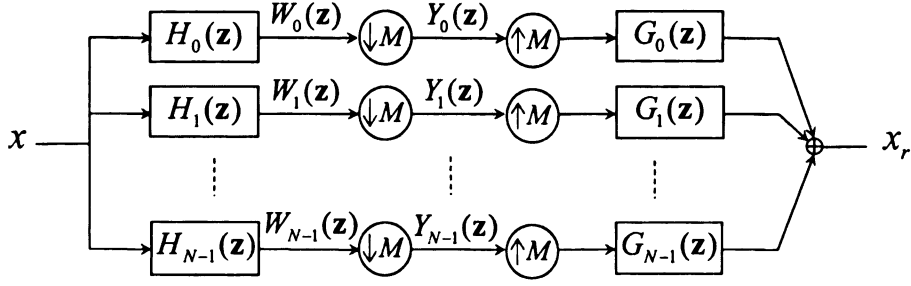


Figure 5. A single-level multi-channel filter bank.

$w_i[\mathbf{n}]$, for $0 \leq i < N$, where $\mathbf{n} = (n_1, \dots, n_d)^T \in \mathbb{Z}^d$. Hence, we have $y_i[\mathbf{n}] = w_i[M\mathbf{n}]$. Below we state a generalized procedure for obtaining all possible shifts of a multidimensional and multi-channel FB.

Remark 2.1: If one computes all possible shifts of $w_i[\mathbf{n}]$ (see Figure 5) by³ $\mathbf{k}_c \in \mathcal{N}(M)$, ($0 \leq c \leq d_M - 1$), that is, $\{w_i[\mathbf{n} + \mathbf{k}_c]\}_{0 \leq c \leq d_M - 1}$, where $d_M = |\det(M)|$, and $\mathcal{N}(M)$ is the set of integer vectors of the form $M\mathbf{t}$, $\mathbf{t} \in [0, 1)^d$, then the output of the analysis section is translation invariant. Notice that the shifting of $w_i[\mathbf{n}]$ is equivalent to shifting either the input signal $x[\mathbf{n}]$ or the analysis filter $h_i[\mathbf{n}]$ by the value of \mathbf{k}_c . It is clear that for a multilevel FB, one can apply the above method at each level for as many inputs as that level has. (See Appendix A.1 for proof.)

In the next remark, we give an example that illustrates the fact that the existence of subsampling operations in a FB is not sufficient for shift variance of the FB. In what follows we define $\mathbf{z}^{\mathbf{m}} \triangleq z_1^{m_1} \dots z_d^{m_d}$, where $\mathbf{z} = (z_1, \dots, z_d)^T$ and $\mathbf{m} = (m_1, \dots, m_d)^T \in \mathbb{Z}^d$, and define $\mathbf{z}^M \triangleq (\mathbf{z}^{\mathbf{m}_{c1}}, \dots, \mathbf{z}^{\mathbf{m}_{cd}})^T$ where M is a $d \times d$

³ Note that in general this shift could be $\mathbf{k}_c + \mathbf{m}M$ where $\mathbf{m} \in \mathbb{Z}^d$ is an arbitrary integer vector.

matrix with \mathbf{m}_{ci} as its i th column. We also adopt the notation $\mathbf{z}^{M^l} \triangleq \mathbf{z}^{(M^l)}$ for an integer $l \in \mathbb{Z}$.

Remark 2.2: Regarding Remark 2.1, if in a critically-sampled FB, without loss of generality, we have $w_i[\mathbf{n}] = w_0[\mathbf{n} + \mathbf{k}_i]$, ($0 \leq i \leq d_M - 1$) (suppose that $\mathbf{k}_0 = \mathbf{0}$), the FB will be TI. In this case the analysis and synthesis filters satisfy $H_i(\mathbf{z}) = \mathbf{z}^{\mathbf{k}_i} H_0(\mathbf{z})$ and $G_i(\mathbf{z}) = \mathbf{z}^{-\mathbf{k}_i} G_0(\mathbf{z})$, and $\{y_i[\mathbf{n}]\}_{0 \leq i \leq d_M - 1}$ represent the polyphase components of $w_0[\mathbf{n}]$. Consequently the filter bank boils down to a simple nonsubsampled system with analysis filter $H_0(\mathbf{z})$ and synthesis filter $G_0(\mathbf{z})$, where $G_0(\mathbf{z}) = 1/H_0(\mathbf{z})$ to ensure perfect reconstruction.

Using the procedure mentioned in Remark 2.1 to obtain a TI signal decomposition, is appropriate in some applications such as adaptive coding, where we need to find a “best” shift based on a cost function. In that case, we find the output of each channel for each possible shift and measure the cost to obtain a best shift for that channel. As a result, the method of finding a best tree proposed in [21] is easily extendable to the multidimensional FB case with an arbitrary sampling matrix M . If however, we need the TI representation in some other applications (such as denoising) in which we require all the TI coefficients at the same time, we can use other approaches where we do not need to shift the coefficients. In what follows, we further discuss this aspect of the TI design.

Remark 2.3: In a single-level multidimensional perfect reconstruction FB (see Figure 5), omitting the sampling operations leads to a new TI output, x_t , which is a

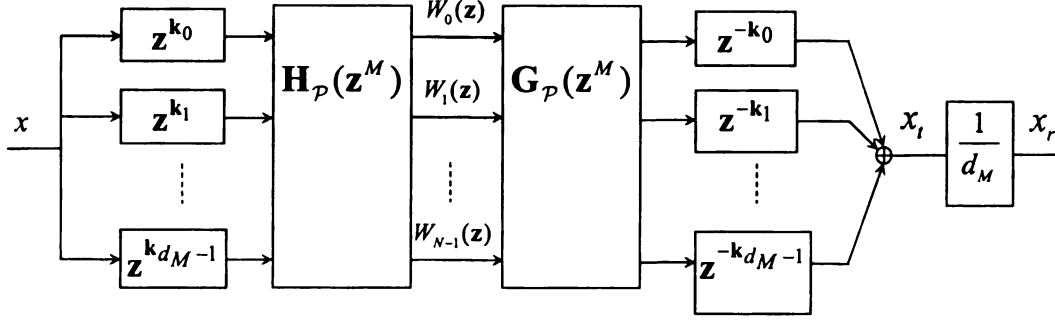


Figure 6. The nonsubsampled or TI multi-channel filter bank scheme in the polyphase domain.

scaled version of x_r , i.e. $x_t = ax_r$, where $a = 1/d_M$ (see Figure 6). Furthermore, the redundancy of the resulting TI filter bank equals N . (See Appendix A.2 for proof).

Note that each synthesis channel of the non-subsampled FB in the polyphase domain [89], [92] yields a signal equal to the reconstructed signal, and as a result, the reconstructed signal (x_r) is the average of the d_M reconstructed signals resulting from the d_M output channels of FB in the polyphase domain. However, the non-subsampled FB is redundant by a factor of N . Although redundancy is not desirable in some signal processing applications such as compression, it provides abundant information about a signal, which is advantageous for some applications such as denoising.

According to Remark 2.3, one can simply omit the subsampling operations at a single-level FB scheme to obtain a TI realization of the FB. For a multilevel FB, however, we cannot merely do so at every level to construct the corresponding TI scheme. In the nonsubsampled version of the FB, one has to change the analysis filters of level(s) $l > 1$ such that they operate the same way as if there is subsampling. In the next proposition, we show how one can construct new filters when one omits the subsampling operations in a multilevel FB, in order to achieve translation invariance.

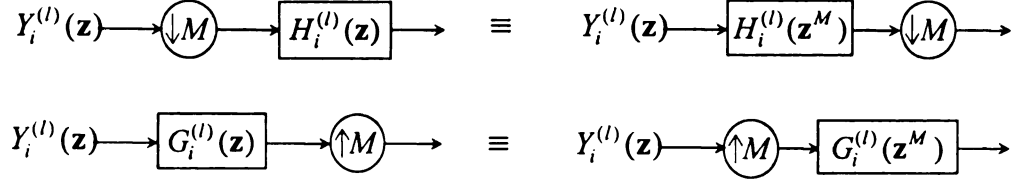


Figure 7. The effects of subsampling on the filters of a filter bank should be considered when developing a TI scheme.

Proposition 2.1 (generalized algorithme à trous): Assume that we have an L -level octave-band multi-channel FB with analysis and synthesis filters at level l as $H_i^{(l)}(\mathbf{z})$ and $G_i^{(l)}(\mathbf{z})$, ($0 \leq i < N$, $1 \leq l \leq L$), respectively and a general d -dimensional sampling matrix M (with size $d \times d$). If one omits the subsampling operations in the FB to obtain the TI scheme, the new analysis and synthesis filters at a level l , ($1 \leq l \leq L$) are $H_i^{(l)}(\mathbf{z}) = H_i(\mathbf{z}^{M^{l-1}})$ and $G_i^{(l)}(\mathbf{z}) = G_i(\mathbf{z}^{M^{l-1}})$, respectively.

Proof: We prove this proposition through induction. For the first level ($l = 1$), as stated in Remark 2.3, the filters remain unchanged. Now suppose we have the TI filters of $H_i^{(l)}(\mathbf{z}) = H_i(\mathbf{z}^{M^{l-1}})$ and $G_i^{(l)}(\mathbf{z}) = G_i(\mathbf{z}^{M^{l-1}})$ for a level l . Assume that the output of the analysis part at this level is $Y_i^{(l)}(\mathbf{z})$, ($0 \leq i < N$). Now at the next level, $l + 1$, we apply a FB using the previous level filters, which are $H_i^{(l)}(\mathbf{z})$ and $G_i^{(l)}(\mathbf{z})$. Since in the original FB, each analysis (synthesis) filter presumes a downsampled (upsampled) version of the output of the last level, as depicted in Figure 7, the equivalent filters are obtained using the noble identities: $H_i^{(l+1)}(\mathbf{z}) = H_i^{(l)}(\mathbf{z}^M)$ and $G_i^{(l+1)}(\mathbf{z}) = G_i^{(l)}(\mathbf{z}^M)$. Hence,

$$H_i^{(l+1)}(\mathbf{z}) = H_i(\mathbf{z}^{(M^{l-1})^M}) = H_i(\mathbf{z}^{M^l}), \text{ and } G_i^{(l+1)}(\mathbf{z}) = G_i(\mathbf{z}^{(M^{l-1})^M}) = G_i(\mathbf{z}^{M^l}).$$

Note that according to Remark 2.3, one has to include a scaling factor equal to $1/d_M$ after each synthesis bank. \square

The following corollary generalizes Proposition 2.1 when the sampling matrices are not the same.

Corollary 2.1: Suppose that M_l , ($1 \leq l \leq L$), is the (d -dimensional) sampling matrix for the level l in the FB mentioned in Proposition 2.1. Then the equivalent analysis and synthesis filters for the non-subsampled FB for levels $l \geq 2$ (*they remain unchanged*

for the first level) are $H_i^{(l)}(\mathbf{z}) = H_i(\mathbf{z}^{\left(\prod_{j=1}^{l-1} M_j\right)})$, and $G_i^{(l)}(\mathbf{z}) = G_i(\mathbf{z}^{\left(\prod_{j=1}^{l-1} M_j\right)})$,

respectively. To ensure perfect reconstruction, a scaling factor equal to $1/d_{M_l}$ is required after each synthesis bank having the sampling matrix M_l .

In Proposition 2.1 and Corollary 2.1 we have extended the well-known *algorithme à trous* proposed in [49] for the wavelet transform to a *generalized algorithme à trous*, which is applicable to a general multidimensional multi-channel FB system. Below we extend Remark 2.3 for a single-level non-uniform FB (i.e. has different sampling matrices). The equivalent single-level FB form of a multilevel wavelet transform is an example of such FBs.

Proposition 2.2: Suppose that a perfect reconstruction multidimensional non-uniform FB has $N = \sum_{i=1}^J n_i$ channels with analysis and synthesis filters as $\{H_{i,1}, H_{i,2}, \dots, H_{i,n_i}\}_{1 \leq i \leq J}$, and $\{G_{i,1}, G_{i,2}, \dots, G_{i,n_i}\}_{1 \leq i \leq J}$, respectively. Suppose also

that the sampling matrices for the channels $\{(i, n); 1 \leq n \leq n_i\}$ are equal, where we denote them as M_i , ($1 \leq i \leq J$). Now, if we remove the sampling operations, the FB can be made perfect reconstruction by adding a scaling factor equal to $1/d_{M_i}$, after each synthesis filter for the channels $\{(i, n); 1 \leq n \leq n_i\}$.

Proof: Here we provide a proof for a special case, where the FB with subsampling (which we call it \mathcal{A}) is a simplified version (which is obtained through FBs identities) of an L -level FB (\mathcal{B}), where \mathcal{B} is composed of a series and parallel combinations of distinct FBs like the one given in Figure 5. Note that the total number of channels in \mathcal{B} is equal to N . Now, regarding Remark 2.3, for each distinct FB in \mathcal{B} one can omit the subsampling operations, add the proper scaling factors at the end of each distinct FB, and modify the filters taking into account the relevant level and the sampling matrices before this level. Finally, one can simplify the resulting FB (\mathcal{C}) to a single-level one, where we denote it \mathcal{D} . Note that the filters in \mathcal{D} are the same as those in \mathcal{A} . Assume that a set of distinct FBs, Γ , from the input to output of \mathcal{C} with the scaling factors $\{1/d_{M_i^l}; 1 \leq l \leq L\}$, lead to the resulting channels $\{(i, n); 1 \leq n \leq n_i\}$ in \mathcal{D} , which have the same scaling factor equal to $1/d_{M_i}$. This scaling factor is in fact equal to $\prod_{l=1}^L (1/d_{M_i^l})$. On the other hand, one can conclude that the sampling matrices associated with Γ in the FB \mathcal{B} are $\{M_i^l; 1 \leq l \leq L\}$. Thus, the sampling matrix for channels $\{(i, n); 1 \leq n \leq n_i\}$ in \mathcal{A} , which is a reduced version of \mathcal{B} , is $M_i = \prod_{l=1}^L (M_i^l)$, hence, $d_{M_i} = \left| \det \left\{ \prod_{l=1}^L (M_i^l) \right\} \right| = \prod_{l=1}^L (d_{M_i^l})$. Therefore, to obtain \mathcal{D} from \mathcal{A} , one can simply omit the subsampling operations and add the scaling factor $1/d_{M_i}$ to the channels associated with the sampling matrix, M_i . \square

In the next section, we develop a TI scheme of the contourlet transform using the algorithms mentioned in this section.

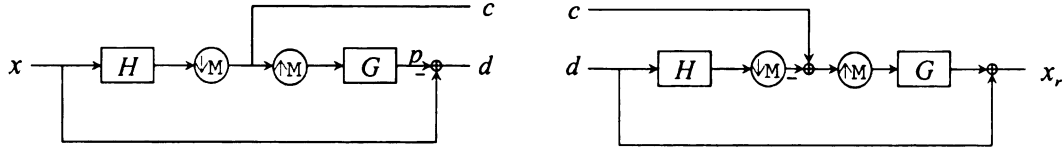


Figure 8. Laplacian pyramid. *Left*: The signal x is decomposed into a detail signal, d , and approximation, c . *Right*: The reconstruction scheme.

2.4 TRANSLATION-INVARIANT CONTOURLET TRANSFORM

The contourlet transform is composed of two stages: a *Laplacian pyramid* (LP) [10], [29] and a *directional filter bank* (DFB) [5], [70]. The LP decomposes an image into a number of radial subbands plus an approximation image. Then, the DFB is applied to each resulting detail subband where a maximum number of directions are used at the finest subband, and this number of directional levels is decreased at every other radial detail subband to achieve the anisotropic scaling law of $width \propto length^2$ [12], [27]. Since the contourlet transform is realized using two stages of subsampled FBs, to create a *TI contourlet transform* (TICT), we need to develop TI schemes for both stages, as explained below.

A. Translation-Invariant Pyramids

A new reconstruction scheme was proposed for the LP that is based on the frame reconstruction, leading to more robustness against noise [29]. Figure 8 shows the LP decomposition as well as its new reconstruction schemes. We let the sampling matrix, M , equal to $\text{diag}(2,2)$ for images, where $\text{diag}(a_1, a_2, \dots, a_N)$ is defined as a diagonal $N \times N$ matrix having (a_1, a_2, \dots, a_N) as its diagonal elements. Here H and G are 2-D

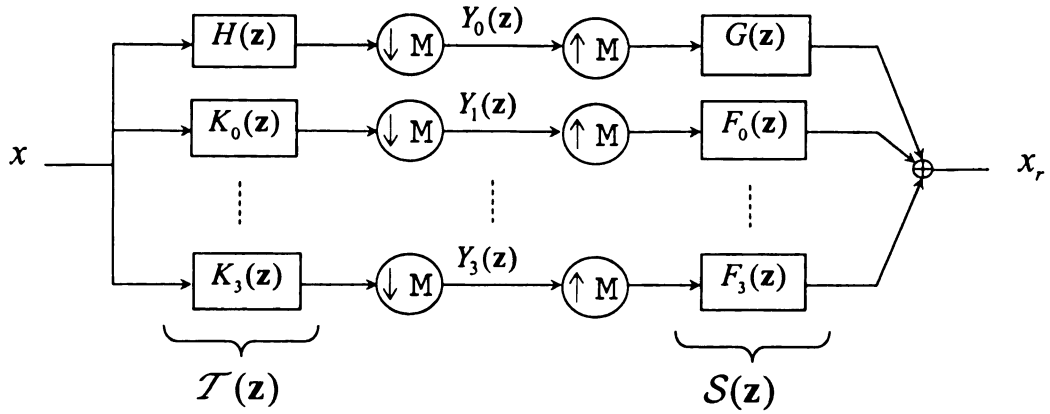


Figure 9. Single-level 2-D LP in the form of an oversampled filter bank.

lowpass filter pair⁴. Note that if one removes the subsampling operations from this LP framework, the resulting nonsubsampling FB will fail to be perfect reconstruction.

Do and Vetterli [29] proposed the LP in the polyphase domain [89], [92] in the form of an oversampled FB. In this form one can better observe the structure of the pyramids, and besides, it is a more suitable framework for developing the TI version of the LP. Defining the vector of the polyphase components of a signal x in the z -domain as $\mathbf{X}_p(\mathbf{z}) = (X_0(\mathbf{z}), \dots, X_3(\mathbf{z}))^T$, and the filters h and g as the row and column vectors $\mathbf{H}_p(\mathbf{z}) = (H_0(\mathbf{z}), \dots, H_3(\mathbf{z}))$ and $\mathbf{G}_p(\mathbf{z}) = (G_0(\mathbf{z}), \dots, G_3(\mathbf{z}))^T$, one can write the input-output relationship of the LP as (see Figure 9),

$$\mathbf{T}(\mathbf{z}) = \begin{pmatrix} H(\mathbf{z}) \\ \mathbf{z}^{\mathbf{k}_0} - G_0(\mathbf{z}^{\mathbf{M}})H(\mathbf{z}) \\ \vdots \\ \mathbf{z}^{\mathbf{k}_3} - G_3(\mathbf{z}^{\mathbf{M}})H(\mathbf{z}) \end{pmatrix} = \begin{pmatrix} H(\mathbf{z}) \\ K_0(\mathbf{z}) \\ \vdots \\ K_3(\mathbf{z}) \end{pmatrix}. \quad (2.1)$$

⁴ While it is easily extendable to the multidimensional case, we present the 2-D LP, proper for image applications.

Therefore, we have $Y(\mathbf{z}) = \mathbb{D}_M\{\mathcal{T}(\mathbf{z})X(\mathbf{z})\}$, where $\mathbb{D}_M\{\cdot\}$ denotes the downsample operator using matrix M . If the filters $h[\mathbf{n}]$ and $g[\mathbf{n}]$ are biorthogonal with respect to the sampling matrix M , the inverse transform of the LP in the polyphase domain is found to be

$$\begin{aligned}\mathcal{S}(\mathbf{z}) &= \begin{pmatrix} G(\mathbf{z}) & \mathbf{z}^{-\mathbf{k}_0} - G(\mathbf{z})H_0(\mathbf{z}^M) & \cdots & \mathbf{z}^{-\mathbf{k}_3} - G(\mathbf{z})H_3(\mathbf{z}^M) \end{pmatrix} \\ &= \begin{pmatrix} G(\mathbf{z}) & F_0(\mathbf{z}) & \cdots & F_3(\mathbf{z}) \end{pmatrix},\end{aligned}$$

and if $\mathbb{U}_M\{\cdot\}$ denotes the upsample operator with respect to the matrix M , we have (see Figure 9):

$$X_r(\mathbf{z}) = \mathcal{S}(\mathbf{z})\mathbb{U}_M\{Y(\mathbf{z})\}.$$

Figure 9 shows a single-level LP in the form of an oversampled FB. To construct a multilevel LP, one can simply iterate the single-level LP on the lowpass channel. Using the *generalized algorithm à trous* developed in Section 2.3, the multilevel TI scheme of the LP is constructed by suppressing all subsampling operations and modifying the filters at level l :

$$\mathcal{T}^{(l)}(\mathbf{z}) = \begin{pmatrix} H(\mathbf{z}^{M^{l-1}}) & K_0(\mathbf{z}^{M^{l-1}}) & \cdots & K_3(\mathbf{z}^{M^{l-1}}) \end{pmatrix}^T,$$

and

$$\mathcal{S}^{(l)}(\mathbf{z}) = \begin{pmatrix} G(\mathbf{z}^{M^{l-1}}) & F_0(\mathbf{z}^{M^{l-1}}) & \cdots & F_3(\mathbf{z}^{M^{l-1}}) \end{pmatrix},$$

where $\mathbf{z}^{M^{l-1}} = (z_1^{2^{l-1}}, z_2^{2^{l-1}})$. This implies that we upsample the corresponding filters in both row and column directions with 2^{l-1} . Note also that we should scale the signal after each synthesis bank by $1/4$. In the TILP scheme, since there are four detail channels at

each level, the redundancy factor of this scheme is $4L + 1$, when an L -level scheme is employed. Below, we provide a brief discussion about the characteristics of the LP filters (Figure 9).

As mentioned before, the LP is perfect reconstruction when the filter pair h and g are biorthogonal. Now we examine the condition in the case of the TILP.

Proposition 2.3: Upon omitting the subsampling operations in a single-level oversampled LP, the filters h and g should be biorthogonal to ensure perfect reconstruction.

Proof: The proof is straightforward noting that

$$S(\mathbf{z})T(\mathbf{z}) = 4 + G(\mathbf{z})H(\mathbf{z})\left(H_p(\mathbf{z}^M)G_p(\mathbf{z}^M) - 1\right).$$

Therefore, if $H_p(\mathbf{z}^M)G_p(\mathbf{z}^M) = 1$ we have perfect reconstruction. This condition is equivalent to $H_p(\mathbf{z})G_p(\mathbf{z}) = 1$, which implies that the filters h and g are biorthogonal.

The constant 4 indicates the need for a scaling factor. □

Consequently, removing subsampling operations from the LP does not eliminate the restriction of biorthogonality of filters h and g in the TILP frameworks. Now we take a closer look at the highpass filters of the TILP.

Proposition 2.4: Let $H^{(1d)}(z)$ be a 1-D linear phase lowpass filter having multiple zeros at $z = -1$ as:

$$H^{(1d)}(z) = (1 + z)^{N_1} (1 + z^{-1})^{N_1} R(z), \quad (2.2)$$

where $R(z) = R(z^{-1})$. Then, if $H_0^{(1d)}(z)$ and $H_1^{(1d)}(z)$ are polyphase components of $H^{(1d)}(z)$, $H_1^{(1d)}(z^2)$ has zeros at $z = \pm j$ or $\omega = \pm\pi/2$. In addition, $H_0^{(1d)}(z^2)$

and $H_1^{(1d)}(z^2)$ cannot have a zero at $z = -1$.

Proof: We can write

$$H_0^{(1d)}(z^2) = \text{Even}\{H^{(1d)}(z)\} \quad \text{and} \quad H_1^{(1d)}(z^2) = z^{-1} \text{Odd}\{H^{(1d)}(z)\}.$$

Therefore,

$$H_1^{(1d)}(z^2) \Big|_{z=\pm j} = \mp j 2^{N_1-1} (R(j) - R(-j)) = 0$$

and for the second part since $H^{(1d)}(z)$ is a lowpass filter, we have $H^{(1d)}(1) \neq 0$ and consequently, regarding (2.2) its even and odd parts are not zero at $z = -1$. \square

As a matter of fact, $H_1^{(1d)}(z^2)$ is also a lowpass filter with about half of the cutoff frequency of $H^{(1d)}(z)$. Note that the filters $G_i(\mathbf{z}^M)H(\mathbf{z})$, $(0 \leq i \leq 3)$ in (2.1) are separable and obtained from 1-D filters $G_0^{(1d)}(z)H^{(1d)}(z)$ and $G_1^{(1d)}(z)H^{(1d)}(z)$, where they have zeros at $\omega = \pi$ and the latter has also zeros at $\omega = \pm\pi/2$. It turns out that the analysis LP filters $K_i(\mathbf{z})$, $(0 \leq i \leq 3)$ - and similarly $F_i(\mathbf{z})$ - have passbands with different cutoff frequencies as illustrated in Figure 10.

Note that when we remove the subsampling operations in a FB, we encounter fewer restrictions in the filter design of such FBs. For instance, to ensure perfect reconstruction in a TI pyramid having five channels, the filters have to just fulfill the following condition:

$$H(\mathbf{z})G(\mathbf{z}) + \sum_{i=0}^3 K_i(\mathbf{z})F_i(\mathbf{z}) = 1.$$

However, there is no standard method for designing 2-D filters having more than two channels with arbitrary passband regions. Moreover, the McClellan transformation,

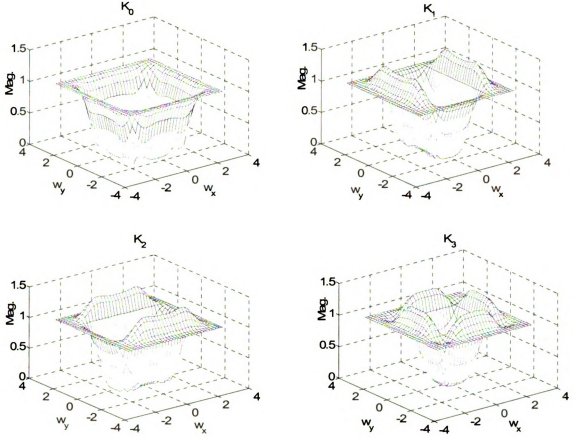


Figure 10. The frequency responses of the analysis filters in the 2-D oversampled LP (Figure 9).

which is normally used in 2-D filter design, seems to be disadvantageous in designing 2-D multi-channel FB. As a result, we resort to biorthogonal filters in the TILP similar to the LP. Next, a frame analysis is provided for a single-level TILP.

For redundant transforms, frames [25], [24] are efficient tools for analysis. A frame is defined as follows.

Definition: Let the sequence $\{\theta_j\}_{j \in \Gamma}$ and signal x , be in the Hilbert space \mathcal{H} ; then $\{\theta_j\}_{j \in \Gamma}$ is a frame if there exist two constants $A > 0$, and $B < \infty$, such that,

$A\|x\|^2 \leq \sum_{j \in \Gamma} |\langle x, \theta_j \rangle|^2 \leq B\|x\|^2$. We call A and B , the *frame bounds*. A frame is known

as a *tight frame* when $A = B$. In a tight frame, the signal is reconstructed through

$$x = A^{-1} \sum_{j \in \Gamma} \langle x, \theta_j \rangle \theta_j.$$

It is important to note that when a scheme can be expressed by a frame, it represents a stable framework, where the existence of an inverse transform is guaranteed. This is especially important for the schemes that are redundant. Since the LP is an oversampled FB, it could be better analyzed using frame theory. In the next proposition we prove that the TI realization of a single-level subsampled FB having a tight frame, is also a tight frame.

Proposition 2.5: Consider a single-level multidimensional FB (see Figure 5) having a tight frame with frame bounds equal to one. Then, the corresponding TI FB provides a tight frame with frame bounds $A = B = d_M$.

Proof: From Remark 2.1, a technique to obtain a TI set of outputs is to shift the analysis filters by \mathbf{k}_c , ($0 \leq c \leq d_M - 1$). We also shift the synthesis filters, correspondingly. Hence, for each shift we have a distinct set of kernel functions. Furthermore, each set provides a tight frame as we show it below. Assume the kernel functions of the original FB are $\{\theta_j\}_{j \in \mathbb{Z}^d}$, thus the tight frame condition implies that

$$\sum_{j \in \mathbb{Z}^d} |\langle x, \theta_j \rangle|^2 = \|x\|^2. \text{ Now a shift in } \{\theta_j\}_{j \in \mathbb{Z}^d} \text{ corresponds to the same shift in } x \text{ as}$$

mentioned in Remark 2.1. As a result, the shifted version of the kernel functions is a distinct tight frame with frame bounds equal to one. Now suppose we denote the analysis

kernel functions for a shift of \mathbf{k}_c , by $\{\theta_j^c\}_{j \in \mathbb{Z}^d}$, where $0 \leq c \leq d_M - 1$. Let us denote

$\{\varphi_j\} = \{\theta_j^c\}$, ($0 \leq c \leq d_M - 1$, and $j \in \mathbb{Z}^d$), as the kernel functions of the TI FB.

Then we have

$$\sum_{j \in \mathbb{Z}^d} |\langle x, \varphi_j \rangle|^2 = \sum_{c=0}^{d_M-1} \sum_{j \in \mathbb{Z}^d} |\langle x, \theta_j^c \rangle|^2 = d_M \|x\|^2.$$

Therefore, the TI FB provides a tight frame with frame bounds $A = B = d_M$. \square

As a result, if a subsampled FB provides a stable framework, the corresponding TI scheme also represents a stable realization.

Corollary 2.2: If the subsampled FB in Proposition 2.5 has a tight frame with frame bounds equal to K , then the corresponding TI scheme provides a tight frame with frame bounds $A = B = d_M K$.

Corollary 2.3: Since it is proven that a LP with orthogonal filters provides a tight frame [29], the single-level 2-D TILP with orthogonal filters provides a tight frame with frame bounds equal to four.

B. Translation-Invariant DFB

The DFB is the major part of the contourlet transform. It is realized through iterated quincunx FBs, and some resampling operations that just rearrange coefficients. In an \hat{l} -level DFB, we decompose the frequency space to $2^{\hat{l}}$ wedge-shaped partitions (Figure 11). Using the noble identities, one can transfer all sampling operation to the end (beginning) of the forward (inverse) transform of the DFB [70]. As a result, one obtains $2^{\hat{l}}$ analysis and $2^{\hat{l}}$ synthesis filters, $H_i^{(\hat{l})}$ and $G_i^{(\hat{l})}$, respectively and the overall

sampling matrices $S_i^{(\hat{i})}$, ($0 \leq i < 2^{\hat{i}}$), as given below [70], [27]:

$$S_i^{(\hat{i})} = \begin{cases} \text{diag}(2^{i-1}, 2), & \text{for } 0 \leq i < 2^{\hat{i}-1} \\ \text{diag}(2, 2^{i-1}), & \text{for } 2^{\hat{i}-1} \leq i < 2^{\hat{i}} \end{cases}.$$

Since it is the equivalent iterated DFB system for \hat{l} levels, to construct the TI scheme, it is sufficient to suppress the subsampling operations and multiply the reconstructed signal by a scaling factor, which is $1/\det(S_i^{(\hat{i})}) = 2^{-\hat{l}}$ for both vertical and horizontal directions. Therefore, the redundancy factor of such a scheme is equal to the number of directions $2^{\hat{l}}$.

According to the passband regions of the TILP highpass filters (see Figure 10), for filters K_1 and K_2 it is more appropriate to employ vertically- and horizontally-oriented DFBs [38], respectively (as we explain further in Section 2.4C). In vertical DFB (VDFB) and horizontal DFB (HDFB) we can achieve vertical directions (directions between 45° and 135°) and horizontal directions (directions between -45° and $+45^\circ$) as depicted in Figure 11. In these two modified DFB schemes, we stop decomposing the signal horizontally or vertically after the first level of the DFB. Therefore, the overall sampling matrices for VDFB and HDFB will be

$$S_i^{V(\hat{i})} = \begin{cases} Q, & \text{for subband } y_1 \\ \text{diag}(2, 2^{i-1}), & \text{for } 2^{\hat{i}-1} \leq i < 2^{\hat{i}} \end{cases},$$

and

$$S_i^{H(\hat{i})} = \begin{cases} \text{diag}(2^{i-1}, 2), & \text{for } 0 \leq i < 2^{\hat{i}-1} \\ Q, & \text{for subband } y_0 \end{cases},$$

where Q is the quincunx sampling matrix. Note that we can change the shape of subbands

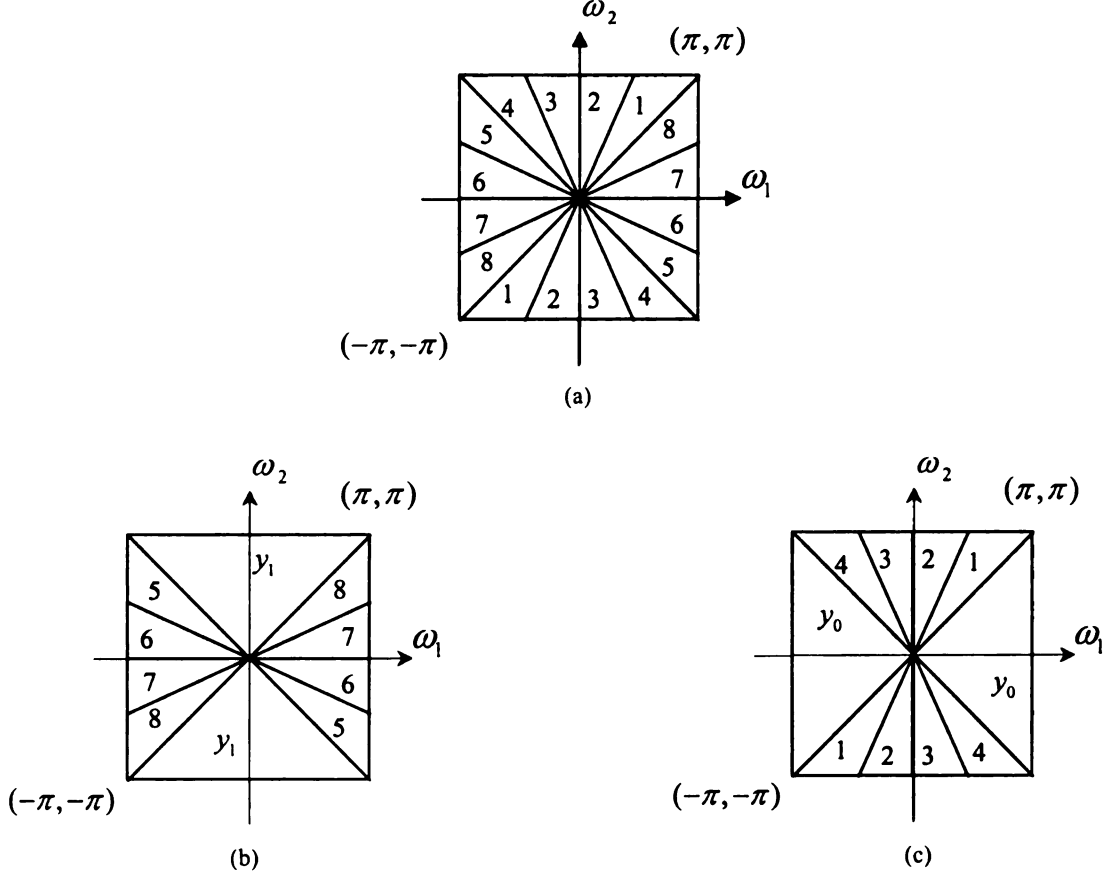


Figure 11. (a) The frequency response of a DFB decomposed in 3 levels. (b) An example of the *vertical* directional filter banks using 8/2 directions. (c) An example of the *horizontal* directional filter banks using 8/2 directions.

y_0 and y_1 (see Figure 11) in the spatial domain into a rectangle using a resampling matrix and shifting as explained in [38]. In the TI versions of the VDFB and HDFB we should consider the new sampling matrices to obtain the proper scaling factors. The redundancy factor of the modified (either vertical or horizontal) TIDFB will be $2^{\hat{i}-1} + 1$.

Note that the construction provided for the (modified) TIDFB is not efficient in terms of complexity. We will present an efficient construction in Section 2.4D.

C. *TI and Semi-TI Contourlet Transforms*

The TI contourlet transform (TICT) is constructed using the TILP and (modified) TIDFB. In fact, we employ a similar structure as the one used in the contourlet transform. However, when developing the TICT, since every level of the TILP has four highpass subbands, we propose to apply the (modified) TIDFB to each one of these subbands. The form of passbands of highpass filters in the TILP (Figure 10) suggests to apply regular TIDFB to highpass outputs of K_0 and K_3 and use TI VDFB and TI HDFB for outputs of K_1 and K_2 , respectively. To preserve the anisotropic scaling law of $width \propto length^2$, we apply (modified) TIDFBs with a desired maximum number of directional levels to the four finest subbands of the TILP, where we are at level one, then as we decrease the radial resolution of the TILP at higher levels, we decrease the directional levels at every other TILP level.

Remark 2.4: Assume that a TILP has L levels and we apply \hat{l}_i -level ($1 \leq i \leq L$) (modified) TIDFBs to the four detail subbands of level i of the TILP. Then the redundancy factor of the constructed TICT is $3L \sum_{i=1}^L 2^{\hat{l}_i} + 3$.

Improvement in denoising performance is an important reason justifying the construction of a TI version of a subband scheme. Since the redundancy of the (modified) TIDFB increases exponentially as the number of directional levels is raised, it makes the TICT highly redundant when comes along with the redundant transform of the TILP. Therefore, we propose another variety of the CT, which is less redundant and less complex. This new scheme is accomplished through applying the critically-sampled (modified) DFBs to the TILP in much the same way that we employ the (modified)

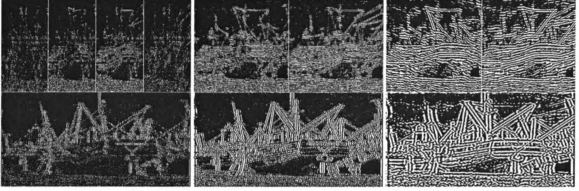


Figure 12. Some of the STICT coefficients of the *Boats* image using $L = 3$ and $\{\hat{l}_i\}_{1 \leq i \leq 3} = \{3, 2, 2\}$ directional levels. The coefficients for only one TILP subband ($k = 3$) are depicted. From left to right the subbands $\eta_{1,3}^{(d)}$, $\eta_{2,3}^{(d)}$, and $\eta_{3,3}^{(d)}$ with all directions are shown. For better visualization, the transform coefficients have been clipped.

TIDFBs to realize the TICT. Hence, this contourlet realization is not TI and therefore, we refer to this approach as the semi-TI contourlet transform (STICT). The redundancy factor of this scheme is the same as that of the TILP, which is $4L + 1$.

Figure 12 shows an example of the STICT of the *Boats* image using three TILP levels and (modified) DFBs with $\{\hat{l}_i\}_{1 \leq i \leq 3} = \{3, 2, 2\}$ directional levels. Images at the top part of each level in this figure indicate the horizontal directions. We will denote the transform coefficients of the TICT and STICT by $\rho_{i,k}^{(d)}(m)$ and $\eta_{i,k}^{(d)}(m)$, respectively, where i , ($1 \leq i \leq L$) indicates the pyramidal level, k , ($1 \leq k \leq 4$) shows the pyramidal subband at each level, d , ($1 \leq d \leq 2^{\hat{l}_i}$ -for regular DFB) specifies the directional subband at each level, and m denotes the position in two dimensions. Likewise, we can also denote the CT coefficients by $\gamma_i^{(d)}(m)$ with the same definition for i , d , and m .

Although the STICT is not TI, our preliminary image denoising results indicated the

potential of this approach [36]. The main drawback of a shift-variant FB scheme to employ for denoising is due to the appearance of artifacts when one reconstructs the signal from not all of the transform coefficients. Here, we perform a simple experiment (similar to the one in [53]) to evaluate our proposed methods. First we obtain the transform of a synthetic image of a circle using the CT, TICT, and STICT (with $\{\hat{l}_i\}_{1 \leq i \leq 3} = \{3, 2, 2\}$). Then, for each method we reconstruct the image by keeping one directional subband at a level ($L = \tilde{L}$) and its parent subbands in the other levels ($L < \tilde{L}$).

Figure 13 shows some examples of the reconstructed images. It is clear that the images reconstructed using the CT show a lot of artifacts approving the unsuitability of this scheme for some image processing tasks such as image denoising. In contrast, the results of the TICT are almost artifact-free with higher directional resolution. The STICT, interestingly, provides the results without noticeable differences to those of the TICT, which clarifies the importance of making the pyramidal subbands translation invariant. Hence, making the DFB stage translation invariant does not have much impact in improving denoising results.

In the next subsection we will provide fast realizations of the TILP and (modified) TIDFB as well as the complexity analysis of the different proposed contourlet schemes.

D. Complexity Analysis and Efficient Realization

When employing the STICT and TICT we encounter alternative FB schemes for which we propose and express efficient realizations along with their individual complexities; then we identify the complexities of the above transforms. Note that we compute the complexities for the decomposition (analysis) stages while we have similar

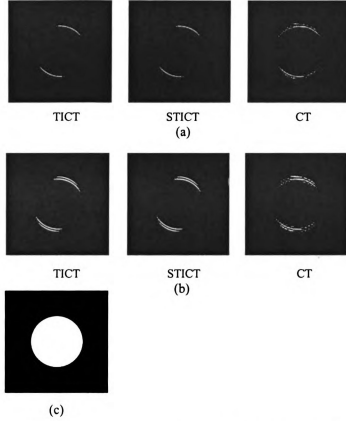


Figure 13. (a) Reconstructed images using the subbands $\gamma_i^{(1)}$, $\rho_{i,k}^{(1)}$, and $\eta_{i,k}^{(1)}$ for $1 \leq i \leq 3$, and $1 \leq k \leq 4$. (b) Image reconstructed using the subband(s) with indices $d = 1$, $i = 3$, and $1 \leq k \leq 4$. (c) Original image.

ones for the reconstruction (synthesis) bands.

1) LP:

Since the sampling matrix M is separable, the 2-D filtering could be carried out in a separable mode using the 1-D filters $h^{(1d)}$ and $g^{(1d)}$ with lengths l_h and l_g , respectively. Therefore, from Figure 8, we have $(l_h + l_g)/2$ multiplications per input sample (MPS) and $(l_h + l_g - 2)/2$ additions per input sample (APS) (note that the input to the filter G has $N^2/4$ nonzero samples for an input image of size $N \times N$). For

a multilevel LP, the complexity is up to 4/3 the complexity of a single-level LP.

2) TILP:

Considering the transfer function of a single-level TILP (2.1), although the filters K_i , ($0 \leq i \leq 3$) are indeed nonseparable, we can do the filtering in a separable mode by computing the difference of the filtered input image (by first $H(\mathbf{z})$ and then $G_i(\mathbf{z}^M)$, which are both separable filters) from the input image shifted by \mathbf{k}_i . Since $H(\mathbf{z})$ is a common filter in all the channels, we are just required to filter the input image by this filter once, which needs $2l_h$ MPS and $2l_h - 2$ APS. Now, without loss of generality, suppose that l_g is odd, then the polyphase components of $g^{(1d)}$ (denoted by $g_0^{(1d)}$ and $g_1^{(1d)}$) will have the lengths of $(l_g - 1)/2$ and $(l_g + 1)/2$. Meanwhile, the filters $G_i(\mathbf{z}^M)$, ($0 \leq i \leq 3$) are created using the 1-D filters $g_0^{(1d)}$ and $g_1^{(1d)}$. It turns out that one needs to filter the rows and columns of the input signal by $g_0^{(1d)}$ and $g_1^{(1d)}$ once. Hence, the complexity of filtering by $G_i(\mathbf{z}^M)$, ($0 \leq i \leq 3$) will be $2 \times (l_g - 1)/2 + 2 \times (l_g + 1)/2 = 2l_g$ MPS and $2l_g - 4$ APS. Consequently, the overall complexity is $2(l_g + l_h)$ MPS and $2(l_g + l_h - 1)$ APS. For an L -level TILP, the complexity will be L times the complexity of the single-level TILP.

3) DFB:

Although the quincunx sampling matrix is nonseparable and thus filtering using fan filters is nonseparable, Phoong *et al.* [72] proposed an efficient approach, which provides separable filtering in the polyphase domain. Suppose that the kernel function $\beta(z)$ in the

ladder network [72] has length l_β , which generates the 2-D synthesis filters with support sizes of $(2l_\beta - 1, 2l_\beta - 1)$ and $(4l_\beta - 3, 4l_\beta - 3)$. Then, the complexity of the *quincunx filter bank* (QFB) is $2l_\beta$ MPS and $2l_\beta - 1$ APS. Since we iterate the QFB at all channels for the higher directional levels, the complexity of the \hat{l} -level DFB will be \hat{l} times and that of a modified DFB is $(\hat{l} + 1)/2$ times the complexity of the QFB.

4) TIDFB:

In this case, opposite to the DFB, we have to perform nonseparable filtering at some levels due to omitting the subsampling operations. Nevertheless, we show that we can have a complexity similar to the separable filtering. Using again the filters designed in [72], we have the synthesis filters for QFB as follows:

$$H_0(z_1, z_2) = (1/2) \left(z_1^{-2l_\beta} + z_1^{-1} \beta(z_1 z_2^{-1}) \beta(z_1 z_2) \right),$$

and

$$H_1(z_1, z_2) = z_1^{-4l_\beta+1} - \beta(z_1 z_2^{-1}) \beta(z_1 z_2) H_0(z_1, z_2),$$

provided that the sampling matrix is

$$Q = \begin{bmatrix} 1 & 1 \\ 1 & -1 \end{bmatrix}.$$

Here, since both $\beta(z_1 z_2^{-1})$ and $\beta(z_1 z_2)$ are diagonal matrices having l_β nonzero elements, the complexity of the QFB is $4l_\beta$ MPS and $4l_\beta - 2$ APS, which is the same as the separable case. In the second level of the TIDFB, we upsample the filters by Q , where $\beta(z_1 z_2^{-1}) \beta(z_1 z_2)$ transforms to $\beta(z_2^2) \beta(z_1^2)$ and therefore, for *each* QFB we

reach the same complexity as the first level. For higher levels, in addition to the sampling matrix Q , we have resampling matrices, as well. The overall sampling matrices for these levels after the second level are in the form of [70]

$$\begin{bmatrix} 2^{\hat{l}-2} & 0 \\ 0 & 1 \end{bmatrix} \text{ or } \begin{bmatrix} 1 & 0 \\ 0 & 2^{\hat{l}-2} \end{bmatrix}.$$

Consequently, for a level $\hat{l} \geq 3$, $\beta(z_2^2)\beta(z_1^2)$ converts to $\beta(z_2^2)\beta(z_1^{2^{\hat{l}-1}})$ or $\beta(z_2^{2^{\hat{l}-1}})\beta(z_1^2)$, which indicates that for each QFB at these levels also we have the same complexity as the first level. Since the total number of the QFBs employed in an \hat{l} -level TIDFB is $2^{\hat{l}} - 1$ and that of the modified TIDFB is $2^{\hat{l}-1}$, ($\hat{l} \geq 2$), the complexity of these schemes will be $4l_\beta(2^{\hat{l}} - 1)$ MPS and $(4l_\beta - 2)(2^{\hat{l}} - 1)$ APS, and $4l_\beta 2^{\hat{l}-1}$ MPS and $(4l_\beta - 2)2^{\hat{l}-1}$ APS, respectively.

5) STICT:

In this case, for an L -level STICT employing (modified) DFBs with \hat{l}_i , ($1 \leq i \leq L$) levels, we have

$$2L(l_h + l_g) + 6l_\beta \sum_{i=1}^L \hat{l}_i + 2l_\beta L \text{ MPS,}$$

and

$$2L(l_h + l_g - 1) + 3(2l_\beta - 1) \sum_{i=1}^L \hat{l}_i + (2l_\beta - 1) \text{ APS.}$$

6) TICT:

Considering the complexity of the TILP and (modified) TIDFB,

an L -level TICT having TIDFBs with \hat{l}_i , ($1 \leq i \leq L$) levels has the complexity of

$$2L(l_h + l_g) + 12l_\beta \sum_{i=1}^L 2^{\hat{l}_i} - 8l_\beta \text{ MPS},$$

and

$$2L(l_h + l_g - 1) + (4l_\beta - 2) \sum_{i=1}^L (3(2^{\hat{l}_i}) - 2) \text{ APS}.$$

Note that in the above calculations, we have considered general forms of the filters. If, however, linear phase filters are employed, we can use about half of the filter lengths in the above complexities. We see that due to the (modified) TIDFB, both the complexity and redundancy ratio of the TICT are exponentially proportional to the directional levels \hat{l}_i , ($1 \leq i \leq L$), whereas they appear as linear terms in those of the STICT. Hence, significant reductions in complexity can be achieved when using STICT, especially when using a high number of levels.

2.5 IMAGE DENOISING

One of the major applications of the wavelet transform is denoising. For images, however, directionality is an important feature that the regular WT lacks. It follows that, when one denoises images using wavelets, the edges and fine details are smeared. Therefore, using subband decompositions having the feature of directionality as well as a good nonlinear approximation property would result in superior image denoising performance [36], [80], [86]. The CT has been shown to be a better alternative choice than the WT at some cases [28], [36], [43], [74]. In [43], a cycle-spinning algorithm is employed to improve the denoising performance of contourlets. Although it is equivalent to a TI denoising if all of the possible shifts of the input image are used [22], the

computational complexity of this procedure for an image of size $N \times N$ is N^2 times that of the CT, which consequently makes this algorithm almost prohibitive for rather large-size images. Our preliminary work on contourlet TI denoising demonstrated the effectiveness of the STICT in image denoising [36]. Here, we improve our method through finding a suitable shrinkage function.

A. *STICT Denoising Scheme Using Bivariate Shrinkage*

One of the most crucial factors in image denoising is the method of shrinkage. Because of the inter-scale and intra-scale dependencies amongst the transform coefficients, it is of key importance to build the shrinkage operation upon an appropriate probability model to account for these dependencies. Bivariate shrinkage is a recent shrinkage approach, which in addition to taking into account the dependencies among the coefficients in each subband, considers the parent-children relationship into the MAP (maximum a posteriori probability) estimation [79]. In this work, we introduce a new image denoising scheme based on the proposed STICT and incorporating bivariate shrinkage. This shrinkage approach is established through modeling the joint *probability distribution function* (PDF) of parents and children of the transform coefficients. For wavelets and also dual-tree complex wavelet coefficients, [79] proposed the following non-Gaussian joint PDF

$$p_{\mathbf{x}}(\mathbf{x}) = \frac{3}{2\pi\sigma^2} e^{-\frac{\sqrt{3}}{\sigma}\sqrt{x_1^2+x_2^2}}, \quad (2.3)$$

where x_1 and x_2 denote parents and children. The main advantage of this model is that it provides a closed-form shrinkage function that results in easy realization and also generates competitive results in comparison with the more sophisticated models [79].

For the STICT, we need to first study the joint PDF of parents-children. In this case, we propose a parent-children relationship, which is similar to the one introduced for the CT coefficients [74]. Suppose that we have the STICT with \hat{l}_i , ($1 \leq i \leq L$) directional levels, then we consider the following parent-children relationship where $\tilde{\mathbf{m}} = (m_1 / 2, m_2)^T$ for horizontal and $\tilde{\mathbf{m}} = (m_1, m_2 / 2)^T$ for vertical subbands:

$$\begin{array}{c} \text{parent} \\ \eta_{i,k}^{(d)}(\mathbf{m}) \end{array} \rightarrow \begin{array}{c} \text{child(ren)} \\ \left\{ \begin{array}{ll} \eta_{i+1,k}^{(d)}(\mathbf{m}) & \text{if } \hat{l}_{i+1} = \hat{l}_i, (i \neq L) \\ \eta_{i+1,k}^{(2d-1)}(\tilde{\mathbf{m}}) \text{ and } \eta_{i+1,k}^{(2d)}(\tilde{\mathbf{m}}) & \text{if } \hat{l}_{i+1} = \hat{l}_i + 1, (i \neq L) \end{array} \right. \end{array}.$$

For subbands corresponding to y_0 or y_1 (see Figure 11), the children lie at the same position where the parents are in the next coarser level. Note that for the approximation subband $\eta_L(\mathbf{m})$, all the directional subbands at the previous level are children subbands with a similar relationship that was mentioned above. Using this definition, in Figure 14 we demonstrate the normalized joint histogram of parents-children for the *Barbara* and *Peppers* images, when an STICT with $\{\hat{l}_i\}_{1 \leq i \leq 2} = \{3, 3\}$ directional levels is employed. We see that the joint histograms are similar to that of the wavelet coefficients (see [79]) and hence, we propose to use the model (2.3) for our bivariate shrinkage function in the STICT domain.

B. Simulation and Results

To evaluate the proposed schemes, we performed several experiments on a variety of images all of size 512×512 . Here, we also provide the CT and TICT denoising results using hard thresholding. For the sake of comparison, we also employed some of the state

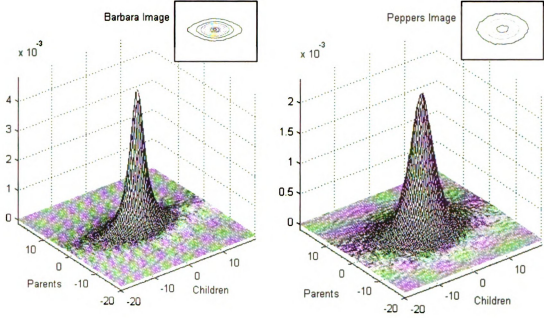


Figure 14. The normalized joint histograms along with their contour plots of parents-children of the STICT coefficients for the images *Barbara* and *Peppers*.

of the art methods in literature such as the dual-tree complex wavelet transform (DTCWT) with both hard thresholding (HT) and bivariate shrinkage (BS) [80], and the BLS-GSM denoising method propose by Portilla *et al.* [73] (using full steerable pyramid with window size (3, 3) and inclusion of parents). Furthermore, we used a *TI* (or undecimated) *wavelet transform* (TIWT) as well as adaptive wiener filter (function *wiener2* in Matlab) using a window size of (5, 5). Note that using the *generalized algorithme à trous* proposed in Section 2.3, we can easily construct the TIWT. Hence, a TIWT with L levels has the redundancy factor of $3L + 1$ and complexity of $2L(l_g + l_h)$ MPS and $2L(l_g + l_h - 2)$ APS where l_h and l_g are the lengths of the 1-D analysis filters $h^{(1d)}$ and $g^{(1d)}$.

The filters we used for the TIWT and TILP in the (S)TICT are biorthogonal

Daubechies 9/7. Further, we used 5 levels for the TIWT and a 4-level TILP in the (S)TICT. For the (modified) DFB and TIDFB, we utilized the fan filters designed in [72] with $l_\beta = 12$ and hence, support sizes of (23,23) and (45,45). We applied $\{\hat{l}_i\}_{1 \leq i \leq 4} = \{3,3,2,2\}$ directional levels to the (S)TICT except for the STICT (BS) for the *Barbara* image where we used $\{\hat{l}_i\}_{1 \leq i \leq 4} = \{4,3,3,2\}$. Note that if we use more directions and levels in the (S)TICT, there will be more artifacts introduced in the denoised images.

The images were contaminated by a zero-mean Gaussian noise with a standard deviation of σ . For all the denoising schemes, we assumed that σ is unknown and we estimated it using the robust median estimator [32]. Moreover, we mirror-extended the noisy images to avoid boundary distortion. Although the size of the noisy images is rather large, the PSNR values of the denoising results change slightly (usually up to ± 0.1 dB) when we use a different noise instance. Hence, to obtain more accurate PSNR values, we repeated each denoising experiment ten times using different noise realizations and found the average of PSNR values. We also clipped the noisy images to set the pixel values in the allowable range of 0 to 255.

Table 1 shows the PSNR values of the denoising results when the standard deviation of the input noise is varying between $\sigma = 5$ and $\sigma = 100$. In the first part of the table we used hard thresholding to compare different transforms for denoising. As seen, our proposed TICT (HT) method outperforms the other methods in most cases. In addition, the STICT (HT) provides competitive PSNR values to the other outstanding schemes.

The second part of Table 1 shows our proposed STICT (BS) denoising results as well

Table 1
PSNR Values of the Denoising Experiments

Image	σ	Noisy Image	CT (HT)	TIWT (HT)	DTCWT (HT)	STICT (HT)	TICT (HT)	TIWT (BS)	DTCWT (BS) [80]	BLS-GSM [73]	STICT (BS)
<i>Barbara</i>	5	34.15	33.64	36.54	36.04	<u>36.75</u>	37.07	37.85	37.09	37.96	<u>37.95</u>
	10	28.13	30.17	32.58	32.66	<u>33.19</u>	33.49	33.72	33.50	<u>34.40</u>	34.42
	20	22.15	26.49	28.26	28.93	<u>29.26</u>	29.53	29.41	29.78	30.60	<u>30.59</u>
	40	16.38	23.17	24.53	25.02	<u>25.42</u>	25.70	25.33	26.35	<u>26.70</u>	26.77
	70	12.25	21.04	22.19	22.28	<u>22.54</u>	22.78	22.38	23.44	<u>23.54</u>	23.57
	100	10.16	19.76	20.60	20.62	<u>20.75</u>	20.95	20.67	<u>21.41</u>	21.51	21.40
<i>Boats</i>	5	34.15	33.97	<u>36.88</u>	36.37	36.78	37.11	<u>38.13</u>	37.55	38.17	38.04
	10	28.14	30.59	<u>33.32</u>	33.24	33.31	33.59	34.19	34.02	34.69	<u>34.35</u>
	20	22.18	27.27	29.75	<u>29.80</u>	29.79	30.03	30.32	30.63	31.14	<u>30.73</u>
	40	16.42	24.08	<u>26.32</u>	26.20	26.25	26.49	26.47	<u>27.36</u>	27.65	27.15
	70	12.31	21.50	<u>23.27</u>	23.10	23.10	23.33	23.27	<u>24.33</u>	24.41	23.91
	100	10.20	19.83	<u>21.06</u>	21.00	20.89	21.08	21.12	<u>21.88</u>	21.94	21.55
<i>Lena</i>	5	34.15	35.00	37.33	<u>37.35</u>	37.30	37.52	38.27	38.00	<u>38.22</u>	38.20
	10	28.13	32.10	34.53	<u>34.71</u>	34.67	34.89	35.08	35.30	35.60	<u>35.44</u>
	20	22.13	28.91	31.35	31.45	<u>31.52</u>	31.75	31.54	<u>32.35</u>	32.63	32.30
	40	16.35	25.62	27.83	27.67	<u>27.94</u>	28.22	27.68	<u>29.24</u>	29.39	28.82
	70	12.22	22.78	<u>24.55</u>	24.31	24.52	24.82	24.23	<u>25.93</u>	25.96	25.35
	100	10.15	21.98	<u>22.20</u>	22.09	22.15	22.39	22.05	<u>23.22</u>	23.30	22.79
<i>Peppers</i>	5	34.21	33.75	<u>35.86</u>	36.04	35.68	35.83	36.88	<u>36.52</u>	36.46	36.46
	10	28.25	31.53	33.91	<u>33.99</u>	33.82	34.00	<u>34.49</u>	34.27	34.57	34.43
	20	22.32	28.50	<u>30.97</u>	30.91	30.92	31.15	31.12	31.49	31.92	<u>31.60</u>
	40	16.59	24.82	<u>27.06</u>	26.79	26.99	27.26	26.78	<u>28.00</u>	28.21	27.77
	70	12.46	21.62	<u>23.29</u>	23.00	23.20	23.45	22.90	24.29	<u>24.26</u>	23.91
	100	10.30	19.58	<u>20.70</u>	20.58	20.61	20.80	20.54	21.48	<u>21.44</u>	21.19

as those of the TIWT (BS), DTCWT (BS) [80] and BLS-GSM [73]. The computational times for these methods on the computer we ran the simulation were roughly 35s, 17s, 5s, and 95s, respectively. As seen in Table 1, for low and moderate noise ($\sigma \leq 20$) our method performs competitively to other methods but for higher power of noise this approach slightly degrades due to the amount of introduced artifacts.

Visually, however, the proposed STICT (BS) method performs better in recovering very fine details found in some images such as the *Barbara* image. Figure 15 shows the visual results of the *Barbara* image where the superior performance of the proposed approach is clear.

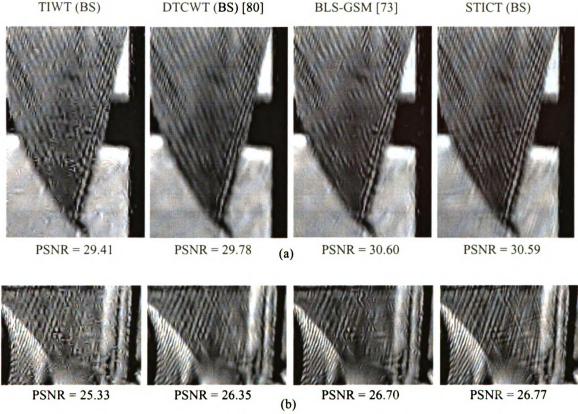


Figure 15. The denoising results of the *Barbara* image when (a) $\sigma = 20$, (b) $\sigma = 40$.

Another visual example is depicted in Figure 16, which illustrates part of the *GoldHill* image. Again, we can see that the detail over the roofs are better recovered using the STICT (BS) approach.

Finally, Figure 17 depicts another example from the *Boats* image. Here, we can compare the artifacts introduced around edges by these methods. Note that both the TIWT and dual-tree complex wavelets produce more (visible) artifacts around strong edges. The proposed method provides similar performance to that of the BLS-GSM in this figure.

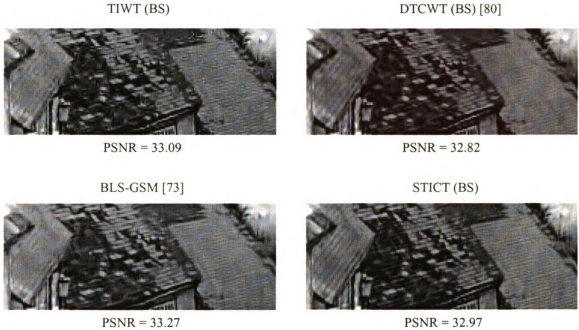


Figure 16. The denoising results of the *GoldHill* image when $\sigma = 10$.

2.6 CONCLUSION

In this work, we studied and developed new approaches for converting a general multi-channel multidimensional subsampled FB to a translation-invariant or non-subsampled FB. Particularly, we extended the *algorithme à trous*, which has been introduced for 1-D wavelets, to a *generalized algorithme à trous*, which is applicable to a general multidimensional and multi-channel FB framework.

Using the proposed *generalized algorithme à trous* as well as incorporating modified versions of the DFB, we constructed the new scheme of the *translation-invariant contourlet transform* (TICT). We also proposed *semi-TICT* (STICT) to reduce the high redundancy and complexity of the TICT. Then, we used a competent Bayesian-based shrinkage approach in conjunction with the proposed STICT to create an efficient



TIWT (BS); PSNR = 30.32



DTCWT (BS) [80]; PSNR = 30.63



BLS-GSM [73]; PSNR = 31.14



STICT (BS); PSNR = 30.73

Figure 17. The denoising results of the *Boats* image when $\sigma = 20$.

denoising scheme. Our results indicate the potential of this new scheme in image denoising.

Chapter 3

A NEW FAMILY OF NONREDUNDANT DIRECTIONAL TRANSFORMS

3.1 INTRODUCTION

Recently, there have been several studies showing that separable 2-D wavelets fail to represent images optimally [60], [91]. It is well known that the wavelet transform provides efficient approximation of 1-D piecewise smooth signals; nevertheless, since natural images possess 1-D singularities in the form of regular edges, approximation behavior of 2-D wavelets for images indicates the need for further improvement [91], [12]. As a means to offset this deficiency to some extent, most image processing systems utilizing the wavelet transform, for instance coding and denoising systems, usually take advantage of a post-processing stage to treat the inter- and intra-scale dependencies amongst the wavelet coefficients [73], [78], [79]. However, this approach alone does not necessarily eliminate the demand and need for more efficient image transforms.

To construct an efficient image transform, the following criteria are critical. First, the transform should provide a good *nonlinear approximation* (NLA) [60] behavior. This

requires the transform to be direction-sensitive (or geometric) in addition to being able to provide perfect reconstruction, multiresolution representation, and localized analysis. Other important features include the transform performance in terms of introducing a minimum level of ringing artifacts during NLA. The second criterion is that the transform should incur reasonable computational complexity. In the light of this property, fixed-procedure transforms are more desirable in contrast to the adaptive transforms, which normally impose more computations. Finally, being nonredundant is a requirement in some image processing tasks, most notably image coding.

In this chapter we introduce a new family of image transforms fulfilling the aforementioned criteria, study their properties and show their applications to coding and denoising of natural images. This family is one of the first nonadaptive directional approaches that is employed for image coding. The proposed transform family is constructed using *Hybrid Wavelets and Directional filter banks* (HWD); thus we refer to them as the HWD transforms.

Other nonredundant geometrical image transforms include bandelets [57], CRISP-contourlets [59], directionlets [90], nonredundant complex wavelets [48], and multiresolution direction filter banks [67]. A primary difference between our proposed transform family and the other nonredundant transforms mentioned above is the following. While HWD is nonadaptive, it possesses a rich set of directions, and provides an efficient NLA by taking advantage of the wavelet transform in its construction, and thus, it could be directly employed in key image processing applications such as coding. We should also note that there have been a few attempts in the past to increase the directionality of wavelets using checkerboard filter bank [4], [17]. Although these

transforms provide nonadaptive directional extension of wavelets, they are limited to a small number of directions and do not have flexibility when compared with our proposed scheme.

The chapter is organized as follows: In the next section we briefly present background material and the notations required for developing the proposed scheme. In Section 3.3 we explain the construction of the proposed HWD transform family. In Section 3.4 we provide multiresolution analysis and efficient realization of the transforms. The applications of the proposed family as well as the experimental results are given in Section 3.5 followed by our main conclusions in Section 3.6.

3.2 BACKGROUND

A. Motivation

It is known that the *wavelet transform* (WT) fails to provide optimal NLA decay for images containing regular regions of C^α ($\alpha > 1$) (i.e., α -order continuously differentiable regions) separated by *regular* discontinuities (or edges) of C^α . While the optimal decay rate of NLA is of $O(M^{-\alpha})$ where M is the number of retained coefficients during NLA, wavelets provide a decay rate of $O(M^{-1})$ [60], [57]. This low decay rate is due to the fact that the discontinuities in images yield many wavelet coefficients of large magnitude. That is, the regularity over the edges remains unseen from the WT. It turns out that there is quite ample room to further improve the NLA decay rate of wavelets.

Here, we attempt to pass wavelet coefficients through a filter bank in order to combine the large wavelet coefficients around discontinuities to achieve a more sparse

representation. Although it is possible to construct a totally different basis from wavelets, we believe that improving wavelet basis has some key advantages:

- The discrete wavelet transform can be realized using a critically-sampled filter bank and consequently, provides a nonredundant image decomposition.
- Wavelets are popular in the image processing community and there exists numerous algorithms and procedures utilizing wavelets for image processing applications; hence, one can benefit from these algorithms by cleverly adapting them to the proposed transform family.
- Wavelet packets is an alternative to handle the problem adaptively. One can also enjoy this feature of wavelets when extending it for the proposed transforms.

Other leading approaches such as curvelets [12], [13] and contourlets [28] use a similar idea of combining large transform coefficients around discontinuities. The curvelet transform has been proposed in the continuous domain and therefore, implementing it in the discrete domain is challenging. The contourlet transform employs a Laplacian pyramid [10] to extract edges of an image and applies *directional filter banks* (DFB) [5] to all bandpass outputs of the pyramid with decreasing number of directions when moving to the coarser pyramid subbands. The DFB stage attempts to decorrelate the dependencies found over the edges in the bandpass outputs of the pyramid. The reason for choosing the Laplacian pyramid as the first stage is that because its highpass channels are not subject to downsampling and thus there is no *frequency scrambling* for these channels. This construction, however, leads to the existing redundancy of the contourlet scheme, which makes this transform unsuitable for image coding.

Below we outline the notations we use in the chapter. Then we very briefly present

key aspects of the 2-D wavelet transform and DFB, which are required for the realization of the HWD family.

Notation: We denote a discrete d -dimensional signal by $x[\mathbf{n}]$ where $\mathbf{n} = (n_1, n_2, \dots, n_d)$, and its z -transform as $X(\mathbf{z}) = \sum_{\mathbf{n} \in \mathbb{Z}^d} x[\mathbf{n}] \mathbf{z}^{-\mathbf{n}}$, where $\mathbf{z} = (z_1, z_2, \dots, z_d)$ is a complex vector and $\mathbf{z}^{\mathbf{n}} = \prod_{i=1}^d z_i^{n_i}$. We also define \mathbf{z}^M as $\mathbf{z}^M = (z^{\mathbf{m}_1}, z^{\mathbf{m}_2}, \dots, z^{\mathbf{m}_d})$, where $M = [\mathbf{m}_1 \quad \mathbf{m}_2 \quad \dots \quad \mathbf{m}_d]$ is a $d \times d$ integer matrix with \mathbf{m}_i as its i th column.

B. 2-D Separable Wavelets

The 2-D separable wavelet transform [60] is obtained from the tensor product of the corresponding 1-D wavelets. Suppose that $H^{(1d)}(z)$ and $G^{(1d)}(z)$ are 1-D lowpass and highpass decomposition filters, then the lowpass and three highpass channels corresponding to the *Horizontal*, *Vertical*, and *Diagonal* subbands for 2-D wavelets are obtained as Figure 18(a) illustrates. In this work we denote the sampling matrix \mathbf{M} as $\text{diag}(2, 2) = 2I_2$. Figure 18(b) shows how the WT^5 partitions the frequency space. Since the WT uses a separable construction, the basis functions are merely aligned in two horizontal and vertical directions (see Figure 18(c)). As a result, wavelets have poor directionality.

C. Directional Filter Banks

Bamberger and Smith introduced *directional filter banks* (DFB) using quincunx and parallelogram filter banks [5], [3]. An improved version of the DFB using tree-structured

⁵ From hereafter we mention 2-D separable wavelet transform as *wavelet transform* (WT).

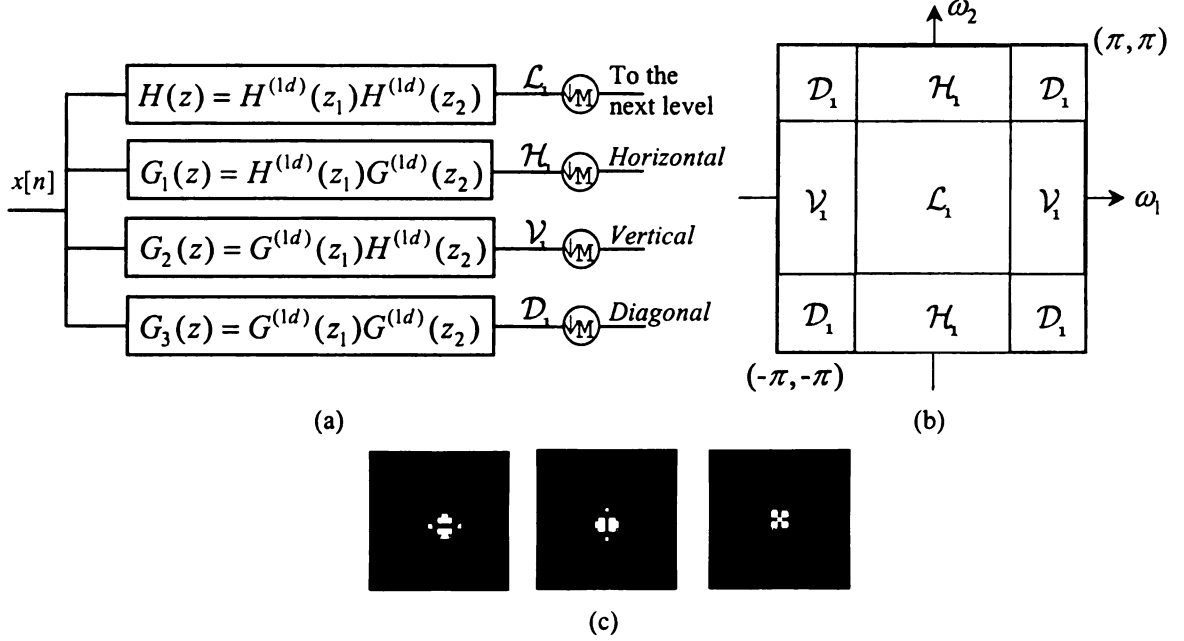


Figure 18. (a) 2-D separable wavelet transform. (b) The frequency partitioning of the separable wavelets. (c) Some basis functions corresponding to *Horizontal*, *Vertical*, and *Diagonal* subbands of biorthogonal 9/7 wavelets (from left to right). Note that only positive values are shown.

filter banks was developed recently [70]. In an l -level DFB, the frequency space is divided into 2^l wedge-shaped subbands (see Figure 19(a)). The overall sampling matrices $D_i^{(l)}$ for channels $1 \leq i \leq 2^l$ of such a DFB is [70]

$$D_i^{(l)} = \begin{cases} \text{diag}(2^{l-1}, 2), & \text{for } 1 \leq i \leq 2^{l-1} \\ \text{diag}(2, 2^{l-1}), & \text{for } 2^{l-1} < i \leq 2^l \end{cases}$$

where the channels $1 \leq i \leq 2^{l-1}$ correspond to the *mostly horizontal* subbands and the channels $2^{l-1} < i \leq 2^l$ indicate the *mostly vertical* subbands.

We can also construct *half-tree* DFBs by just decomposing the *mostly vertical* directions or the *mostly horizontal* directions, where we call the resulting schemes *vertical DFB* (VDFB) and *horizontal DFB* (HDFB) as Figure 19 depicts [38]. In VDFB

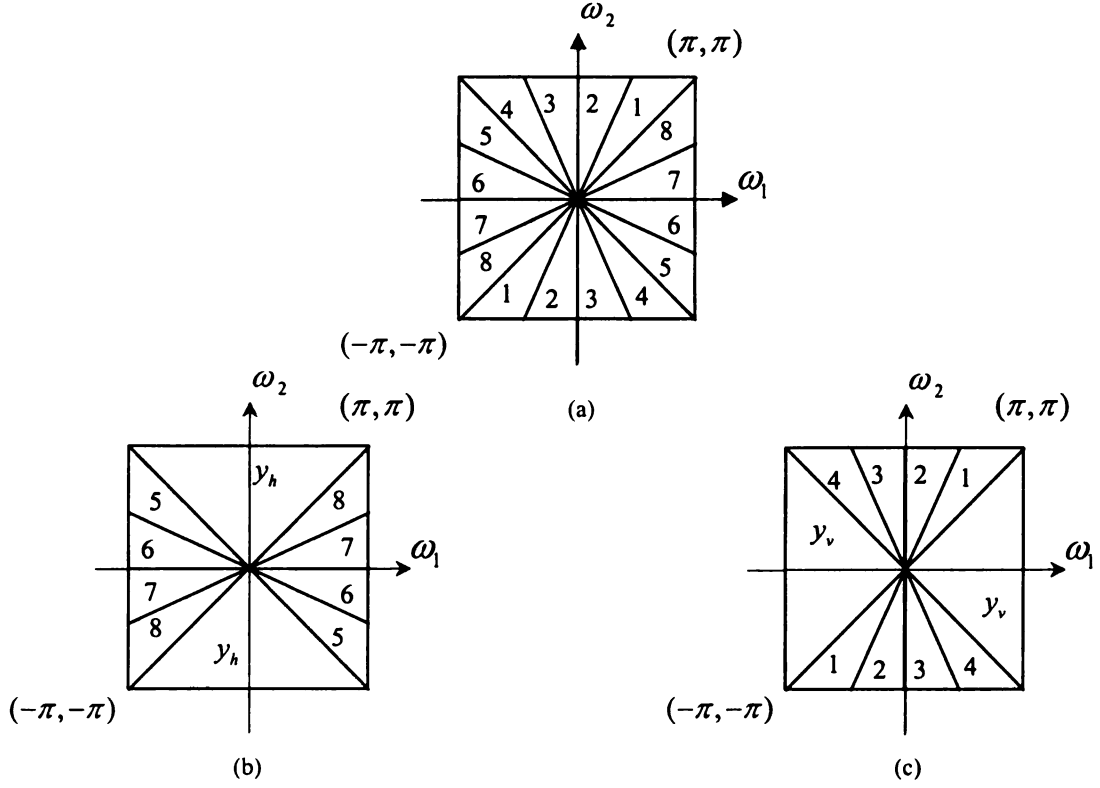


Figure 19. (a) The frequency response of a (full-tree) DFB decomposed in 3 levels. (b) An example of the *vertical directional filter bank* (VDFB) using 3 levels. (c) An example of the *horizontal directional filter bank* (HDFB) using 3 levels.

(HDFB), we stop iterating at subband y_h (y_v) after one level and do not decompose the signal horizontally (vertically) further. We call the subbands y_h and y_v as *pseudo-directional* subbands.

The first level of the DFB is a simple *quincunx filter bank* (QFB) with fan filters. Therefore, the overall sampling matrices for VDFB and HDFB are

$$D_i^{V(l)} = \begin{cases} Q, & \text{for subband } y_h \text{ (} i = 'h' \text{)} \\ \text{diag}(2, 2^{l-1}), & \text{for } 2^{l-1} < i \leq 2^l \end{cases},$$

and

$$D_i^{H(l)} = \begin{cases} \text{diag}(2^{l-1}, 2), & \text{for } 1 \leq i \leq 2^{l-1} \\ Q, & \text{for subband } y_v \text{ (} i = 'v' \text{)} \end{cases}$$

where Q is a quincunx sampling matrix. Note that we number the *directional* channels in the half-tree DFBs similar to a regular DFB. Moreover, we denote the overall reconstruction filters by $F_i^{(l)}(\mathbf{z})$, ($1 \leq i \leq 2^l$) for the DFB subband i , and also directional subbands in VDFB and HDFB with appropriate i . We also denote the synthesis fan filters resulting in subbands y_h and y_v by $F_h(\mathbf{z})$ and $F_v(\mathbf{z})$, respectively. Then, the functions $\left\{ f_i^{(l)}[\mathbf{n} - D_i^{(l)}\mathbf{m}] \right\}_{1 \leq i \leq 2^l, \mathbf{m} \in \mathbb{Z}^2}$ (and similarly $\left\{ f_i^{(l)}[\mathbf{n} - D_i^{V(l)}\mathbf{m}] \right\}_{i \in I_v^{(l)}, \mathbf{m} \in \mathbb{Z}^2}$ and $\left\{ f_i^{(l)}[\mathbf{n} - D_i^{H(l)}\mathbf{m}] \right\}_{i \in I_h^{(l)}, \mathbf{m} \in \mathbb{Z}^2}$ in VDFB and HDFB, where $I_v^{(l)} = \{i \mid i = 'v' \text{ or } 2^{l-1} < i \leq 2^l\}$ and $I_h^{(l)} = \{i \mid i = 'h' \text{ or } 1 \leq i \leq 2^{l-1}\}$) provide a directional basis for $\mathbf{l}^2(\mathbb{Z}^2)$. Note that if we utilize orthogonal fan filters in the DFBs⁶, the basis functions are orthogonal in the corresponding DFB [26].

Since we use quincunx sampling at the first level, the shape of subbands y_h and y_v in the spatial domain is diamond. We can change the shape into a rectangle using a unimodular matrix and shifting as explained in [38].

3.3 HYBRID WAVELETS AND DFB

A. Construction

We propose to extend the directionality of the WT by employing the DFBs to the

⁶ By DFBs we sometimes mean both full-tree and half-tree DFBs depending on the context.

highpass channels of the WT. Therefore, we use the name *Hybrid Wavelets and Directional filter banks* (HWD) transform family. Before describing the construction, we elaborate further regarding the proper use of the DFBs in this scheme.

A major drawback of employing DFB is the pseudo-Gibbs phenomena artifacts introduced when some of the transform coefficients are set to zero during NLA, coding [45], and denoising [44]. Since in the DFB we need to use long filters for better directional resolution and since the basis functions are directional, it turns out that the issue of ringing artifacts will be severer for the DFB when compared with other subband schemes such as WT. Do and Vetterli attempted to address this issue by applying the DFB to the Laplacian pyramid in which the highpass channels are free from frequency scrambling [28], [26].

In a previous work [45], [47], we applied DFBs to all the highpass channels of WT, which resulted in introducing many artifacts in the smooth regions during NLA and coding. In this work, we address the problem as described below.

Conjecture 3.1: The main reason for the creation of ringing artifacts when applying the DFB to the WT highpass channels is employing the DFB to the *coarser wavelet subbands*.

This conjecture is based on the following reasons:

1. The human visual system is more sensitive to the low-frequency portions of images. Consequently, the ringing artifacts resulting from the coarser wavelet scales due to applying DFBs render more irritant distortions. In addition, smooth regions have nonzero transform coefficients mainly in the coarser scales of the WT and are best represented by wavelet basis functions. Therefore, it is crucial to retain coarser

wavelet subbands and do not change their basis elements.

2. Although the frequency scrambling exists in all the levels of wavelet highpass channels, it is worse for coarser levels due to the lower frequency content of these subbands.
3. Suppose that a line segment of support size of $\ell \times 1$ exists in the input image and we apply a J -level WT (we assign level one to the finest resolution). Then the support size of the line at a level j ($1 \leq j \leq J$) is approximately $[(1 - 2^{-j})\ell_g + 2^{-j}\ell] \times (1 - 2^{-j})\ell_g$ for the diagonal subband (a similar expression is obtained for other subbands), where ℓ_g is the length of the 1-D highpass filter $g^{(1d)}[n]$. Observe that the line segment becomes thicker in coarser scales. Since we would also have larger directional basis elements if we apply DFB to the coarser scales, we expect introducing more distortion during nonlinear approximation.
4. Since large-size fan filters are employed in the DFB, the size of coarser subbands usually becomes less than the size of the DFB filters applied to them. In this case, we take advantage of the periodic extension⁷ of the signal as we see in the following example. Assume a 1-D N -point signal $x[n]$ and a filter with length ℓ ($N < \ell \leq 2N$) are given. To obtain a filtered signal with size N , we can concatenate two copies of $x[n]$ to obtain $x_C[n]$. Now we can use $2N$ -point DFT (*discrete Fourier transform*) [69] to obtain the filtered output $y_C[n]$ and find $y[n]$ as the first N -point of $y_C[n]$. One can prove that the $2N$ -point DFT of $x_C[n]$ is

⁷ Note that if we use linear-phase filters, we can benefit from symmetric extension yielding less border artifact.

expressed as

$$X_C^{(2N)}[k] = \begin{cases} 2X^{(N)}[k] & \text{for } k = 0, 2, \dots, 2N-2 \\ 0 & \text{for } k = 1, 3, \dots, 2N-1 \end{cases}$$

where $X^{(N)}[k] = \sum_{n=0}^{N-1} x[n] e^{-jn\frac{2\pi}{N}k}$ is the N -point DFT of $x[n]$. Therefore,

$X_C^{(2N)}[k]$ is proportional to the concatenation of two copies of $X^{(N)}[k]$ where the odd samples are set to zero. It turns out that a distorted version of the input signal $x[n]$ is employed in filtering, which makes the output distorted. \square

Now we explain how to construct the HWD transform family. Since in the WT we already have horizontal and vertical subbands, different paradigms could be considered to apply DFBs to the $J_m < J$ finest subbands of wavelets. We propose two types of HWD transforms:

- *HWD using Both Full-Tree and Half-Tree DFBs (HWD-H):*

- i. Apply *HDFBs* with l_j levels to *vertical* wavelet subbands at levels $1 \leq j \leq J_m$.

We denote these subbands by $VD_j^{(i)}$ ($i \in I_h^{(l_j)} = \{i \mid 1 \leq i \leq 2^{l_j-1} \text{ or } i = 'v'\}$).

- ii. Apply *VDFBs* with l_j levels to *horizontal* wavelet subbands at levels

$1 \leq j \leq J_m$. We denote these subbands by $HD_j^{(i)}$ ($i \in I_v^{(l_j)} = \{i \mid i = 'h' \text{ or }$

$2^{l_j-1} < i \leq 2^{l_j}\}$).

- iii. Apply (full-tree) *DFBs* with l_j levels to *diagonal* wavelet subbands at levels

$1 \leq j \leq J_m$. We denote these subbands by $DD_j^{(i)}$ ($i \in I_d^{(l_j)} = \{i \mid$

$1 \leq i \leq 2^{l_j}\}$).

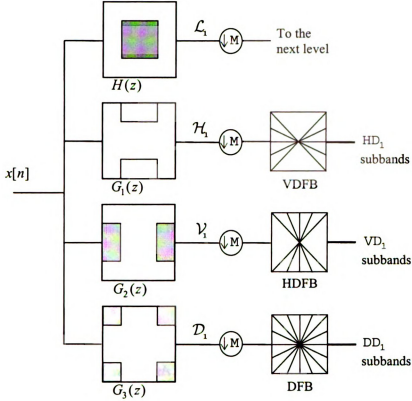


Figure 20. A schematic plot of the HWD-H transform using $l_1 = 3$ directional levels.

- *HWD using Full-Tree DFBs (HWD-F)*⁸:

Apply (full-tree) DFBs with l_j levels to all three highpass subbands of wavelets at levels $1 \leq j \leq J_m$. We denote the subbands by $VD_j^{(i)}$, $HD_j^{(i)}$, and $DD_j^{(i)}$ ($i \in I_d^{(l_j)} = \{i \mid 1 \leq i \leq 2^{l_j}\}$) corresponding to the *vertical*, *horizontal*, and *diagonal* wavelet subbands to which we applied the DFBs.

A schematic diagram of the HWD-H transform is illustrated in Figure 20. Using the noble identities [89], we can move the DFB filters before downsampling by M in the

⁸ We formerly called HWD-F and HWD-H as HWD type 3 and HWD type 2, respectively [42].

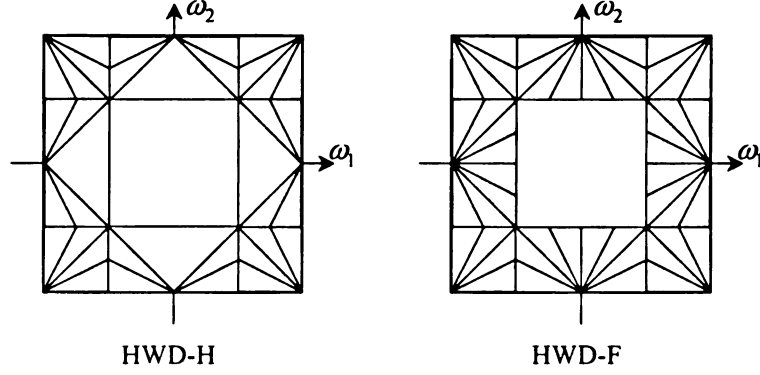


Figure 21. The frequency partitioning in the HWD family using $l_1 = 3$ directional levels.

WT. Consequently, we can find the frequency partitioning by the HWD family as Figure 21 demonstrates.

Remark 3.1 (directional subbands): In HWD-H, since we apply VDFB to wavelet horizontal subband and HDFB to wavelet vertical subband, we *convert* wavelet horizontal and vertical subbands to mostly vertical and horizontal directional subbands, respectively. However, in HWD-F, we have all set of directions at each wavelet highpass subbands in the finest scales.

Similar to the DFB, the major direction represented by each directional subband in HWD is perpendicular to the major axis passing through the subband (in the Fourier domain) as Figure 22 shows. As seen, a directional subband in the wavelet vertical subband represents a mostly horizontal direction (see also Figure 24).

Remark 3.2 (frequency scrambling): Since our objective is the construction of a critically-sampled scheme, we cannot avoid subsampling in the wavelet stage of the HWD transforms. As a result, frequency scrambling in the wavelet highpass subbands is inevitable. That is, the frequency regions of wavelet highpass subbands are subject to stretching and displacement due to downsampling by M . For instance, as Figure 23

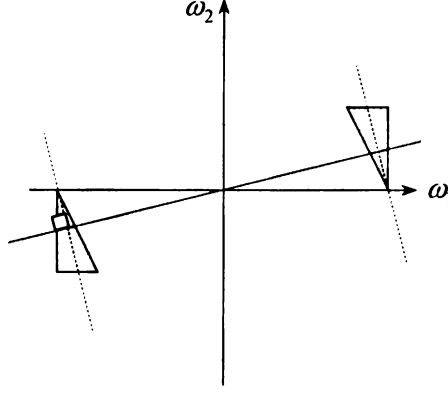


Figure 22. A *directional* subband of HWD ($VD_1^{(3)}$). The shaded regions show the frequency support of the subband and the thick line indicate its major direction in the space domain.

shows, the high frequency regions (frequencies near $\omega_2 = \pi$) of the horizontal wavelet subband are mapped to low-frequency regions (frequencies near $\omega_2 = 0$) after downsampling. Therefore, to decrease the aliasing due to downsampling, in HWD-H we decompose horizontal wavelet subbands (at finest scales) into mostly vertical directions (see Figure 23) and vertical wavelet subbands into mostly horizontal directions. Nonetheless, for some images with a large amount of textures and oscillatory patterns, taking advantage of full-tree DFBs in all wavelet finest subbands as in HWD-F, yields better results indicating the minor impact of the frequency scrambling in this case.

In Figure 24 we show some basis functions of the HWD family in both the space and Fourier domains. (Note that the Fourier transform of a basis function corresponds to its relevant subband.) As a matter of fact, in the HWD family we convert the wavelet basis functions at a few finest scales to *more directional* basis elements. We also show a few basis functions of the DFB in Figure 24(b).

Remark 3.3: Note that under HWD-F, since some of the DFB filters are oriented

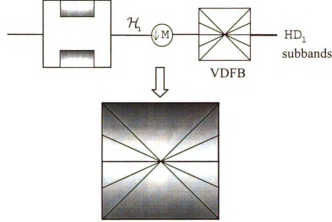


Figure 23. The effect of downsampling on the wavelet highpass subband which gives rise to frequency scrambling. By applying VDFB to horizontal subband in the HWD-H scheme, one can avoid inputting low-frequency regions of the wavelet subband to the directional decomposition.

similar to the wavelet subbands, we have more aliasing. Additionally, from Figure 24(b) last row, we can see that since the wavelet filters fail to perfectly separate frequency regions, we have more leakage to low-frequency region in those subbands.

Remark 3.4: As mentioned in Remark 3.1, the major direction represented by each directional subband in HWD is the same as the direction of the DFB subband that is employed in the HWD subband. As a result, all three directional subbands $VD_j^{(i)}$, $HD_j^{(i)}$, and $DD_j^{(i)}$ represent the same direction as subband i of the DFB stands for (see Figure 19). We can see this fact from Figure 24 when we compare parts (a) and (b).

Note that both stages utilized in the HWD family (i.e. the WT and DFB) are nonredundant and we can use any number of directions in this construction. Consequently, the HWD transforms provide a family of nonredundant, flexible and rich *directional* and *nondirectional* basis elements leading to good NLA decay for natural

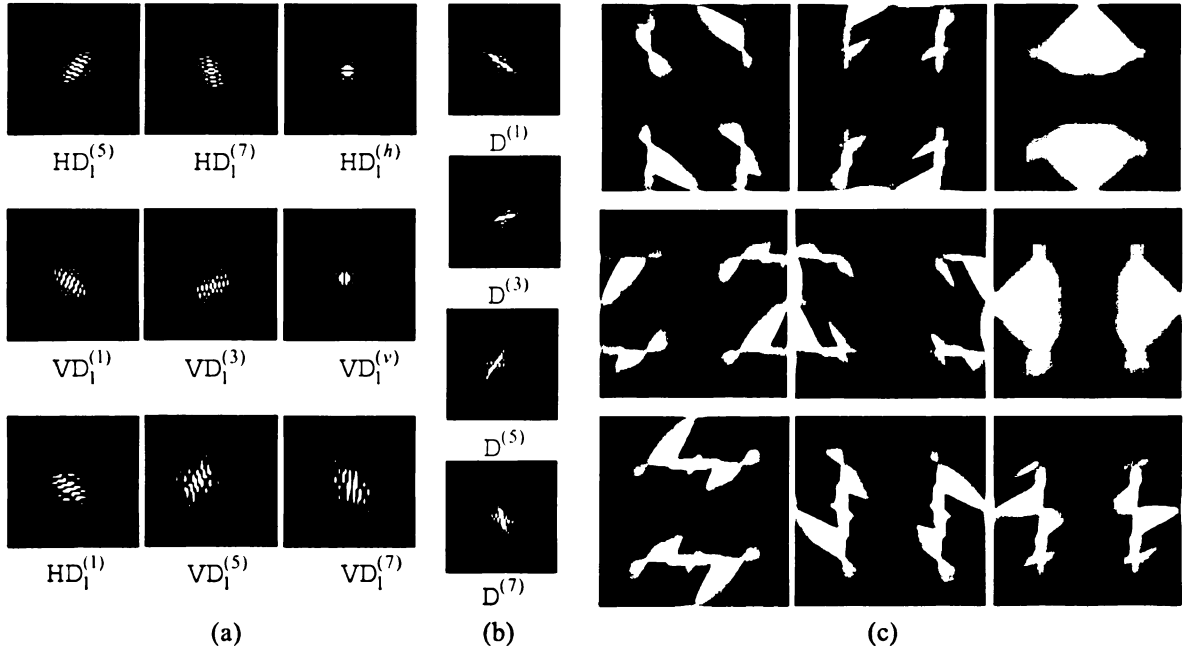


Figure 24. (a) Some *directional* basis functions of the HWD-H (first two rows of which the last column corresponds to the pseudo-directional subbands) and HWD-F (all except the pseudo-directional ones) when $l_1 = 3$. (Only positive values are shown.) (b) Four basis functions of the DFB with $l = 3$. (c) The corresponding magnitudes of the Fourier transform of the basis functions in (a).

images as we demonstrate in Section 3.5.

B. HWD for Quincunx Wavelets

Similar to the HWD, we can add directionality to the *quincunx wavelet transform* (QWT) to construct *Hybrid Quincunx Wavelets and Directional filter banks* (HQWD). In contrast to the WT, the QWT uses nonseparable diamond filters and has just one highpass channel at each level. As a result, we propose the HQWD transform as follows (see Figure 25(a)):

- HQWD:

Apply (full-tree) DFBs with l_j levels to the highpass subbands of quincunx

x

Fig

dire

as

the

In t

of 2

C.

S

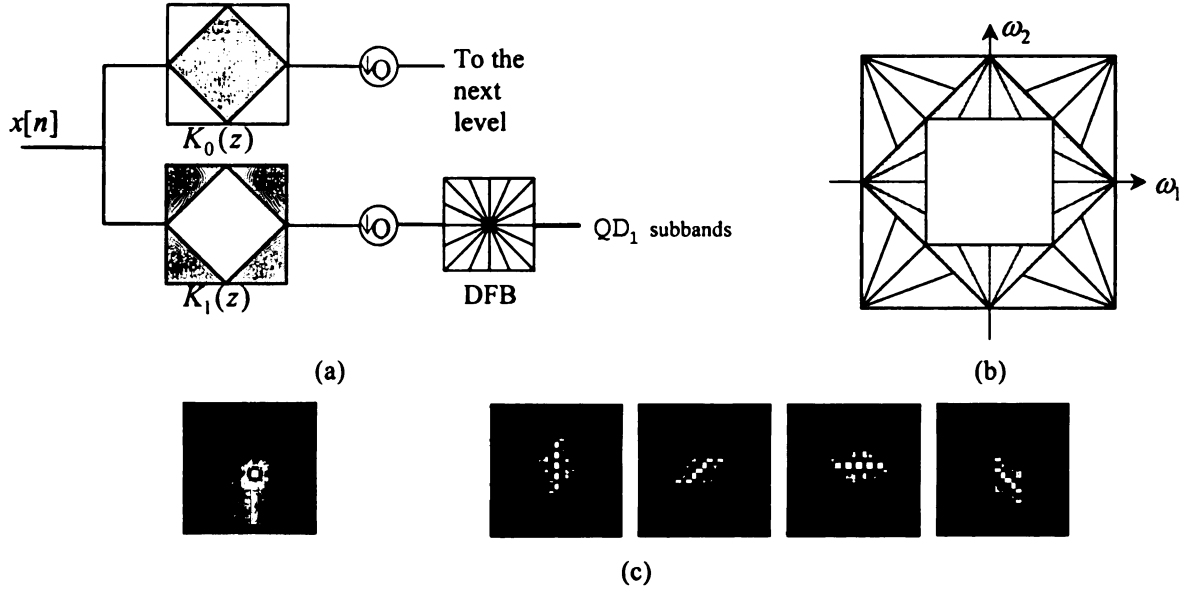


Figure 25. (a) The HQWD transform. (b) The frequency partitioning in the HQWD $l_1 = l_2 = 3$ directional levels. (c) *Left*: A basis function of the QWT. *Right*: Some directional basis functions of

wavelets at levels $1 \leq j \leq J_m$. We denote the resulting subbands by $QD_j^{(i)}$ ($1 \leq i \leq 2^{l_j}$).

Again, after using the noble identities, the frequency span of the HQWD is obtained as Figure 25(b) shows. A few basis functions are depicted in Figure 25(c). We consider the following quincunx sampling matrices for odd and even QWT levels, respectively:

$$Q_1 = \begin{bmatrix} 1 & 1 \\ -1 & 1 \end{bmatrix}, \quad \text{and} \quad Q_2 = \begin{bmatrix} 1 & -1 \\ 1 & 1 \end{bmatrix}.$$

In this case, at even levels (i.e. $j = 2k$, $k \in \mathbb{Z}$) we have the equivalent overall sampling of $M^{(j/2)}$.

C. Scaling Law and DFB Levels

Suppose that in HWD, we apply l_j -level DFBs to the highpass subbands of level j

in the

have s

maxim

the bar

Theref

$2^i \times 2^i$

$(2^i -$

directi

are con

Co

width

coarse

$1 \leq j$

N

Q^i

about

shou

T

T

in the WT. Then a transform coefficient in the directional subbands of the HWD will have support size of about $2\ell_f \times 2^{l_{j-1}}\ell_f$ after the DFB reconstruction, where the maximum size of the fan filter pair of the DFB are assumed (ℓ_f, ℓ_f) . Now, to obtain the basis element, we pass the resulting coefficients through j -level WT synthesis bank. Therefore, we have an upsampling by M^j , which expands the size of the input by $2^j \times 2^j$ followed by filtering by the overall synthesis filters of size about $(2^j - 1)\ell_g \times (2^j - 1)\ell_g$. As a result, the support size of the basis elements in the directional subbands of the HWD family is about $2^{j+1}\ell_1 \times 2^{l_j+j-1}\ell_2$, where $\ell_1 \approx \ell_2$ are constants.

Consequently, similar to contourlets, we can hold the *parabolic scaling law* of $width \propto length^2$ [12], [28] through decreasing the directional levels l_j at every other coarser wavelet scales up to level J_m : $l_{j_2} = l_{j_1} - \lfloor (j_2 - j_1)/2 \rfloor$, for levels $1 \leq j_1 < j_2 \leq J_m$.

Note that in the case of the HQWD, the QWT synthesis bank involves upsampling by Q^j that is equal to $M^{j/2}$. Hence, the support size of the basis elements in HQWD is about $2^{j/2+1}\ell_1 \times 2^{l_j+j/2-1}\ell_2$ ($\ell_1 \approx \ell_2$). It follows that for the HQWD transform we should enforce the scaling rule:

$$l_{j_2} = l_{j_1} - \lfloor (j_2 - j_1)/4 \rfloor, \quad (1 \leq j_1 < j_2 \leq J_m).$$

The number of directions in the DFB stage (l_j) and the number of finest wavelet

sc

th

at

C

m

w

H

3.

.A

ne

an

wf

V

app

spa

scales (J_m) that should be employed in the HWD are dependent on the image size and the amount of textures in the image. For texture images and images with a significant amount of texture regions we use larger values of directional levels. To satisfy item 3 in Conjecture 1 for a given image of size $N \times N$ and fan filter pair of the DFB with maximum support size of (ℓ_f, ℓ_f) , we should have

$$J_m < \log_2 \frac{N}{2\ell_f},$$

where ℓ_{J_m} is assumed 2 (the minimum number of directional levels). Note that for HQWD we have $J_m < 2\log_2(N/2\ell_f)$.

3.4 ANALYSIS AND REALIZATION

A. Multiresolution Analysis

Having the multiresolution framework for 2-D separable wavelets, we extend it to a new system to account for the proposed schemes.

Suppose that we construct 2-D wavelets from 1-D scaling and wavelet functions (φ and ψ) as [60]

$$\psi^1(\mathbf{t}) = \varphi(t_1)\psi(t_2), \quad \psi^2(\mathbf{t}) = \psi(t_1)\varphi(t_2), \quad \text{and} \quad \psi^3(\mathbf{t}) = \psi(t_1)\psi(t_2),$$

which form an orthonormal basis of $\mathbf{L}^2(\mathbb{R}^2)$. The 2-D multiresolution is defined as

$$\mathbf{V}_j^2 = \mathbf{V}_j \otimes \mathbf{V}_j, \quad (j \in \mathbb{Z}), \quad \text{where} \quad \{\mathbf{V}_j\}_{j \in \mathbb{Z}} \quad \text{denotes the corresponding 1-D}$$

approximation space and we have the detail space \mathbf{W}_j^2 connected to the approximation

space as the orthogonal component of \mathbf{V}_j^2 : $\mathbf{V}_{j-1}^2 = \mathbf{V}_j^2 \oplus \mathbf{W}_j^2$. The approximation

spaces have the inclusion property of $\mathbf{V}_{j+1}^2 \subset \mathbf{V}_j^2$, ($j \in \mathbb{Z}$). Defining the 1-D wavelet at scale 2^j as $\left\{ \psi_{j,n}(t) = 2^{-j/2} \psi(2^{-j}t - n) \right\}_{j,n \in \mathbb{Z}}$, the family $\left\{ \psi_{j,n}^k(\mathbf{t}) \right\}_{\substack{\mathbf{n} \in \mathbb{Z}^2 \\ 1 \leq k \leq 3}}$ is an

orthonormal basis of \mathbf{W}_j^2 . Note that we can also define the detail orthogonal subspaces

$$\mathbf{W}_j^{2,1} = \mathbf{V}_j \otimes \mathbf{W}_j, \quad \mathbf{W}_j^{2,2} = \mathbf{W}_j \otimes \mathbf{V}_j, \quad \text{and} \quad \mathbf{W}_j^{2,3} = \mathbf{W}_j \otimes \mathbf{W}_j,$$

Where

$$\mathbf{W}_j^2 = \bigoplus_{k=1}^3 \mathbf{W}_j^{2,k}.$$

Now for instance we consider the HWD-H transform, where we apply l_j -level ($j \leq J_m$) DFBs to the detail multiresolution space \mathbf{W}_j^2 as (see Section 3.2C):

$$\eta_{i,j,\mathbf{n}}^{1,(l_j)}(\mathbf{t}) = \sum_{\mathbf{m} \in \mathbb{Z}^2} f_i^{(l_j)}[\mathbf{m} - D_i^{V(l_j)} \mathbf{n}] \psi_{j,\mathbf{m}}^1(\mathbf{t}), \quad \text{for } i \in I_v^{(l_j)}$$

$$\eta_{i,j,\mathbf{n}}^{2,(l_j)}(\mathbf{t}) = \sum_{\mathbf{m} \in \mathbb{Z}^2} f_i^{(l_j)}[\mathbf{m} - D_i^{H(l_j)} \mathbf{n}] \psi_{j,\mathbf{m}}^2(\mathbf{t}), \quad \text{for } i \in I_h^{(l_j)}$$

and

$$\eta_{i,j,\mathbf{n}}^{3,(l_j)}(\mathbf{t}) = \sum_{\mathbf{m} \in \mathbb{Z}^2} f_i^{(l_j)}[\mathbf{m} - D_i^{(l_j)} \mathbf{n}] \psi_{j,\mathbf{m}}^3(\mathbf{t}), \quad \text{for } 1 \leq i \leq 2^{l_j} \text{ (or } i \in I_d^{(l_j)}).$$

Therefore, by using orthogonal DFBs, we span the detail subspaces $\mathbf{W}_j^{2,1}$, $\mathbf{W}_j^{2,2}$, and

$\mathbf{W}_j^{2,3}$ ($j \leq J_m$) into the following orthogonal directional subspaces:

$$\mathbf{W}_j^{2,1} = \bigoplus_{i \in I_v} \mathbf{W}_j^{2,1,(i)}, \quad \mathbf{W}_j^{2,2} = \bigoplus_{i \in I_h} \mathbf{W}_j^{2,2,(i)}, \quad \text{and} \quad \mathbf{W}_j^{2,3} = \bigoplus_{i \in I_d} \mathbf{W}_j^{2,3,(i)}.$$

For the other levels $J_m < j \leq J$ in HWD-H, we have the same functions as wavelets:

$$\left\{ \psi_{j,n}^k(\mathbf{t}) \right\}_{\substack{\mathbf{n} \in \mathbb{Z}^2 \\ 1 \leq k \leq 3}}.$$

Remark 3.5: The family

$$\left\{ \eta_{i_1,j,\mathbf{n}}^{1,(l_j)}, \eta_{i_2,j,\mathbf{n}}^{2,(l_j)}, \eta_{i_3,j,\mathbf{n}}^{3,(l_j)} \right\}_{\substack{i_1 \in I_v, i_2 \in I_h, i_3 \in I_d \\ \mathbf{n} \in \mathbb{Z}^2}}$$

provides an orthonormal basis for \mathbf{W}_j^2 ($j \leq J_m$). In addition, each individual family

$$\left\{ \eta_{i_1,j,\mathbf{n}}^{1,(l_j)} \right\}_{\substack{i_1 \in I_v \\ \mathbf{n} \in \mathbb{Z}^2}}, \left\{ \eta_{i_2,j,\mathbf{n}}^{2,(l_j)} \right\}_{\substack{i_2 \in I_h \\ \mathbf{n} \in \mathbb{Z}^2}}, \text{ and } \left\{ \eta_{i_3,j,\mathbf{n}}^{3,(l_j)} \right\}_{\substack{i_3 \in I_d \\ \mathbf{n} \in \mathbb{Z}^2}},$$

provides an orthonormal basis for the detail subspaces $\mathbf{W}_j^{2,1}$, $\mathbf{W}_j^{2,2}$, and $\mathbf{W}_j^{2,3}$ ($1 \leq j \leq J_m$), respectively.

Proof of the above statement is similar to that of the quad-tree decomposition in wavelet packets [60]. Since we use orthonormal filters in the DFBs, we divide $\mathbf{W}_j^{2,k}$, ($1 \leq k \leq 3$) into orthogonal detail subspaces after each directional level. As a result, the proof is achieved through induction.

Remark 3.6: The family $\left\{ \eta_{i_1,j,\mathbf{n}}^{1,(l_j)}(\mathbf{t}), \eta_{i_2,j,\mathbf{n}}^{2,(l_j)}(\mathbf{t}), \eta_{i_3,j,\mathbf{n}}^{3,(l_j)}(\mathbf{t}) \right\}_{\substack{i_1 \in I_v, i_2 \in I_h, i_3 \in I_d \\ \mathbf{n} \in \mathbb{Z}^2, j \leq J_m}}$

together with $\left\{ \psi_{j,\mathbf{n}}^k(\mathbf{t}), \varphi_{J,\mathbf{n}}(\mathbf{t}) \right\}_{\substack{\mathbf{n} \in \mathbb{Z}^2, J > j > J_m \\ 1 \leq k \leq 3}}$ provide an orthonormal basis for

$\mathbf{L}^2(\mathbb{R}^2)$.

We can derive similar analyses for HWD-F and also HQWD.

B. Approximation

Owing to the similar structure of the proposed HWD-F to contourlets [28], one can prove a similar NLA rate of decay for HWD-F for a class of signals. In particular, it can be shown that an image x containing \mathbf{C}^2 regions separated by \mathbf{C}^2 curves when

decomposed by an HWD-F transform, follows the NLA decay of

$$\|x - x_M\|_2^2 \leq A(\log M)^3 M^{-2},$$

where x_M is the reconstructed image using M largest-magnitude transform coefficients and A is a positive constant. Note that the directional subbands in the HWD-F transform should have as many directional vanishing moments as possible (ideally have perfect *flat* passbands and are zero elsewhere) and the wavelet scaling function should satisfy $\varphi \in C^2$.

The proof is similar to the one provided for the contourlet transform's approximation decay [28], however, we must emphasize a few points.

1. Generally, the curves in the image will have components in all three wavelet highpass subbands where they are subject to being directionally decomposed by the DFBs. Thus, each segment of curve will have just significant components when it intersects a directional basis function oriented alongside the curve. The fact that we have three highpass channels in the WT stage of HWD as opposed to the one highpass subband of the pyramid stage of contourlets, only changes the constant A in the NLA decay rate.

2. The scales $j > J_m$ (wavelet subbands) in HWD-F mostly stand for the smooth regions and the wavelet highpass subbands furnish sufficient angular resolution for the curve components.

3. Unlike the contourlet transform, since HWD take advantage of wavelets with horizontal and vertical vanishing moments and good NLA decay when compared with the Laplacian pyramid in contourlets, practically HWD shows better NLA decay in

comparison to the contourlet transform (*see* Section 3.5A).

In the next section, we provide an efficient realization for the proposed transform family.

C. *Efficient Realization*

While the WT can be implemented efficiently using 1-D filters, the DFBs in the HWD need to be treated carefully. Although the quincunx filter bank [89], which is the major building block of a DFB, is a non-separable filter bank system, it is possible to implement it using ladder network and hence benefiting from low computational cost similar to 2-D separable filtering.

Phoong *et al.* [72] proposed a two-channel filter bank using a pair of halfband filters, which can be realized in the polyphase domain using ladder network. This scheme, however, has some restrictions. Ansari *et al.* [1] proposed a two-channel filter bank using a triplet of halfband filters, where they could address the restrictions in double-halfband filter bank. We use this scheme to construct the DFBs.

The equivalent analysis band of the *quincunx filter bank* (QFB) scheme using diamond filter is shown in Figure 26. The parameter c is set to $\sqrt{2} - 1$, to ensure that the 1-D lowpass and highpass filters have the same magnitude of $1/\sqrt{2}$ at $\omega = \pi/2$; a condition not achieved using the double-halfband filter bank. To have the maximum regularity of the filters, we use the Lagrange coefficients (a_k) in the FIR 1-D T -filter [1]

$$R^{(1d)}(z) = \sum_{k=1}^{N_T} a_k (z^{-k} + z^{k-1}), \text{ where}$$

$$a_k = \frac{(-1)^{k+N_T-1} \prod_{i=1}^{2N_T} (N_T + 0.5 - i)}{(N_T - k)!(N_T - 1 + k)!(k - 0.5)}.$$

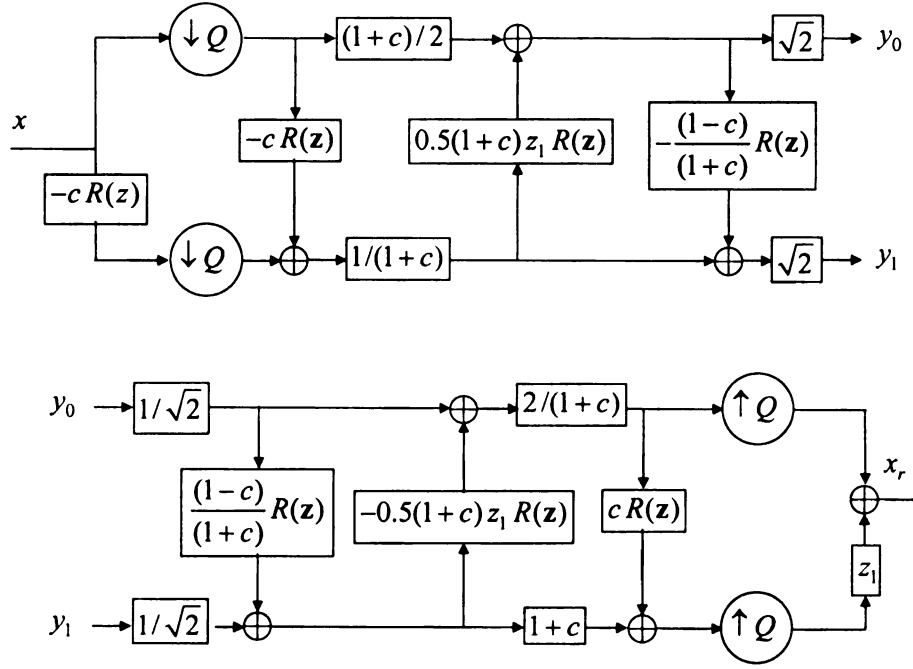


Figure 26. *Top*: The analysis bank of the triplet QFB. *Bottom*: The synthesis bank.

To have a QFB with diamond filter pair, we use the transformation $R(\mathbf{z}) = R^{(1d)}(z_1)R^{(1d)}(z_2)$, whereas we use time-reversed versions of the T -filters to obtain a QFB with fan filters: $R(\mathbf{z}) = R^{(1d)}(-z_1)R^{(1d)}(-z_2)$. The resulting filter pair will have support sizes of $(8N_T - 3, 8N_T - 3)$ and $(12N_T - 5, 12N_T - 5)$.

Figure 27 depicts the frequency responses of the fan filter pairs using both double-halfband (with support size of $(23, 23)$ and $(45, 45)$) and triple-halfband (with support size of $(29, 29)$ and $(43, 43)$) ladder structures. It is clear that the triplet filter bank yields smoother fan filters and consequently introduces less visible ringing artifacts when employed in the DFBs.

One of the issues affecting the efficiency of a transform is the regularity of its filters [55]. Since HWD is composed of two filter bank stages, its regularity is dependent on the

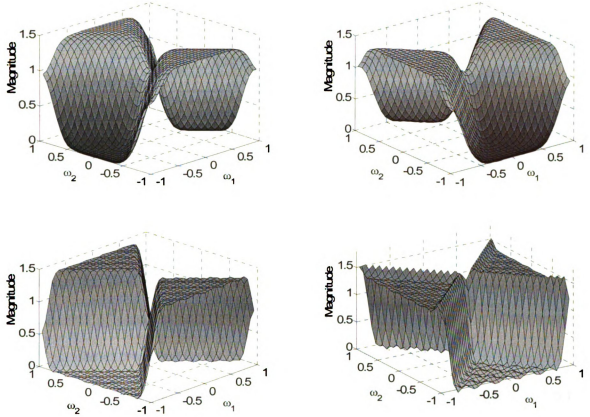


Figure 27. *Top:* The fan filter pair using triplet filter bank [1]. *Bottom:* The fan filter pair using double-halfband filter bank [72].

regularity of both wavelets and DFBs. While the regularity of DFBs needs a comprehensive treatment, here we resort to performing a simple test.

The largest first-order difference of the coefficients of the iterated filter bank in the lowpass channel (which leads to an approximate of the scaling function) is an indication of the regularity [55], [56]. Here we measure the largest first-order difference when we apply an l -level DFB to the wavelet scaling function. We approximate φ by 7 iterations of the Daubechies 9/7 analysis filter and apply both double- and tippel-halfband DFBs with *normalized* filters and l levels to φ . Table 2 shows the maximum value of the first-order differences obtained for all the DFB subbands in the n_1 and n_2 directions. As seen

Table 2
Largest First-Order Difference of the DFB When Applied to φ

DFB level (l)	No DFB	2	3	4
DFB (THF) ¹	0.0239	0.0245	0.0320	0.0431
DFB (DHF) ²	0.0239	0.0466	0.0815	0.1479

¹DFB using normalized triple-halfband filters

²DFB using normalized double-halfband filters

and expected, it is clear that the DFB with triple-halfband filters has more regularity.

In what follows, we examine the complexities of the proposed schemes.

D. Complexity

Since the HWD transforms are composed of two stages, we first express the complexities of wavelets and DFBs. Here we evaluate the complexities of the analysis banks; similar expressions for the synthesis banks can be derived.

1) WT: Suppose that we use analysis 1-D filters of a same even length, ℓ_h , in the 2-D WT. Then the complexity of a *single-level* WT is $2\ell_h$ *multiplications per input sample* (MPS) and $2\ell_h - 2$ *additions per input sample* (APS). If we use *linear-phase* filters, we have ℓ_h MPS and $2\ell_h - 2$ APS in the WT. For an *octave-band* WT, the complexity will be up to $4/3$ times the complexity of a single-level WT [92].

2) DFB: Regarding the ladder network shown in Figure 26, the complexity of the QFB is evaluated as follows. Since at each channel we decrease the number of samples by 2 and we have three levels of separable convolution with 1-D T -filters having a length of ℓ_r , the complexity of the QFB is $3\ell_r + 1$ MPS and $3\ell_r - 3/2$ APS. For the *linear-phase* maximally flat filters that we use in this work, we have $3N_T + 1$ MPS and $3N_T - 3/2$ APS ($N_T = \ell_r / 2$) for the QFB. For a J -level octave-band QWT, we

have $2(1 - 1/2^J)$ times the complexity of the QFB.

The complexity of an l -level DFB is l times that of the QFB (note that after each level the size of the signal is halved). A half-tree DFB needs $(l + 1)/2$ times the operations required for the QFB.

3) HWD: Suppose that in the HWD (considering linear-phase filters), we apply l_j -level DFBs ($1 \leq j \leq J_m$) to the j th highpass channels of the WT. Then the complexity of HWD-F is about

$$(4/3)\ell_h + 3(3N_T + 1)\sum_{j=1}^{J_m} (l_j / 4^j) \text{ MPS}$$

and

$$(4/3)\ell_h + 9(N_T - 1/2)\sum_{j=1}^{J_m} (l_j / 4^j) \text{ APS.}$$

In the case of HWD-H, the complexity is about

$$(4/3)\ell_h + (3N_T + 1)\sum_{j=1}^{J_m} ((2l_j + 1)/4^j) \text{ MPS}$$

and

$$(4/3)\ell_h + 3(N_T - 1/2)\sum_{j=1}^{J_m} ((2l_j + 1)/4^j) \text{ APS.}$$

And for the HQWD we have

$$(3N_T + 1)\left(2(1 - 1/2^J) + \sum_{j=1}^{J_m} (l_j / 2^j)\right) \text{ MPS}$$

and

$$3(N_T - 1/2)\left(2(1 - 1/2^J) + \sum_{j=1}^{J_m} (l_j / 2^j)\right) \text{ APS.}$$

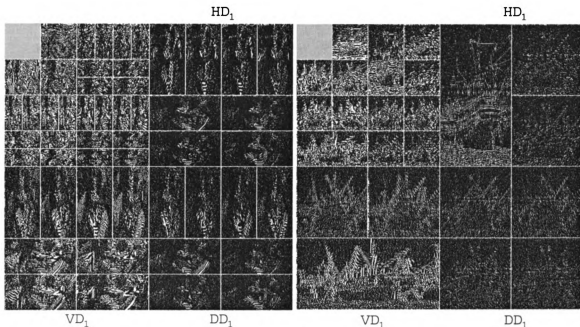


Figure 28. *Left*: The HWD-F transform of the *Barbara* image. Here $J = 3$, $J_m = 2$, and $l_1 = l_2 = 3$.

Right: The HWD-H transform of the *Boats* image with $J = 3$, $J_m = 2$, and $l_1 = l_2 = 2$.

3.5 APPLICATIONS AND RESULTS

In this section we show examples of the HWD transforms and then present potential applications of the proposed transforms. Particularly, we examine their applications in nonlinear approximation, image coding, and image denoising.

Figure 28 depicts two examples of the HWD transforms of the *Barbara* and *Boats* images. In this figure the wavelet subbands are separated with white lines and the directional subbands at the two finest wavelet subbands are separated with gray lines. The transform coefficients are clipped for better visualization.

A. Nonlinear Approximation

Nonlinear approximation (NLA) is an efficient approach to measure the capability of

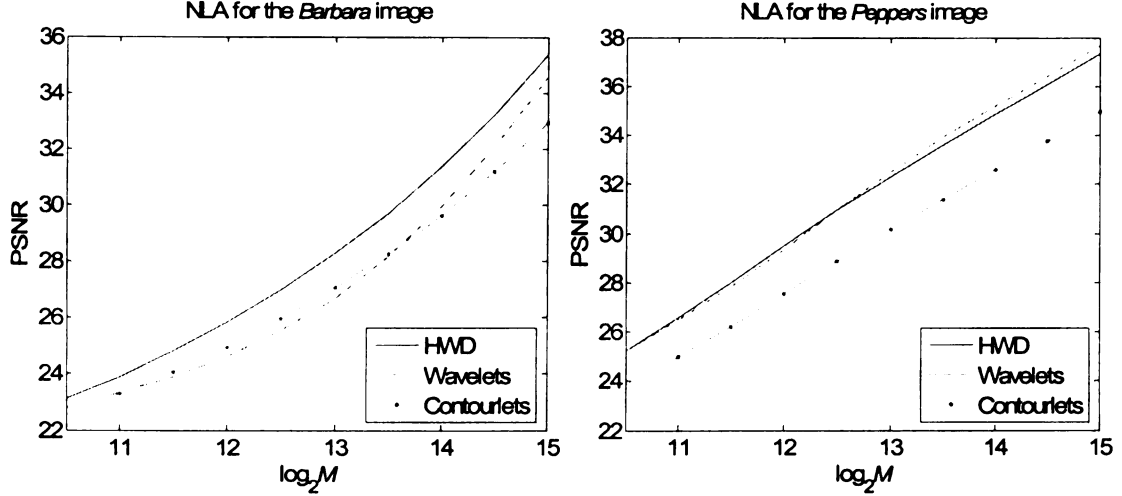


Figure 29. Examples of the nonlinear approximation PSNR results. *Left*: The NLA results for the *Barbara* image. *Right*: The NLA results for the *Peppers* image.

a transform in sparse representation of a signal. Having a good NLA behavior, a transform would have potential in several signal processing applications such as coding, denoising, and feature extraction.

We tested our proposed transforms using a variety of images and compared them with other transforms such as the WT and contourlets [28]. We used five decomposition levels in all methods and employed Daubechies 9/7 filters for the WT. For the HWD transforms we set $J_m = 2$. For contourlets we used $\{l_j\}_{1 \leq j \leq 5} = \{5, 4, 4, 3, 3\}$ ($j = 1$ corresponds to the finest scale) directional levels. Figure 29 shows two examples of the NLA PSNR results versus the number of retained coefficients. For the *Barbara* image we used HWD-F with $l_1 = l_2 = 3$ directional levels while for the *Peppers* image (and other images that contain less texture) we used HWD-H with $l_1 = l_2 = 2$.

The proposed HWD transform shows promising results for the *Barbara* image (and other images with significant texture content) where it consistently outperforms both

Table 3
PSNR Values of the NLA Experiment for the *Barbara* Image

Method / M	2048	4096	8192	16374	32768
HWD (THF) ¹	23.91	25.86	28.28	31.35	35.39
HWD (DHF) ²	23.87	25.73	28.05	30.95	34.73
Wavelets	23.33	24.63	26.68	29.95	34.58
Contourlets [28]	23.29	24.95	27.08	29.63	32.91

¹HWD using triple-halfband filters

²HWD using double-halfband filters

wavelets and contourlets. In particular, it achieves up to 1.6 dB (1.2 dB) improvement over the WT (contourlet transform). In the case of the *Peppers* image, the HWD transform provides comparable result to that of wavelets. Note that for many other images such as *Boats*, *Fingerprint*, *GoldHill*, *Mandrill*, and texture images our experiments indicated that HWD always provides better NLA performance.

Some numerical values for the NLA of the *Barbara* image are also given in Table 3. To demonstrate the effect of employing regular fan filters in HWD, we also provided the HWD results when using double-halfband filters. The superior results especially for large values of M are clear for the HWD transform using maximally flat triple-halfband fan filters.

Figure 30 shows the visual results of NLA of the *Barbara* image when $M = 8192$. As seen, the proposed HWD method provides better detail in conjunction with an acceptable level of artifacts in the result.

Our experiments implied that the HWD-H is more appropriate for images that are mostly smooth, whereas HWD-F provides very good performance for images containing a significant amount of fine textures.

We also performed NLA for the HQWD transform and compared it with the quincunx wavelet transform. Table 4 shows the PSNR values obtained for the *Barbara* image. As seen, HQWD provides a growing improvement in the PSNR values as the

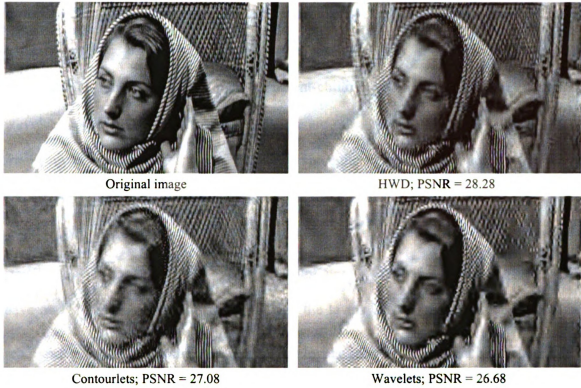


Figure 30. Example of the NLA visual results for the *Barbara* image when $M = 8192$.

Table 4
PSNR Values of the NLA Experiment for the *Barbara* Image (Quincunx Case)

Method / M	2048	4096	8192	16374	32768
HQWD	22.21	23.69	25.59	28.18	31.90
Quincunx WT	21.95	23.06	24.54	26.64	30.06

number of retained coefficients increases. In this experiment we used ten wavelet levels and for the HQWD we used $J_m = 4$ and $l_j = 3$ ($1 \leq j \leq J_m$).

B. Image Coding

Due to the good NLA performance of the HWD family and since this transform family is nonredundant, a potential key application for the proposed transforms is image coding.

Although the NLA decay rate of wavelets for images is suboptimal, one can benefit

from tree-based coding schemes to improve this decay rate [20]. The SPIHT algorithm is an efficient tree-based wavelet coding scheme [78]. In this scheme, inter-scale dependencies are considered through the parent-children relationships existing among the wavelet coefficients. Note that although there are other superior schemes such as space-frequency quantization [94] and WSFQ [93], since the scope of this chapter is not image coding, we just provide our preliminary results using SPIHT coding algorithm.

To take advantage of the SPIHT scanning algorithm for the HWD transform coefficients, a new parent-children relationship should be considered. Suppose that we have an HWD transform with J levels. For the levels $J_m < j \leq J$, we have the same relationship as the one in the WT, and for the levels $1 \leq j \leq J_m$, for each subband HD_j , VD_j , and DD_j we can use a similar parent-children relationship as the one considered for the contourlet coefficients [74]. The problem appears when we attempt to define the children of coefficients lying at level $J_m + 1$. By applying DFBs to level J_m , we almost remove the inter-scale dependencies that existed between wavelet levels J_m and $J_m + 1$. Nevertheless, we employ a suboptimal but simple rearrangement algorithm to be able to apply a similar SPIHT scanning algorithm as the one we use for wavelets (*see* Appendix A3 for detail).

Although the described procedure is not optimal, we will show that the low bit-rate SPIHT coding results are rather promising for images with high amount of textures and details, where we could capture more details in the HWD coded images when compared with the wavelet coder. In our coding simulation, we used the image *Barbara* and an image composed of 16 textures [9]. For both images we used HWD-F with 5 wavelet

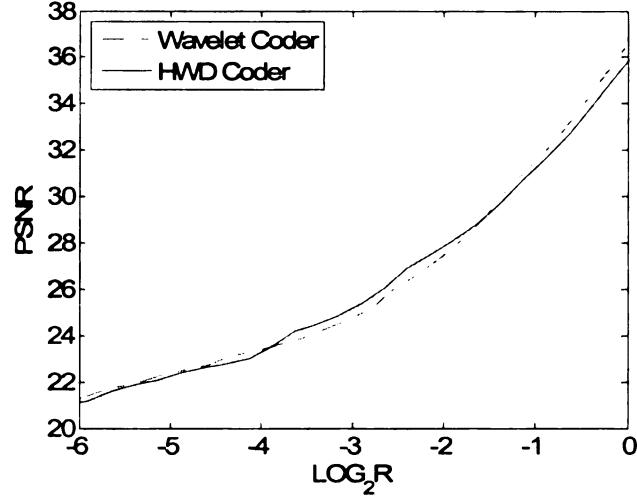


Figure 31. Coding performance of the wavelet and HWD coders using SPIHT algorithm in terms of PSNR versus the rate for the *Barbara* image.

levels and $J_m = 2$, where for the *Barbara* image we used $l_1 = l_2 = 3$ directional levels and $l_1 = l_2 = 4$ directional levels for the *Texture16* image. The number of directional levels is handy-optimized.

In Figure 31 we show the RD curves of the wavelet and proposed coding schemes for the *Barbara* image. As seen, our method provides better or comparable result for a wide range of low bitrate when compared with the wavelet SPIHT coder. Remarkably, unlike the NLA performance of HWD in comparison to that of wavelets, the coding performance does not show significant improvement, which indicates a need for more sophisticated algorithms that we would address later.

Figure 32 shows visual coding results of the *Barbara* image at 0.25 bpp and the results for *Texture16* at 0.1 bpp are depicted in Figure 33. As can be seen from the figures, more directional features are retained when using the HWD transform (for example table cover and chair in Figure 32). Further, we have improved PSNR values compared with those of the wavelet coder.



Wavelets/SPIHT; PSNR = 27.45



HWD-F/SPIHT; PSNR = 27.83

Figure 32. Coding results of the *Barbara* image at rate 0.25 bpp.

C. Image Denoising

Image denoising is another application of the HWD transforms. We tested the proposed transforms for denoising of noisy images corrupted with additive white Gaussian noise. For the first part of simulation, we used a simple hard-thresholding rule to shrink the transform coefficients. This way we can observe to what extent the transform is efficient without the use of more complex shrinkage schemes. The threshold is selected as 3σ [60] where σ is the standard deviation of the input noise and is estimated using robust median estimator [32].

We also mirror-extended the images to remedy boundary artifacts. Although the sizes of the noisy images are rather large, the PSNR values of the denoising results change slightly (usually up to ± 0.1 dB) when we use a different noise instance. Hence, to obtain more accurate PSNR values, we repeated each denoising experiment ten times and found the average PSNR values. We also clipped the noisy images to set the pixel values in the

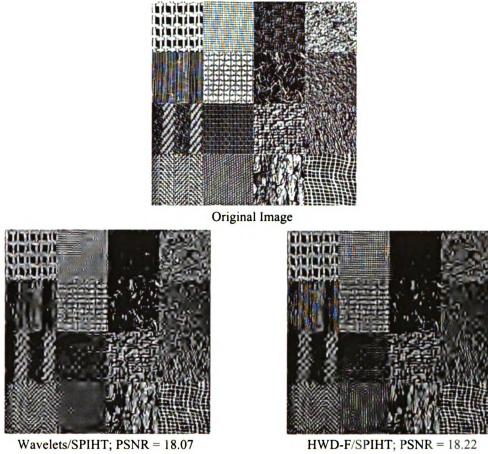


Figure 33. Coding results of the *Texture16* image at rate 0.1 bpp.

allowable range of 0 to 255.

Since the HWD transforms are shift variant, they introduce many artifacts in the denoising results. Therefore, we also constructed *translation-invariant HWD* (TIHWD) transforms by removing subsampling operations to improve the results. A delicate point in developing the TIHWD schemes, is that we should not change the frequency partitioning of the HWD transforms (see Figure 21). As a result, we first upsample the DFB filters at level j ($1 \leq j \leq J_m$) by M^j , where $M = \text{diag}(2, 2)$ and then remove the sampling operations using the *generalized algorithme à trous* introduced in [36], [44].

In addition to the proposed methods, we also employed the *wavelet transform* (WT),

Table 5
PSNR Values of the Denoising Experiments

Left Part: Different Transforms With Hard Thresholding											Right Part: Different Denoising Methods			
Image	σ	Noisy Image	WT	CT [28]	CuTFW [11]	HWD	TIWT	DTCWT [53]	TICT [36]	TIHWD	DTCWT (BS)[80]	STICT (BS)[36]	BLS-GSM[73]	TIHWD (BS)
Barbara	10	28.13	29.86	29.78	29.71	30.07	32.58	32.66	33.49	33.70	33.50	34.42	34.40	34.46
	20	22.15	25.80	26.31	25.89	26.58	28.26	28.93	29.53	30.01	29.78	30.59	30.60	30.78
	40	16.38	22.44	22.94	23.67	23.16	24.53	25.02	25.70	26.33	26.35	26.77	26.70	27.15
	60	13.30	20.99	21.04	22.60	21.21	22.82	23.00	23.57	23.96	24.28	24.48	24.41	24.84
Boats	10	28.14	30.76	30.30	31.44	30.86	33.32	33.24	33.59	33.70	34.02	34.35	34.69	34.50
	20	22.18	27.21	26.88	28.66	27.29	29.75	29.80	30.03	30.13	30.63	30.73	31.14	30.96
	40	16.42	23.83	23.55	25.82	23.82	26.32	26.20	26.49	26.66	27.36	27.15	27.65	27.48
	60	13.37	21.94	21.53	23.96	21.77	24.17	23.98	24.26	24.42	25.25	24.87	25.43	25.24
GoldHill	10	28.13	29.97	29.72	30.86	30.02	32.07	31.98	32.10	32.36	32.82	32.98	33.27	33.25
	20	22.17	26.98	26.84	28.43	27.05	29.17	29.16	29.16	29.44	29.97	29.93	30.31	30.22
	40	16.41	23.93	23.82	25.87	24.00	26.32	26.02	26.35	26.63	27.26	27.01	27.49	27.37
	60	13.34	22.09	21.88	24.22	22.08	24.40	23.94	24.57	24.71	25.40	25.05	25.54	25.44
Lena	10	28.13	32.10	31.58	33.46	32.08	34.53	34.71	34.89	34.73	35.30	35.44	35.60	35.39
	20	22.13	28.58	28.16	30.59	28.59	31.35	31.45	31.75	31.60	32.35	32.30	32.63	32.40
	40	16.35	24.97	24.64	27.27	24.92	27.83	27.67	28.22	28.17	29.24	28.82	29.39	29.15
	60	13.27	22.94	22.42	25.29	22.73	25.50	25.25	25.82	25.80	26.96	26.38	27.03	26.78
Peppers	10	28.25	31.83	31.04	32.54	31.69	33.91	33.99	34.00	33.95	34.27	34.43	34.57	34.44
	20	22.32	28.49	27.89	29.67	28.43	30.97	30.91	31.15	31.18	31.49	31.60	31.92	31.72
	40	16.59	24.47	24.09	26.20	24.46	27.06	26.79	27.26	27.44	28.00	27.77	28.21	28.14
	60	13.53	22.00	21.64	23.91	21.91	24.38	24.04	24.56	24.71	25.41	25.04	25.42	25.44

contourlet transform (CT) [28], and adaptive wiener filter using “wiener2” function in Matlab. Moreover, we used the *curvelet transform via frequency wrapping* (CuTFW) [11] (where we found that it gives better denoising results than curvelets via unequispaced FFT approach), *translation-invariant WT* (TIWT) [22], *dual-tree complex wavelet transform* (DTCWT) [53], and *translation-invariant CT* (TICT) (see Chapter 2) using hard thresholding for the sake of comparison. Except for the *Barbara* image that we used HWD-F with $l_1 = l_2 = 3$, for the other images we used HWD-H with $l_1 = l_2 = 2$. Similar to the NLA experiment, for contourlets we used $\{l_j\}_{1 \leq j \leq 5} = \{5, 4, 4, 3, 3\}$ directional levels.

The left part of Table 5 shows the PSNR values of the denoising results for different images and noise levels using hard thresholding. As seen, the HWD transform yields in



TIWT; PSNR = 30.97



DTCWT; PSNR = 30.91



TIHWD; PSNR = 31.18

Figure 34. Denoising results of the *Peppers* image when $\sigma = 20$.

better PSNR values than the CT. Moreover, for the *Barbara* image it achieves superior results when compared with the WT. In the case of *translation-invariant* (TI) denoising, we see that the proposed TIHWD denoising scheme almost always provides better results (improvements up to 1.80 dB) when compared with the TIWT and DTCWT schemes. Moreover, it outperforms curvelet (CuTFW) denoising scheme.

As an example of the visual results for this part of denoising, in Figure 34 we show the TI denoising results of the *Peppers* image when $\sigma = 20$. We see that the TIHWD scheme provides less visible artifacts in the denoised image.

In the second part of denoising experiment, we took advantage of the *bivariate shrinkage* (BS) scheme with local variance estimation [80] for TIHWD, where we also used this approach for *semi-translation invariant contourlet transform* (STICT) described in Chapter 2. For TIHWD (BS) we used a window size equal to (17, 17) for estimation of local variance whereas we used a window with size (5, 5) for STICT (BS). We also compared our method to some other leading denoising approaches: DTCWT (BS) [80] and BLS-GSM (Bayes least squares using Gaussian scales mixtures) [73].

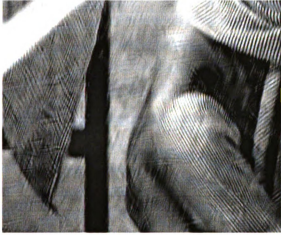
The right part of Table 5 shows PSNR values resulting from the above methods. We see that for the image *Barbara*, our TIHWD (BS) denoising scheme provides better



TIHWD (BS); PSNR = 30.78



BLS-GSM [73]; PSNR = 30.60



STICT (BS) [44]; PSNR = 30.59



DTCWT (BS) [80]; PSNR = 29.78

Figure 35. Denoising results of the *Barbara* image when $\sigma = 40$.

results whereas for other images it shows comparable performance (within 0.25 dB). Our results are also comparable to those reported in [23] for NSCT-LAS (nonsampled contourlet transform using local adaptive shrinkage).

Figure 35 demonstrates a visual example for this part for the *Barbara* image and noise level of $\sigma = 40$. It clearly shows the superior performance of the TIHWD in retaining details along with introducing fewer (or comparable) artifacts in the result.

3.6 CONCLUSION

We proposed a new family of nonredundant geometrical image transforms by employing wavelets and directional filter banks. We showed that to avoid artifacts introduced during nonlinear approximation (and thus coding and denoising), we should change the wavelet basis functions in only a few finest wavelet scales. This way we take advantage of both directional and nondirectional basis functions to efficiently represent natural images. The proposed family benefit from a number of essential characteristics. They are nonredundant and at the same time provide promising nonlinear approximation behavior for natural images especially those having a significant amount of periodic texture. Consequently, they have potential for image coding. In the experiments, we employed the proposed transform family in nonlinear approximation, image coding, and image denoising and demonstrated their efficiency in these applications.

Chapter 4

ON THE LINEAR COMBINATION OF DENOISING SCHEMES

4.1 INTRODUCTION

As have been highlighted in previous chapters of this thesis, wavelets have proven their capability in removing noise from a piece-wise smooth signal [60]. Under wavelet denoising with hard thresholding, one simply sets to zero the transform coefficients of the noisy signal, which are below a threshold, and reconstructs the resulting coefficients to obtain the denoised signal.

Recently, several new image transform schemes have been introduced, where most of them take advantage of the important feature of directionality. Following a similar procedure to the wavelet denoising scheme, one can employ other transforms for denoising [36], [44].

Owing to the characteristics of a transform, a transform-domain denoising scheme introduces some artifacts in the denoising results that are different from those of other schemes. Furthermore, each denoising scheme may have some advantages over the others

and also some drawbacks. As a consequence, combination of different schemes would be a solution to reduce artifacts and to compensate for the drawbacks. Taking advantage of the same idea, the authors in [22] proposed translation-invariant (TI) wavelet denoising, where it is, in effect, equivalent to the average of all denoised images resulting from the cycle-spinning algorithm. In [36] we have shown that the pseudo-Gibbs phenomena artifacts that usually appear in the denoising results when we use the contourlet transform [28] denoising scheme, can be significantly reduced. In this chapter, however, we use a different strategy that is based on a linear optimization approach in conjunction with employing *different* denoising schemes, where we extend our preliminary work [41].

The remainder of the chapter outline is as follows. In the next section we briefly highlight some of the related work. Section 4.3 provides problem formulation for our proposed linear combination method. The experimental results are provided in Section 4.4 and finally Section 4.5 concludes the chapter.

4.2 RELATED WORK

In a general framework, where one wishes to find an optimal representation over a *dictionary* of bases functions, a few algorithms have been proposed [51]. Suppose that $\mathcal{D} = \{\mathcal{B}_1, \dots, \mathcal{B}_M\}$ is the dictionary of the bases functions, where \mathcal{B}_i is the matrix corresponding to the i th basis and we want to decompose a signal x (given in a row vector of length N) using the dictionary \mathcal{D} . Therefore, we have

$$x = \sum_{i=1}^M \alpha_i \mathcal{B}_i,$$

where $\{\alpha_i\}_{1 \leq i \leq M}$ are the arrays of coefficients and $\alpha_i = (\alpha_{i1}, \dots, \alpha_{iN})$. The *method of frames* [25], provides α with a minimized ℓ_2 norm. *Basis pursuit* [18] is another

algorithm, which optimizes α subject to ℓ_1 norm; and hence, results in a linear programming approach. *Matching pursuit* [63] attempts to find a *best* basis in \mathcal{D} utilizing a greedy algorithm. It sequentially adds elements from \mathcal{D} that are most correlated with the residual. The above methods, however, are computationally expensive.

Total variation is a technique employed to denoising [77] and later was combined with traditional wavelet decompositions to reduce artifacts in wavelet denoising [16], [33]. Using the same idea, the authors in [15] applied the curvelet transform in conjunction with total variation to improve the denoising results of curvelets. Starck *et al.* [87] proposed an algorithm to combine several transforms, where they used an iterative approach to minimize an ℓ_1 norm instead of total variation norm.

Our approach, however, is based on a linear combination of the denoising results and thus is not complex. Meanwhile, the proposed approach provides improvement in the PSNR values and, more importantly, in visual quality due to significant reduction of the artifacts. Here we assume that the image is corrupted with an additive white Gaussian noise.

4.3 OPTIMAL LINEAR COMBINATION

A. Optimal LMS Approach

We wish to find an analytical solution to the following problem. Suppose that an image denoted by a row vector $\tilde{\mathbf{x}} \in \mathbb{R}^{1 \times N}$ with size N is corrupted with an additive zero-mean white Gaussian noise $\tilde{\mathbf{z}} = \tilde{\mathbf{x}} + \mathbf{v}$. Note that we use boldface for random variables and random vectors and a tilde sign for a variable that does not have zero mean.

Now we employ M different denoising schemes to the noisy image to obtain the denoised signals $\{\tilde{\mathbf{y}}_1, \tilde{\mathbf{y}}_2, \dots, \tilde{\mathbf{y}}_M\}$, where $\tilde{\mathbf{y}}_i \in \mathbb{R}^{1 \times N}$. Assuming that none of the denoised signals is an exact copy of the original signal, which is usually the case because of the artifacts introduced by the denoising schemes and also because of the remaining noise in the denoising results, we wish to find a better estimation $\hat{\mathbf{x}}$ of the image \mathbf{x} using the denoised images $\{\tilde{\mathbf{y}}_1, \tilde{\mathbf{y}}_2, \dots, \tilde{\mathbf{y}}_M\}$. In this work, we are only interested in the linear estimation approach. To obtain more compact equations, we centralize the random vectors $\tilde{\mathbf{x}}$ and $\{\tilde{\mathbf{y}}_i\}_{1 \leq i \leq M}$ around their means $m_{\tilde{\mathbf{x}}} = \text{mean}(\tilde{\mathbf{x}}) = 1/N \sum_{n=1}^N \tilde{x}[n]$ and $m_{y_i} = \text{mean}(\tilde{\mathbf{y}}_i) = 1/N \sum_{n=1}^N \tilde{y}_i[n]$ as

$$\mathbf{x} = \tilde{\mathbf{x}} - m_{\tilde{\mathbf{x}}} \mathbf{1}_{1 \times N}, \quad \text{and} \quad \mathbf{y}_i = \tilde{\mathbf{y}}_i - m_{\tilde{\mathbf{y}}_i} \mathbf{1}_{1 \times N}, \quad (4.1)$$

where $\mathbf{1}_{M \times N}$ is a matrix of size $M \times N$ with all entries equal to one.

Using the denoising results, we are interested in a linear estimation of \mathbf{x} ,

$$\hat{\mathbf{x}} = \sum_{i=1}^M k_i \mathbf{y}_i,$$

and therefore a vector of coefficients $K = (k_1, \dots, k_M)$ in order to minimize the variance of error $\mathbf{e} = \mathbf{x} - \hat{\mathbf{x}}$ (note that the variance of error is a scalar):

$$K_o = \arg \min_K \left\{ \|\mathbf{e}\|^2 \right\} = \arg \min_K \left\{ E[\mathbf{x} - \hat{\mathbf{x}}][\mathbf{x} - \hat{\mathbf{x}}]^T \right\},$$

where $(.)^T$ denotes the transpose operation. This is the well-known problem of optimal linear estimation in a *least-mean-squares* (LMS) sense. Note that we define the inner product of two random vectors as the expectation:

$$\langle \mathbf{x}, \mathbf{y} \rangle = E[\mathbf{xy}^T] = C_{xy}, \quad \text{and} \quad \|\mathbf{x}\|^2 = \langle \mathbf{x}, \mathbf{x} \rangle = E[\mathbf{xx}^T] = \sigma_x^2.$$

Hence, we can express the above equations in terms of inner products where it is straightforward to switch between deterministic and stochastic cases.

Defining the matrix of the denoising results as $\mathbf{y} = (\mathbf{y}_1^T, \dots, \mathbf{y}_M^T)^T \in \mathbb{R}^{M \times N}$, we can find the optimal LMS estimator coefficients K_o as [52]

$$K_o = C_{xy} C_y^{-1}, \quad (4.2)$$

where

$$C_y = E[\mathbf{yy}^T] = \left(E[\mathbf{y}_i \mathbf{y}_j^T] \right)_{\substack{i=1, \dots, M \\ j=1, \dots, M}} \in \mathbb{R}^{M \times M},$$

is the covariance matrix of \mathbf{y} and

$$C_{xy} = E[\mathbf{xy}^T] = \begin{pmatrix} E[\mathbf{xy}_1^T] & \dots & E[\mathbf{xy}_M^T] \end{pmatrix} \in \mathbb{R}^{1 \times M},$$

denotes the cross-covariance matrix. Therefore, using the computed coefficients in (4.2), we find the optimal LMS estimation as

$$\hat{\mathbf{x}}_o = K_o \mathbf{y} = C_{xy} C_y^{-1} \mathbf{y}. \quad (4.3)$$

Further, the minimum mean-square error is found to be [52]

$$\|\mathbf{e}_o\|^2 = \sigma_x^2 - C_{xy} C_y^{-1} C_{yx}.$$

It follows from (4.1) that the optimal estimated image is

$$\begin{aligned} \hat{\mathbf{x}}_o &= m_{\tilde{x}} \mathbf{1}_{1 \times N} + K_o (\tilde{\mathbf{y}} - m_{\tilde{y}}) \\ &= m_{\tilde{x}} \mathbf{1}_{1 \times N} + C_{xy} C_y^{-1} (\tilde{\mathbf{y}} - m_{\tilde{y}}), \end{aligned}$$

where $C_y = C_{\tilde{y}}$, $C_{xy} = C_{\tilde{x}\tilde{y}}$, and $m_{\tilde{y}} = (m_{\tilde{y}_1}^T, \dots, m_{\tilde{y}_M}^T)^T \in \mathbb{R}^{M \times N}$.

While the above LMS method provides optimal coefficients to combine the denoising results, its dependence on the statistical properties of the original image $\tilde{\mathbf{x}}$ makes this approach unattainable in practice. Nevertheless, we use this *oracle* approach for the sake of comparison.

Note that in the above formulation, we used only one coefficient k_i to scale all pixels in a denoising result \mathbf{y}_i . The reason for this is to facilitate developing a *non-oracle* method to find a set of *near* optimal coefficients.

B. LMS Approach using the Noisy Signal

Since finding the optimal coefficients K_o as given in (4.2) is subject to having the original signal, we need to develop other approaches that do not rely on having knowledge of the original signal. One approach is to use the noisy image instead of the original. (Note that the noisy signal is the maximum likelihood estimation of the original signal [7].) Therefore, the *suboptimal* estimated (removed-mean) image $\hat{\mathbf{x}}_{no}$, and the corresponding coefficient vector K_{no} , are expressed as

$$\hat{\mathbf{x}}_{no} = K_{no} \mathbf{y} \quad \text{and} \quad K_{no} = C_{zy} C_y^{-1}. \quad (4.4)$$

Note that, since $\mathbf{z} = \tilde{\mathbf{z}} - m_{\tilde{\mathbf{x}}} \mathbf{1}_{1 \times N}$ and thus $\mathbf{z} = \mathbf{x} + \mathbf{v}$, we have $\sigma_z^2 = \sigma_x^2 + \sigma_v^2$, $C_{zy} = C_{xy} + C_{vy} \in \mathbb{R}^{1 \times M}$, and also $C_{yz} = C_{yx} + C_{yv} \in \mathbb{R}^{M \times 1}$. Consequently, we can calculate the covariance of the error (associated with the noisy signal) as

$$\|\mathbf{e}_{no}\|^2 = \|\mathbf{e}_o\|^2 + \sigma_v^2 - C_{vy} C_y^{-1} (C_{yx} + C_{yv}) - C_{xy} C_y^{-1} C_{yv}. \quad (4.5)$$

Since the denoising schemes usually take advantage of nonlinear approaches to

remove noise, it is not trivial to find statistical measures such as C_{xy} and C_{vy} ; hence, we attempt to use approximate values. If we assume that $\mathbf{y}_i \approx \mathbf{x}$ ($1 \leq i \leq M$), we can express (4.5) as

$$\begin{aligned} \|\mathbf{e}_{no}\|^2 - \|\mathbf{e}_o\|^2 &\approx \sigma_v^2 - 2\sum_{i=1}^M C_{vy_i} - C_{vy}C_{yv} \\ &\approx \sigma_v^2 - 2\sum_{i=1}^M C_{vy_i} - \sum_{i=1}^M C_{vy_i}^2. \end{aligned} \quad (4.6)$$

In addition, it is reasonable to assume that there is low correlation between the noise \mathbf{v} and the denoised signals \mathbf{y} . Meanwhile, we always have $\|\mathbf{e}_{no}\|^2 - \|\mathbf{e}_o\|^2 \geq 0$. It follows that the variance of the noise is the dominant term in (4.6), and hence, for a rather good estimation of the signal using the proposed approach given in (4.4), we should ensure that the power of the input noise is low.

C. Approximation to the Optimal LMS Approach

Now we consider another method to this linear estimation problem. Here we suppose that the denoised signals are corrupted versions of the original signal with additive distortions expressed as $\tilde{\mathbf{y}}_i = \tilde{\mathbf{x}} + \tilde{\boldsymbol{\eta}}_i$ ($1 \leq i \leq M$) or equivalently after removing the mean values we have

$$\mathbf{y}_i = \mathbf{x} + \boldsymbol{\eta}_i \quad (1 \leq i \leq M),$$

where $\boldsymbol{\eta}_i \in \mathbb{R}^{1 \times N}$ is the distortion vector due to the artifacts and remaining noise in the denoised signal \mathbf{y}_i . In particular, we assume that the denoised signal is linearly related to the original signal. We also assume that $\boldsymbol{\eta}_i$ ($1 \leq i \leq M$), is uncorrelated with \mathbf{x} .

Denoting $\boldsymbol{\eta} = (\boldsymbol{\eta}_1^T, \dots, \boldsymbol{\eta}_M^T)^T \in \mathbb{R}^{M \times N}$, we can write $\mathbf{y} = \mathbf{1}_{M \times 1} \mathbf{x} + \boldsymbol{\eta}$. The linear LMS

solution [52] to this problem is found to be

$$\hat{\mathbf{x}}_o = K_o \mathbf{y}, \quad \text{with} \quad K_o = \left(\|\mathbf{x}\|^{-2} + \mathbf{1}_{1 \times M} C_\eta^{-1} \mathbf{1}_{M \times 1} \right)^{-1} \mathbf{1}_{1 \times M} C_\eta^{-1}.$$

By assuming $\|\mathbf{x}\| \gg 1$, we obtain the Fisher estimation of \mathbf{x} as

$$\hat{\mathbf{x}}_F = \left(\mathbf{1}_{1 \times M} C_\eta^{-1} \mathbf{1}_{M \times 1} \right)^{-1} \mathbf{1}_{1 \times M} C_\eta^{-1} \mathbf{y}, \quad (4.7)$$

and

$$\|\mathbf{e}_F^2\| = \left(\mathbf{1}_{1 \times M} C_\eta^{-1} \mathbf{1}_{M \times 1} \right)^{-1}.$$

Note that although there is no explicit dependence on the signal \mathbf{x} in (4.7), we have no prior knowledge of C_η . Meanwhile, it is important to note that when deploying different denoising schemes, one would target a variety of such schemes that generate different types of artifacts. Ideally, the resulting artifacts from the different denoising schemes are uncorrelated. Therefore, under such scenario, we can assume that $C_\eta \approx I$, which results in the estimation

$$\hat{\mathbf{x}}_a = \frac{1}{M} \mathbf{1}_{1 \times M} \mathbf{y} = \frac{1}{M} \sum_{i=1}^M \mathbf{y}_i, \quad (4.8)$$

and $\|\mathbf{e}_a^2\| = 1/M$. That is, $\hat{\mathbf{x}}_a$ is obtained through averaging the denoised images (where we assumed that $\mathbf{m}_{\hat{\mathbf{x}}} = \text{mean}(\mathbf{m}_{\hat{\mathbf{y}}_i})$). Note that when $C_\eta = I$, $\hat{\mathbf{x}}_a$ is the optimal unbiased LMS estimation of \mathbf{x} .

As mentioned above, for the assumption $C_\eta \approx I$ to be viable, one should have $E[\eta_i \eta_j^T] \approx 0$ ($1 \leq i, j \leq M$ and $i \neq j$) and $E[\eta_i \eta_i^T] \approx 1$ ($1 \leq i \leq M$), which is the case (to some extent) when one employs different denoising schemes having comparable

performance and producing different types of artifacts.

4.4 EXPERIMENTAL RESULTS

A. *A Brief Note on the Denoising Artifacts*

Here we briefly outline the type of artifacts introduced by some different image denoising schemes to better appreciate the benefit of combining denoised image signals. Particularly, we consider denoising under the wavelet transform, contourlet transform, and adaptive Wiener filter [58]. Notice that while there exist other approaches, we have selected the above methods due to their different characteristics where each of them can be representing a different class of image denoising schemes. Remarkably, when some statistical approaches could improve the above methods, their intrinsic features that result in denoising artifacts still remain and cannot be totally eliminated.

1) Wavelet Denoising Scheme: The wavelet transform has shown its capability for denoising piece-wise smooth images [60]. Wavelets, indeed, provide unconditional bases of ℓ_2 and also of many smoothness spaces [30]. As a result, wavelet shrinkage is a smoothing operation for a wide variety of signal classes. Wavelet shrinkage in comparison to other older methods such as convolutional smoothers and Fourier-domain damping is much simpler, and offers many broad near-optimality properties not achievable by the older methods [30].

An important problem that arises in a transform-domain denoising is the artifacts introduced when one thresholds the transform coefficients. The ringing artifacts are in fact due to pseudo-Gibbs phenomena, which occur near edges and discontinuities and resemble the basis functions of the transform. Figure 36(a) shows some of the basis functions of the wavelet transform. Note that this transform is efficient in capturing point-

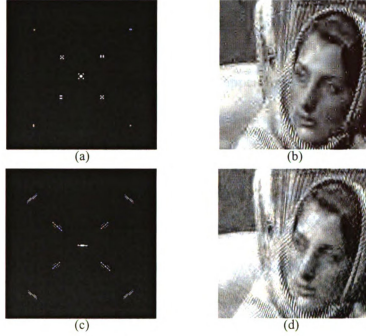


Figure 36. (a) Some basis functions of wavelets. (b) The denoising result of the *Barbara* image using wavelets ($\sigma_v = 20$). (c) Some basis functions of contourlets. (d) The denoising result of the *Barbara* image using contourlets ($\sigma_v = 20$).

wise singularities and the basis functions are like points. Therefore, the artifacts in a denoised image will look like the basis functions as shown in Figure 36(b), which depicts an example, where the standard deviation of the input noise is 20. Notably, this denoising scheme is incapable of capturing some textures and fine details and therefore, yielding another kind of distortion.

2) Contourlet Denoising Scheme: The contourlet transform, one of the geometrical image transform, is introduced to better capture directional features of an image [28]. Owing to the directionality of this transform, the basis functions are in the form of needle-shaped segments, which can be oriented in different directions as Figure 36(c) shows. Consequently, the denoising artifacts will look like arbitrarily-oriented needle-shaped

segments that are more visible in the smooth regions (see Figure 36(d)). To have sufficient directional resolution, one has to use directional filters with large support. As a result, the basis functions and thus the artifacts appear in the form of long segments, which severely degrade the quality of the denoised image. Nevertheless, the contourlet denoising scheme outperforms the wavelet approach in retaining textures and fine details in the denoising results (compare Figure 36(b) and (d)).

3) Adaptive Wiener Filtering: The Wiener filtering is a traditional denoising method, which usually leads to a lowpass filtration. This approach would be the optimal linear minimum-mean-square error estimate of the signal if $x[n]$ and $v[n]$ are samples of stationary random processes that are linearly independent from each other and their *power spectral densities* (PSD) are known [58]. Practically, however, the above assumptions do not hold. To improve the performance of this scheme, we can use adaptive filtering, where one locally estimates the PSDs of the signal and noise and estimates the signal. As a result, if $m_z^{(\Omega)}$ and $\sigma_z^{2(\Omega)}$ denote the local minimum and variance of the noisy image z in the window Ω , respectively, the local estimate $\hat{s}^{(\Omega)}$ is [58]

$$\hat{s}^{(\Omega)} = m_z^{(\Omega)} + \frac{\sigma_z^{2(\Omega)} - \sigma_v^2}{\sigma_z^{2(\Omega)}} \left(z^{(\Omega)} - m_z^{(\Omega)} \right),$$

where we assumed that v is a zero-mean white Gaussian noise.

Since this approach is a locally filtering task, it introduces artifacts, which resemble speckle noise (see Figure 38). Additionally, blurring textures and edges in the output is another kind of distortion resulting from this approach. As we enlarge the window size,

the artifacts reduce, but more edges are smeared in the denoised image.

4) Other Methods: In addition to the above methods, we also employ our proposed linear combining of multi-scheme denoising approach in conjunction with two competitive advanced denoising methods, namely, the BLS-GSM [73] (Bayes least-squares using Gaussian scales mixtures) and TIHWD (translation-invariant hybrid wavelets and directional filter banks) using *bivariate shrinkage* (BS) (see Section 3.5C). In Section 3.5C we showed that the TIHWD (BS) denoising approach provides sometimes better results in retaining fine textures than other leading approaches such as the BLS-GSM denoising method. However, BLS-GSM renders fewer artifacts in the results. Consequently, we attempt to linearly combine these two methods in order to achieve better results.

B. Results

As we mentioned earlier, to better take advantage of the proposed linear combination approach when there is no prior information of the original signal, it is advised that the denoising schemes for which we employ the LMS approach, provide comparable performances. As a result, for the first part of our experiments, we used the three denoising techniques, wavelets [60], contourlets [28], [44], and adaptive Wiener (function “wiener2” in Matlab) [58] while employing hard thresholding for the former ones. And in the second part, we used the two leading approaches of BLS-GSM [73] and TIHWD (BS) (see Chapter 3).

To test our proposed LMS approach, we selected a variety of images and used additive white Gaussian noise with $\sigma = 10, 20$, and 40. We employed all the denoising schemes with the same parameters as those reported in Section 3.5C. We assumed that σ

Table 6
PSNR Values of the Denoised Images

Image	σ	Noisy Image	Adaptive Wiener	WT (HT)	CT (HT)	LMS_O	LMS_N	LMS_A
<i>Barbara</i>	10	28.13	28.31	29.86	30.17	31.36	31.32	31.14
	20	22.15	26.44	25.80	26.49	27.74	27.43	27.68
	40	16.38	23.65	22.44	23.17	24.50	22.88	24.35
<i>Boats</i>	10	28.14	30.44	30.76	30.59	32.14	32.11	32.11
	20	22.18	28.36	27.21	27.27	29.18	28.77	29.04
	40	16.42	25.09	23.83	24.08	26.06	23.70	25.84
<i>Lena</i>	10	28.13	32.66	32.10	32.10	33.78	33.68	33.72
	20	22.13	30.00	28.58	28.91	30.89	30.05	30.72
	40	16.35	26.10	24.97	25.62	27.46	23.94	27.33
<i>Peppers</i>	10	28.25	32.87	31.83	31.53	33.53	33.46	33.31
	20	22.32	30.09	28.49	28.50	30.84	30.25	30.48
	40	16.59	25.79	24.47	24.82	27.04	24.06	26.63

WT (HT):wavelet transform with hard thresholding

CT (HT): contourlet transform with hard thresholding

LMS_O:optimal LMS method using the original image (*see* Section 4.3A)

LMS_N:LMS method using noisy image (*see* Section 4.3B)

LMS_A:method of averaging (*see* Section 4.3C)

is unknown and we estimated it using the robust median estimator [32]. Moreover, we mirror-extended the noisy images to avoid boundary distortion. Although the size of the noisy images is rather large, the PSNR values of the denoising results change slightly (usually up to ± 0.1 dB) when we use a different noise instance. Hence, to obtain more accurate PSNR values, we repeated each denoising experiment ten times using different noise realizations and evaluated the average of PSNR values. We also clipped the noisy images to set the pixel values in the allowable range of 0 to 255.

Table 6 provides the PSNR values for the first part. We refer to the optimal LMS method of Section 4.3A as LMS_O, the method of Section 4.3B as LMS_N, and finally the averaging method of Section 4.3C as LMS_A. As seen, the proposed LMS method achieves between one and two dB improvement in most cases. For low noise levels (say $\sigma = 10$), the results where the noisy image is used as the estimate of the original signal in the LMS algorithm (LMS_N) are comparable with those of the LMS_O (optimal LMS

Table 7
PSNR Values of the Denoised Images (Advanced Methods)

Image	σ	Noisy Image	BLS-GSM	TIHWD (BS)	LMS_O	LMS_N	LMS_A
<i>Barbara</i>	10	28.13	34.40	34.46	34.70	34.60	34.70
	20	22.15	30.60	30.78	30.97	30.86	30.95
	40	16.38	26.70	27.15	27.30	27.02	27.15
<i>Peppers</i>	10	28.25	34.57	34.44	34.62	34.62	34.60
	20	22.32	31.92	31.72	32.03	31.36	31.94
	40	16.59	28.21	28.14	28.73	25.95	28.32

BLS-GSM:Bayes least-squares using Gaussian scales mixtures

TIHWD (BS): ...translation-invariant HWD with bivariate shrinkage

with oracle) results. Remarkably, the averaging approach (LMS_A) provides near-optimal PSNR values. The reason is that the selected denoising methods are comparable (and the types of artifacts generated are different/uncorrelated).

Note that although the PSNR values achieved using adaptive Wiener method are usually higher than those of the wavelet and contourlet schemes, it introduces more visible artifacts in the results. That is due to the fact that the PSNR measure treats the low-frequency artifacts similar to the high-frequency ones; while, eyes are usually more sensitive to the low-frequency artifacts.

Table 7 shows the PSNR results for the second part where we employ the combining approach to the BLS-GSM and TIHWD (BS) denoising schemes. Since these methods provide much fewer artifacts, linear combination cannot improve the PSNR values significantly. Note that again, since these schemes yield close PSNR values, the averaging method yields near-optimal performance.

Now we show some visual results. Figure 37 depicts the visual results of the *Boats* image when $\sigma = 10$. We see that the distortions resulting from the denoising schemes are very different as pointed out earlier. The LMS approach shows a significant reduction in the artifacts while the salient advantages of the denoising schemes are preserved.



Figure 37. The denoising results of the *Boats* image when $\sigma = 10$. (Note that the visual results for LMS_O and LMS_N are similar to that of LMS_A.)

Further, all the LMS methods provide similar results in this case.

Another example is demonstrated in Figure 38, where we used BLS-GSM and



Original Image



TIHWD (BS) – PSNR = 27.15



BLS-GSM – PSNR = 26.70



LMS_A – PSNR = 27.15

Figure 38. The denoising results of the *Barbara* image when $\sigma = 40$.

TIHWD (BS) denoising schemes with $\sigma = 40$. As seen, using the averaging approach takes advantage of desirable features of both methods, that is, producing fewer artifacts in the BLS-GSM approach and better retaining of fine textures in the TIHWD denoising scheme.

4.5 CONCLUSION

In this chapter we proposed a method based on the least-mean-squares approach to linearly combine different denoising schemes in an optimal sense. We found the proposed scheme to be efficient in improving denoising results through significant reduction in the artifacts and hence an increase in the PSNR values. We also proposed

non-oracle methods of averaging and LMS estimation with the noisy image as special cases of linear combining, where we showed that we can achieve near-optimal results for comparable denoising schemes.

Chapter 5

FUTURE WORK

Using directional filter banks, we added more directionality to the wavelet transform and proposed the new transform family using *Hybrid Wavelets and Directional Filter Banks* (HWD). Then we employed the proposed scheme to several image processing applications. Our preliminary results indicate the potential of the proposed HWD family for image processing. We can utilize this family in several directions explained in the following sections.

5.1 IMAGE CODING

For image coding, we plan to investigate more sophisticated approaches that take care of dependencies among the HWD coefficients. For this purpose, finding appropriate statistical models is necessary.

While we can benefit from a nonadaptive and thus less-complex coding scheme using HWD family, it is possible to achieve more efficiency through applying the proposed family in an adaptive framework similar to wavelet packets. In this direction, we used an early version of the HWD family in [46].

5.2 IMAGE DENOISING

While the denoising results of the *translation-invariant HWD* (TIHWD) are quite satisfactory (see Section 3.5C), there is still room to further improve the performance of the TIHWD denoising scheme by developing more suitable shrinkage schemes for this family.

Furthermore, note that in all of the scenarios for image denoising in the thesis, we considered white Gaussian additive noise for greylevel images. Under a possible extension of our denoising approaches, we can consider nonlinear noise, non-Gaussian noise, and color images.

5.3 IMAGE WATERMARKING

Another application that the proposed family could be useful for is image watermarking. Regarding the fact that the significant HWD transform coefficients better represent edges and fine details when compared with wavelets, one could easily embed a watermark in these image components. Since the details correspond to perceptually most significant image coefficients, we expect to have a robust watermarking scheme [34], [37].

5.4 OTHER POSSIBLE AREAS FOR HWD

One can also utilize the proposed family in other applications. For example, feature extraction is a possibility for pattern recognition. Another example is 3-D image processing where the need to extend and develop a 3-D HWD transform family is inevitable.

APPENDICES

A.1 Proof of Remark 2.1 (see Section 2.3)

Let us denote the output of channel i for each shift \mathbf{k}_c as: $s_{ic}[\mathbf{n}]$, for $0 \leq i < N$, and $0 \leq c \leq d_M - 1$, and the set of outputs of channel i as: $s_i[\mathbf{n}] = \{s_{i0}[\mathbf{n}], \dots, s_{i(d_M-1)}[\mathbf{n}]\}$. That is, for each channel i , we have d_M outputs obtained by shifting w_i as,

$$\begin{aligned} s_{ic}[\mathbf{n}] &= w_i[M\mathbf{n} + \mathbf{k}_c], \quad (0 \leq c \leq d_M - 1, \quad 0 \leq i < N) \\ &= \sum_{\mathbf{m} \in \mathbb{Z}^d} x[\mathbf{m}] h_i[M\mathbf{n} - \mathbf{m} + \mathbf{k}_c] \\ &= \sum_{\tilde{\mathbf{m}} \in \mathbb{Z}^d} x[\tilde{\mathbf{m}} + \mathbf{k}_c] h_i[M\mathbf{n} - \tilde{\mathbf{m}}]. \end{aligned}$$

As a result, s_{ic} equals the c th polyphase component of w_i , that is, $s_{ic}[\mathbf{n}] = w_{ic}[\mathbf{n}]$, $(0 \leq c \leq d_M - 1, \quad 0 \leq i < N)$. Now if one shifts the input as $x'[\mathbf{n}] = x[\mathbf{n} + \mathbf{p}]$, $(\mathbf{p} \in \mathbb{Z}^d)$, one obtains the same shift for $w_i[\mathbf{n}]$, $(0 \leq i < N)$ as $w_i'[\mathbf{n}] = w_i[\mathbf{n} + \mathbf{p}]$. It turns out that $s_i'[\mathbf{n}] = \{w_i[M\mathbf{n} + M\mathbf{p} + \mathbf{k}_c], \quad 0 \leq c \leq d_M - 1\}$, the set of polyphase components of $w_i'[\mathbf{n}]$, is equal to $s_i[\mathbf{n} + \mathbf{p}]$. \square

A.2 Proof of Remark 2.3 (see Section 2.3)

We can prove this proposition in the polyphase domain. Let the filters and input signal $x[\mathbf{n}]$ in the polyphase domain be $H_i(\mathbf{z}) = \sum_{c=0}^{d_M-1} \mathbf{z}^{k_c} H_{ic}(\mathbf{z}^M)$,

$G_i(\mathbf{z}) = \sum_{c=0}^{d_M-1} \mathbf{z}^{-k_c} G_{ic}(\mathbf{z}^M)$, and $X(\mathbf{z}) = \sum_{c=0}^{d_M-1} \mathbf{z}^{-k_c} X_c(\mathbf{z}^M)$. Now we use a matrix

notation for the polyphase components as $\mathbf{X}_{\mathcal{P}}(\mathbf{z}) = (X_0(\mathbf{z}), \dots, X_{d_M-1}(\mathbf{z}))^T$ (here the

subscript \mathcal{P} denotes the polyphase domain), $\mathbf{Y}(\mathbf{z}) = (Y_0(\mathbf{z}), \dots, Y_{N-1}(\mathbf{z}))^T$, and

$$\mathbf{H}_{\mathcal{P}}(\mathbf{z}) = \begin{bmatrix} H_{00}(\mathbf{z}) & \cdots & H_{0,(d_M-1)}(\mathbf{z}) \\ \vdots & \ddots & \vdots \\ H_{(N-1),0}(\mathbf{z}) & \cdots & H_{(N-1),(d_M-1)}(\mathbf{z}) \end{bmatrix},$$

and

$$\mathbf{G}_{\mathcal{P}}(\mathbf{z}) = \begin{bmatrix} G_{00}(\mathbf{z}) & \cdots & G_{0,(N-1)}(\mathbf{z}) \\ \vdots & \ddots & \vdots \\ G_{(d_M-1),0}(\mathbf{z}) & \cdots & G_{(d_M-1),(N-1)}(\mathbf{z}) \end{bmatrix}.$$

Thus in the polyphase domain we have [89], [92]

$$\mathbf{Y}(\mathbf{z}) = \mathbf{H}_{\mathcal{P}}(\mathbf{z})\mathbf{X}_{\mathcal{P}}(\mathbf{z}), \quad (\text{A.1})$$

and for the synthesis part, the reconstructed signal is

$$X_r(\mathbf{z}) = \Delta^T(\mathbf{z}^{-1})\mathbf{G}_{\mathcal{P}}(\mathbf{z}^M)\mathbf{Y}(\mathbf{z}^M), \quad (\text{A.2})$$

where $\Delta(\mathbf{z}) = (\mathbf{z}^{k_0}, \mathbf{z}^{k_1}, \dots, \mathbf{z}^{k_{d_M-1}})^T$. Figure 39 shows the FB represented in the

polyphase domain. By inserting $\mathbf{Y}(\mathbf{z}^M)$ from (A.1) to (A.2) we obtain the reconstructed

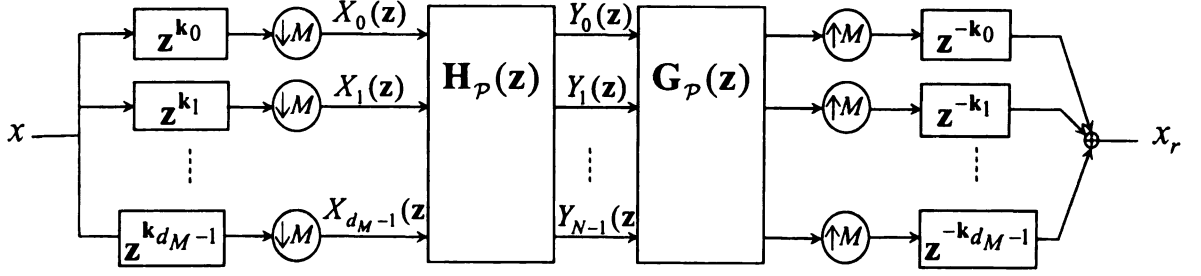


Figure 39. The polyphase domain scheme of the multi-channel filter bank given in Figure 5.

signal as

$$X_r(\mathbf{z}) = \Delta^T(\mathbf{z}^{-1}) \mathbf{G}_p(\mathbf{z}^M) \mathbf{H}_p(\mathbf{z}^M) X_p(\mathbf{z}^M).$$

We denote $\mathbf{T}_p(\mathbf{z}^M) = \mathbf{G}_p(\mathbf{z}^M) \mathbf{H}_p(\mathbf{z}^M)$ as the transfer function of the FB in the polyphase domain. It is clear that for perfect reconstruction we should have $\mathbf{T}_p(\mathbf{z}^M) = \mathbf{I}_{d_M}$, which leads to

$$X_r(\mathbf{z}) = \Delta^T(\mathbf{z}^{-1}) X_p(\mathbf{z}^M) = X(\mathbf{z}).$$

Now, we omit the subsampling operations, leading to a non-subsampled FB as depicted in Figure 6. Note that before doing this, it is better to transfer the downsampling (upsampling) operations to the right (left) side of the analysis (synthesis) filters. As shown below, this is advantageous since when we omit the subsampling operations, the transform coefficients will be the same as those in Figure 5 before downsampling, i.e.,

$\mathbf{W}(\mathbf{z}) = (W_0(\mathbf{z}), \dots, W_{N-1}(\mathbf{z}))^T$. The forward transform is expressed as

$$\mathbf{W}(\mathbf{z}) = X(\mathbf{z}) \mathbf{H}_p(\mathbf{z}^M) \Delta(\mathbf{z}).$$

On the other hand,

$$X_r(\mathbf{z}) = \Delta^T(\mathbf{z}^{-1}) \mathbf{G}_p(\mathbf{z}^M) \mathbf{W}(\mathbf{z}).$$

As a result,

$$X_t(\mathbf{z}) = d_M X(\mathbf{z}).$$

It follows that we need a scaling factor to ensure perfect reconstruction as $a = 1/d_M$.

Since the resulting TI scheme is non-subsampled, the redundancy of this scheme equals the number of channels, N .

Finally, since the output of the channel c , ($0 \leq c \leq d_M - 1$) of synthesis bank is

$$X_t^{(c)}(\mathbf{z}) = \mathbf{z}^{\mathbf{k}_c} \mathbf{z}^{-\mathbf{k}_c} X(\mathbf{z}) = X(\mathbf{z}),$$

we have

$$X_r(\mathbf{z}) = (1/d_M) \sum_{c=0}^{d_M-1} X_t^{(c)}(\mathbf{z}).$$

□

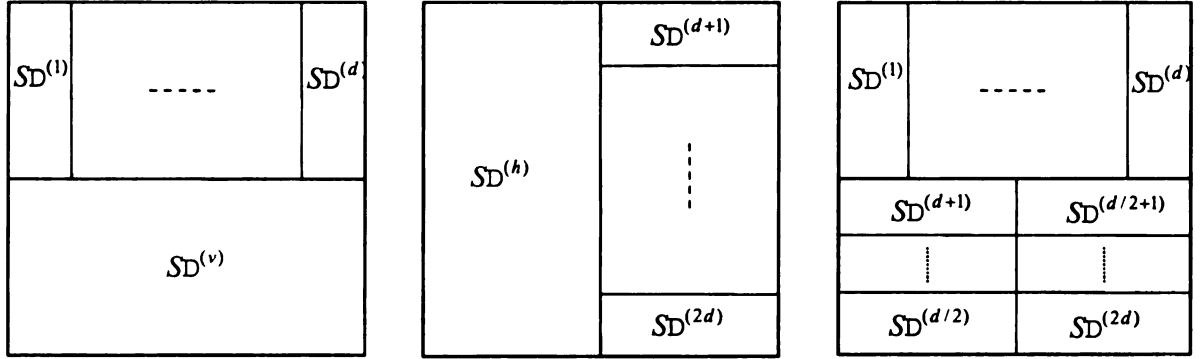


Figure 40. A schematic diagram of the directional subbands using l levels ('S' is 'H' or 'V', and $d = 2^{l-1}$). *Left:* Subbands obtained by applying HDFB to a wavelet highpass channel. *Middle:* Subbands obtained by applying VDFB. *Right:* Subbands obtained by applying full-tree DFB.

A.3 The Rearrangement Algorithm (see Section 3.5B)

For each of the three types of the subbands in the levels $1 \leq j \leq J_m$, we utilize its individual algorithm as described below (see Figure 40):

1) For subbands that a HDFB is applied: Suppose we decompose a wavelet subband of size $N_s \times N_s$, into $d = 2^{l-1}$ horizontal directional subbands $SD^{(i)}$ ($1 \leq i \leq d$, 'S' is either 'H' or 'V'), each having a size of $\tilde{M} \times \tilde{m}$, where $\tilde{M} = N_s / 2$, and $\tilde{m} = N_s / d$.

Now we combine these directional subbands column-wise to form $SD^{(H)}$ as:

$$SD^{(H)} = [c_1^{h_1} \dots c_1^{h_d} \quad \dots \quad c_{\tilde{m}}^{h_1} \dots c_{\tilde{m}}^{h_d}], \text{ where } c_i^x \text{ denotes the column } i \text{ of subband } SD^{(x)}.$$

To form a subband almost similar to a wavelet subband, we combine the resulting

matrix with $SD^{(v)}$ row-wise to obtain $\tilde{S}_{\text{HDFB}} = [r_1^H r_1^v \quad \dots \quad r_{\tilde{M}}^H r_{\tilde{M}}^v]^T$, where r_i^x

denotes the row i of subband $SD^{(x)}$ and $(\cdot)^T$ denotes the transpose operation.

2) For subbands that a VDFB is applied: Here we use the *dual* procedure of the one we used to rearrange the HDFB subbands. That is, we first combine the vertical directional subbands row-wise, and then we interlace the resulting matrix with $SD^{(h)}$, column-wise to obtain \tilde{S}_{VDFB} .

3) For subbands that a full DFB is applied: In this case, we first combine the horizontal subbands to obtain $SD^{(H)} = [c_1^{h_1} \dots c_1^{h_d} \quad \dots \quad c_{\tilde{m}}^{h_1} \dots c_{\tilde{m}}^{h_d}]$. Now we divide the vertical subbands into two parts and combine each part row-wise separately as

$$SD^{(\nu_1)} = [r_1^{\nu_1} \dots r_1^{\nu_\delta} \quad \dots \quad r_{\tilde{m}}^{\nu_1} \dots r_{\tilde{m}}^{\nu_\delta}]^T,$$

and

$$SD^{(\nu_2)} = [r_1^{\nu_{\delta+1}} \dots r_1^{\nu_d} \quad \dots \quad r_{\tilde{m}}^{\nu_{\delta+1}} \dots r_{\tilde{m}}^{\nu_d}]^T,$$

where $\delta = d/2$. Interlacing the resulting matrices column-wise, we obtain $SD^{(\hat{\nu})}$,

which is the same size as $SD^{(H)}$: $SD^{(\hat{\nu})} = [c_1^{\nu_1} c_1^{\nu_2} \quad \dots \quad c_{\tilde{M}}^{\nu_1} c_{\tilde{M}}^{\nu_2}]$. Finally, we interlace

$SD^{(H)}$ and $SD^{(\hat{\nu})}$ row-wise and obtain $\tilde{S}_{\text{DFB}} = [r_1^H r_1^{\hat{\nu}} \quad \dots \quad r_{\tilde{M}}^H r_{\tilde{M}}^{\hat{\nu}}]^T$.

REFERENCES

- [1] R. Ansari, C. W. Kim, and M. Dedovic, "Structure and design of two-channel filter banks derive from a triplet of halfband filters," *IEEE Trans. Circuits and Systems-II*, vol. 46, no. 12, pp. 1487-1496, Dec. 1999.
- [2] J. P. Antoine, P. Carrette, R. Murenzi and B. Piette, "Image analysis with two-dimensional continuous wavelet transform," *Signal Processing*, vol. 31, pp. 241-272, 1993.
- [3] R. H. Bamberger, "New results on two and three dimensional directional filter banks," in *Proc. of Asilomar Conf. Signals, Systems, and Computers*, vol. 2, pp: 1286-1290, 1993.
- [4] _____, "New subband decompositions and coders for image and video compression," in *Proc. of IEEE Int. Conf. Acoustics, Speech, and Signal Processing*, vol. 3, pp. 217-220, Mar. 1992.
- [5] R. H. Bamberger and M. J. T. Smith, "A filter bank for the directional decomposition of images: Theory and design," *IEEE Trans. Signal Processing*, vol. 40, no. 4, pp. 882-893, Apr. 1992.
- [6] G. Beylkin, "On the representation of operators in bases of compactly supported wavelets," *SIAM J. Numerical Analysis*, vol. 29, pp.1716-1740, 1992.
- [7] P. J. Bickel K. A. Doksum, *Mathematical Statistics: Basic Ideas and Selected Topics*. Oakland, CA, Holden-Day, 1977.
- [8] W. Brghorn, T. Boskamp, M Lang, and H.-O. Peitgen, "Fast variable run-length coding for embedded progressive wavelet-based image compression," *IEEE Trans. Image Processing*, vol. 10, pp. 1781-1790, Dec. 2001.
- [9] P. Brodatz, *Textures, A photographic album for artists and designers*. Some images available on <http://www.ux.his.no/~tranden/brodatz.html>.
- [10] P. J. Burt and E. H. Adelson, "The Laplacian pyramid as a compact image code," *IEEE Trans. Communications*, vol. 31, no. 4, pp. 532-540, Apr. 1983.
- [11] E. J. Candes, L. Demanet, D. Donoho, and L. Ying, "Fast discrete curvelet transform," preprint available on <http://www.curvelet.org/papers/FDCT.pdf>. Software available on <http://www.curvelet.org/software.html>.
- [12] E. J. Candes and D. L. Donoho, "Curvelets – a surprisingly effective nonadaptive representation for objects with edges," in *Curve and Surface Fitting*, Saint- Malo, 1999, Vanderbuilt Univ. Press.
- [13] _____, "New tight frames of curvelets and optimal representations of objects with piecewise C^2 singularities," *Commun. Pure Applied Math.*, vol. 57, pp. 219-266, Feb. 2004.

- [14] _____, "Ridgelets: a key to higher-dimensional intermittency?," *Phil. Trans. R. Soc. Lond. A.*, pp. 2495-2509, 1999.
- [15] E. Candès and F. Guo, "New multiscale transforms, minimum total variation synthesis: applications to edge-preserving image reconstruction," *Signal Processing*, vol. 82, pp. 1519-1543.
- [16] T. F. Chan and H. M. Zhou, "Optimal construction of wavelet coefficients using total variation regularization in image compression," *CAM Technical report*, UCLA, 2000.
- [17] E. Chang and A. Zakhor, "Subband video coding based on velocity filters," in *Proc. of IEEE Int. Conf. Circuits and Systems*, vol. 5, pp. 2288-2291, May 1992.
- [18] S. Chen and D. Donoho, "Atomic decomposition by basis pursuit," in *SPIE Intl. Conf. Wavelets*, San Diego, Jul. 1995.
- [19] R. R. Coifman and M. V. Wickerhauser, "Entropy-based algorithms for best basis selection," *IEEE Trans. Information Theory*, vol. 38, pp. 713-718, 1992.
- [20] A. Cohen, I. Daubechies, O. Guleryuz, and M. Orchard, "On the importance of combining wavelet-based non-linear approximation with coding strategies," *IEEE Trans. Information Theory*, vol. 48, no. 7, pp. 1895-1921, Jul. 2002.
- [21] I. Cohen, S. Raz, and D. Malah, "Orthonormal shift-invariant wavelet packet decomposition and representation," *Signal Processing*, vol. 57, No. 3, pp. 251-270, Mar. 1997.
- [22] R. R. Coifman and D. L. Donoho, "Translation invariant de-noising," in *Wavelets and Statistics, Springer Lecture Notes in Statistics 103*, New York, Springer-Verlag, pp. 125-150, 1995.
- [23] A. L. Cunha, J. Zhou, and M. N. Do, "The nonsubsampling contourlet transform: theory, design, and applications" *IEEE Trans. Image Processing*, to be published.
- [24] Z. Cvetkovic and M. Vetterli, "Oversampled filter banks," *IEEE Trans. Signal Processing*, vol. 46, pp. 1245-1255, May 1998.
- [25] I. Daubechies, *Ten Lectures on Wavelets*. Philadelphia, SIAM, 1992.
- [26] M. N. Do, *Directional multiresolution image representations*. PhD thesis, EPFL, Lausanne, Switzerland, Dec. 2001.
- [27] M. N. Do and M. Vetterli, "Contourlets," in *Beyond Wavelets*, Academic Press, New York, 2003.
- [28] _____, "The contourlet transform: An efficient directional multiresolution image representation," *IEEE Trans. Image Processing*, vol. 14, no. 12, pp. 2091-2106, Dec. 2005. Software available on <http://www.ifp.uiuc.edu/~minhdo/software/>.

- [29] M. N. Do and M. Vetterli, "Framing pyramids," *IEEE Trans. Signal Processing*, vol. 51, no. 9, pp. 2329-2342, Sep. 2003.
- [30] D. L. Donoho, "Nonlinear wavelet methods for recovery of signals, densities, and spectra from indirect and noisy data" in *proc. of Symposia in Applied Math.*, pp. 173-205, 1993.
- [31] D. Donoho and X. Huo, "Beamlets and multiscale image analysis," *Multiscale and Multiresolution Methods, Springer Lecture Notes in Computational Science and Engineering* (Editors T.J. Barth, T. Chan, and R. Haimes), vol. 20, pp. 149-196, 2002.
- [32] D. L. Donoho and I. M. Johnstone, "Ideal spatial adaptation by wavelet shrinkage," *Biometrika*, vol. 81, no. 3, pp. 425-455, 1994.
- [33] S. Durand and J. Froment, "Artifact free signal denoising with wavelets," in *Proc. of IEEE Int. Conf. Acoustics, Speech, and Signal Processing*, pp. 3685-3688, 2001.
- [34] R. Eslami, J. R. Deller and H. Radha, "On the detection of multiplicative watermarks for speech signals in the wavelet and DCT domains," in *Proc. of IEEE Int. Conf. Multimedia and Expo*, Toronto, Canada, Jul. 2006.
- [35] R. Eslami and H. Radha, "A new family of nonredundant transforms using hybrid wavelets and directional filter banks," *IEEE Trans. Image Processing*, 2006.
- [36] _____, "Image denoising using translation-invariant contourlet transform," in *proc. of IEEE Int. Conf. Acoustics, Speech, and Signal Processing*, vol. 4, pp. 557-560, Mar. 2005.
- [37] _____, "Image watermarking using hybrid wavelets and directional filter banks," in *Proc. of Conf. Information Sciences and Systems*, Princeton, NJ, Mar. 2006.
- [38] _____, "New image transforms using hybrid wavelets and directional filter banks: analysis and design," in *Proc. of IEEE Int. Conf. Image Processing*, vol. 1, pp. 733-736, Genova, Italy, Sep. 2005.
- [39] _____, "On low bit-rate coding using the contourlet transform," in *proc. Asilomar Conf. Signals, Systems, and Computers*, pp. 1524-1528, Pacific Grove, USA, Nov. 2003.
- [40] _____, "On the linear combination of denoising schemes," *submitted to IEEE Trans. Signal Processing*, 2006.
- [41] _____, "Optimal linear combination of denoising schemes for efficient removal of image artifacts," in *Proc. of IEEE Int. Conf. Multimedia and Expo*, Toronto, Canada, Jul. 2006.
- [42] _____, "Regular hybrid wavelets and directional filter banks: extensions and applications," *to appear in Proc. of IEEE Int. Conf. Image Processing*, Atlanta, GA, Oct. 2006.
- [43] _____, "The contourlet transform for image de-noising using cycle spinning," in *Asilomar Conf. Signals, Systems, and Computers*, pp. 1982-1986, Pacific Grove, USA, Nov. 2003.
- [44] _____, "Translation-invariant contourlet transform and its application to image denoising," *IEEE Trans. Image Processing*, to be published, Nov. 2006.

- [45] _____, "Wavelet-based contourlet coding using an SPIHT-like algorithm," in *proc. of Conf. Information Sciences and Systems*, pp. 784-788, Princeton, March 2004.
- [46] _____, "Wavelet-based contourlet packet image coding," in *proc. of Conf. Information Sciences and Systems (CISS)*, Baltimore, MD, Mar. 2005.
- [47] _____, "Wavelet-based contourlet transform and its application to image coding," in *proc. of IEEE Int. Conf. Image Processing*, vol. 5, pp. 3189-3192, Singapore, Oct. 2004.
- [48] F. C. A. Fernandes, R. L. C. van Spaendonck, and C. S. Burrus, "Multidimensional, mapping-based complex wavelet transforms," *IEEE Trans. Image Processing*, vol. 14, no. 1, pp. 110-124, Jan. 2005.
- [49] M. Holschneider, R. Kronland-Martinet, J. Morlet, and P. Tchamitchian, "A real-time algorithm for signal analysis with the help of the wavelet transform," in *Wavelets, Time-Frequency Methods and Phase Space*, pp. 289-297, Springer-Verlag, Berlin, 1989.
- [50] P. Hong and M. J. T. Smith, "An octave-band family of non-redundant directional filter banks," in *IEEE proc. ICASSP*, vol. 2, pp. 1165-1168, 2002.
- [51] X. Huo, *Sparse Image Representation via Combined Transforms*. Ph.D. thesis, Stanford University, Aug. 1999.
- [52] T. Kailath, A. H. Sayed, and B. Hassibi, *Linear Estimation*. Prentice Hall, 2000.
- [53] N. G. Kingsbury, "Complex wavelets for shift invariant analysis and filtering of signals," *Applied and Computational Harmonic Analysis*, vol. 10, no. 3, pp. 234-253, May 2002.
- [54] _____, "Image processing with complex wavelets," *Phil. Trans. R. Soc. London*, Sep. 1999.
- [55] J. Kovacevic and M. Vetterli, "Nonseparable multidimensional perfect reconstruction filter banks and wavelet bases for \mathbb{R}^n ," *IEEE Trans. Information Theory*, vol. 38, pp. 533-555, Mar. 1992.
- [56] _____, "Nonseparable two- and three-dimensional wavelets," *IEEE Trans. Signal Processing*, vol. 43, pp. 1269-1273, May 1995.
- [57] E. LePennec and S. Mallat, "Sparse geometric image representation with bandelets," *IEEE Trans. Image Processing*, vol. 14, no. 4, p. 423-438, Apr. 2005.
- [58] J. S. Lim, *Two-Dimensional Signal and Image Processing*. Prentice Hall, 1990.
- [59] Y. Lu and M. N. Do, "CRISP-contourlets: a critically sampled directional multiresolution image representation," in *proc. of SPIE conference on Wavelet Applications in Signal and Image Processing X*, San Diego, USA, August 2003.
- [60] S. Mallat, *A Wavelet Tour of Signal Processing*. Academic Press, 2nd Ed., 1998.

- [61] S. Mallat and F. Falzon, "Analysis of low bit-rate image transform coding," *IEEE Trans. Signal Processing*, vol. 46, no. 4, pp. 1027-1042, Apr. 1998.
- [62] S. Mallat and S. Zhong, "Characterization of signals from multiscale edges," *IEEE Trans. Pattern Analysis and Machine Intelligence*, vol. 14, no. 7, pp. 710-732, Jul. 1992.
- [63] _____, "Matching pursuit with time-frequency dictionaries," *IEEE Trans. Signal Processing*, vol. 41, pp. 3397-3415, Dec. 1993.
- [64] F. G. Mayer, A. Z. Averbuch, and J.-O. Stromberg, "Fast adaptive wavelet packet image compression," *IEEE Trans. Image Processing*, vol. 9, no. 5, pp. 792-800, May 2000.
- [65] F. G. Meyer and R. R. Coifman, "Brushlets: a tool for directional image analysis and image compression," *Applied and Computational Harmonic Analysis*, vol. 4, pp. 147-187, 1997.
- [66] G. P. Nason and B. W. Silverman, "The stationary wavelet transform and some statistical applications," in *Wavelets and Statistics, Springer Lecture Notes in Statistics 103*, New York, Springer-Verlag, pp. 281-299, 1995.
- [67] T. T. Nguyen and S. Orlintara, "Multiresolution direction filterbanks: Theory, design, and applications," *IEEE Trans. Signal Processing*, vol. 53, no. 10, pp. 3895-3905, Oct. 2005.
- [68] B.A. Olshausen and D.J. Field, "Emergence of simple-cell receptive field properties by learning a sparse code for natural images," *Nature*, no. 381, pp. 607-609, 1996.
- [69] A. V. Oppenheim, R. W. Schaffer, and J. R. Buck, Discrete-time signal processing. Prentice Hall, 2nd Ed., 1999.
- [70] S. Park, M. J. T. Smith, and R. M. Mersereau, "Improved structures of maximally decimated directional filter Banks for spatial image analysis," *IEEE Trans. Image Processing*, vol. 13, no. 11, pp. 1424-1431, 2004.
- [71] J.-C. Pesquet, H. Krim, and H. Carfantan, "Time-invariant orthonormal wavelet representations," *IEEE Trans. Signal Processing*, vol. 44, no. 8, pp. 1964-1970, Aug. 1996.
- [72] S. M. Phoong, C. W. Kim, P. P. Vaidyanathan, and R. Ansari, "A new class of two-channel biorthogonal filter banks and wavelet bases," *IEEE Trans. Signal Processing*, vol. 43, no. 3, pp. 649-665, Mar. 1995.
- [73] J. Portilla, V. Strela, M. J. Wainwright, and E. P. Simoncelli, "Image denoising using scale mixtures of Gaussians in the wavelet domain," *IEEE Trans. Image Processing*, vol. 12, no. 11, pp. 1338-1351, Nov. 2003. (Software is available at <http://decsai.ugr.es/~javier/denoise/index.html>).
- [74] D. D.-Y. Po and M. N. Do, "Directional multiscale modeling of images using the contourlet transform," *IEEE Trans. Image Processing*, vol. 15, pp. 1610-1620, Jun. 2006.
- [75] H. Radha, M. Vetterli, and R. Leonardi, "Image compression using binary space partitioning trees," *IEEE Trans. Image Process.*, vol. 5, no. 12, pp. 1610-1624, Dec. 1996

- [76] K. Ramchandran and M. Vetterli, "Best wavelet packet bases in a rate-distortion sense," *IEEE Trans. Image Processing*, vol. 2, pp. 160-175, Apr. 1993.
- [77] L. I. Rudin, S. Osher, and E. Fatemi, "Nonlinear total variation based noise removal algorithm," *Physica D*, 60, pp. 259-268, 1992.
- [78] A. Said and W. A. Pearlman, "A New Fast and Efficient Image Codec Based on Set Partitioning in Hierarchical Trees," *IEEE Trans. on Circuits and Systems for Video Technology*, vol. 6, pp. 243-250, June 1996.
- [79] L. Sendur and I. W. Selesnick, "Bivariate shrinkage functions for wavelet-based denoising exploiting interscale dependency," *IEEE Trans. Signal Processing*, vol. 50, no. 11, pp. 2744-2756, Nov. 2002.
- [80] L. Sendur and I. W. Selesnick, "Bivariate shrinkage with local variance estimation," *IEEE Signal Processing Letters*, vol. 9, no. 12, Dec. 2002. (Software is available at <http://taco.poly.edu/WaveletSoftware/index.html>).
- [81] J. M. Shapiro, "Embedded image coding using zerotrees of wavelet coefficients," *IEEE Trans. Signal Processing*, vol. 41, pp. 3445-3462, Dec. 1993.
- [82] M. J. Shensa, "The discrete wavelet transform: wedding the à trous and Mallat algorithms," *IEEE Trans. Signal Processing*, vol. 40, no. 10, pp. 2464-2482, Oct. 1992.
- [83] R. Shukla, P. L. Dragotti, M. N. Do and M. Vetterli, "Rate-distortion optimized tree structured compression algorithms for piecewise smooth images," *IEEE Trans. Image Processing*, vol. 14, pp. 343-359, Mar. 2005.
- [84] E. P. Simoncelli and W. T. Freeman, "The steerable pyramid: A flexible architecture for multi-scale derivative computation" in *proc. Intl. Conf. on Image Processing*, Washington DC, 1995.
- [85] E. P. Simoncelli, W. T. Freeman, E. H. Adelson, and D. J. Heeger, "Shiftable multi-scale transforms," *IEEE Trans. Information Theory*, vol. 38, no. 2, pp. 587-607, 1992.
- [86] J.-L. Starck, E. J. Candes, and D. L. Donoho, "The curvelet transform for image denoising," *IEEE Trans. Image Processing*, vol. 11, pp. 670-684, Jun. 2002.
- [87] J.-L. Starck, D. L. Donoho, and E. Candes, "Very high quality image restoration," in *Proc. SPIE Conf. Signal and Image Processing: Wavelet Apps. Sig. and Image Proc. IX*, vol. 4478, 2001.
- [88] G. J. Sullivan, "Efficient scalar quantization of exponential and Laplacian random variables," *IEEE Trans. Information Theory*, vol. 42, pp. 1365-1374, Sep. 1996.
- [89] P. P. Vaidyanathan, *Multirate Systems and Filter Banks*. Prentice Hall, 1993.
- [90] V. Velisavljevic, B. Beferull-Lozano, M. Vetterli and P.L. Dragotti, "Directionlets: Anisotropic Multidirectional representation with separable filtering," *IEEE Trans. Image Processing*, vol. 15, pp. 1916 – 1933, Jul. 2006.

- [91] M. Vetterli, "Wavelets, approximation and compression," *IEEE Signal Processing Magazine*, vol. 18, no. 5, pp. 59–73, Sep. 2001.
- [92] M. Vetterli and J. Kovacevic, *Wavelets and Subband Coding*. Prentice Hall, 1995.
- [93] M. Wakin, J. K. Romberg, H. Choi, and R. G. Baraniuk, "Wavelet-domain approximation and compression of piecewise smooth images," *IEEE Trans. Image Processing*, vol. 15, no. 5, pp. 1071-1087, May 2006.
- [94] Z. Xiong, K. Ramchandran, and M. Vetterli, "Space-frequency quantization for wavelet image coding," *IEEE Trans. Image Processing*, vol. 6, no. 5, pp. 677-693, May 1997.
- [95] R. Zuidwijk, "Continuous and discrete wavelet X-ray transform," *SPIE Wavelet Application in Signal and Image Processing V*, pp. 357-366, 1997.

2

1

MICHIGAN STATE UNIVERSITY LIBRARIES



3 1293 02845 6022